MODELING STUDY OF AIR POLLUTION IN THE MEXICO CITY AREA

ZHUMING YING

A THESIS SUBMITTED TO THE FACULTY OF GRADUATE STUDIES
IN PARTIAL FULFILLMENT OF THE REQUIREMENTS
FOR THE DEGREE OF

DOCTOR OF PHILOSOPHY

GRADUATE PROGRAM IN EARTH AND SPACE SCIENCE
YORK UNIVERSITY
NORTH YORK, ONTARIO

August 2012

Abstract

The purpose of this research is to study the air pollution problem in the Mexico City (MC) area. The WRF/Chem model is used to simulate the chemical oxidants and dust aerosols, including meteorological conditions. The observations during the 2006 MILAGRO (Megacity Initiative: Local and Global Research Observations) experiments are used to evaluate the model results and to understand the characterizations of chemical species (CO, NO, $NO2$, and O_3): their magnitudes, diurnal variations, and horizonal distributions.

The main results are: (1) the chemical O_3 formation is found to be under VOC-limited regime in the MC's center and south zone during March 12-15, 2006, and weakly sensitive to VOCs in the north, especially in the northeast zone. It is also found that the O_3 production is possibly sensitive to both NO_x and VOCs in the downwind suburb area, and NO_x-limited in the further rural area. The OH reactivity with VOCs is calculated from simulations. It shows that alkenes dominate the OH reactivity at the city emission source site; and at the downwind site, oxygenated hydrocarbons make the largest contribution, and CO plays a relatively more important role in the OH reactivity. The most important VOCs in terms of OH reactivity is acetaldehyde in the all sites. (2) the diurnal variations of surface emissions play an important role in controlling the O_3 concentrations in the MC area, and also in the downwind suburb area. The daytime O_3 concentrations are sensitive to emissions of

NO_x and VOCs in the morning, increase in daytime O_3 concentrations as well as the afternoon O_3 maximum are mainly attributable to the increase of VOC emissions and the decrease of NO_x emissions in the morning. The sensitivity experiments also suggest that without reduction of total emissions, the daytime concentrations of CO, NO_x, and O_3 and their maxima can be significantly reduced by changing the timing of surface emissions. (3) the large area of dry barren lands to the northeast of MC is found to be an major source of dust particles for the entire MC area. With dust module included in the WRF/Chem model, the simulated aerosols were significantly improved in terms of their mass concentrations and diurnal variations. Dust accounts for about 50% of total $PM_{2.5}$ mass, and 70% of total PM_{10} mass during the period of March 16-20, 2006. The simulation results also show that dust aerosols have important effects on actinic fluxes and hence photochemistry, especially on hydroxyl radical (OH) and ozone (O_3) concentrations, in the MC area and the surrounding region. The dust aerosols lead to a significant reduction of the surface concentrations of OH and O_3. The maximum reduction of OH is about 0.3 pptv in the dust source region, and the maximum reduction of O_3 is about 10 ppbv near Mexico city.

Acknowledgments

I would like to thank my supervisor, Professor Jack McConnell, who read the whole thesis carefully, without complaining, and made many constructive comments and suggestions, which greatly improved this manuscript. I would also like to thank all other committee members for their constructive comments.

I would especially like to thank Dr. Xuexi Tie, for his guidance and continuous encouragement throughout this work. I would like also thank Dr. Sasha Madronich, for accepting me as a visiting student at ACD/NCAR, and for many interesting discussion, and his detailed, valuable comments and suggestions. ACD/NCAR is acknowledged for providing me a work space and partial financial support. Thanks also go to Dr. Guohui Li, for the help on the WRF/Chem model and Dr. Steven Massie for providing the figure of measured absorbing Aerosol Optical Depth (AOD) in the MC region.

On a personal level, I am grateful to my parents, especially to my father, who always inspired me in my study and work. And I thank my family for their support and love during this work.

Contents

List of Tables

List of Figures

Chapter 1

Introduction

Dramatic increases in global population and urbanization, and rapid growth of industrialization in many regions of the world may have significant consequences for air pollution problem on a broad regional or even global scale. World-wide emissions from growing industrial and transportation activity have caused widespread increase in concentrations of photochemical oxidants, acid gases, fine particles, and other toxic chemical species. Many of these air pollutants are known to have harmful impacts on human health and plants.

1.1 Photochemical air pollution

Photochemical air pollution is a worldwide issue, particularly in large urbanized areas. It was first recognized in Los Angeles in the 1950s, and later in many other urban and even rural regions. This type of air pollution, also known as photochemical smog, is characterized by the presence of high concentration of ozone (O_3) and other oxidants, nitrogen oxides ($NO_x = NO + NO_2$) and volatile organic compounds (VOCs) as primary pollutants in the ambient air on warm days with bright sunshine (e.g. Jacob, 1999, Brasseur *et al.*, 1999, Molina and Molina, 2002). The troposphere contains only

about 10% of all atmospheric ozone, but this lower level ozone causes health problems (eye and nose irritation, respiratory discomfort), and plant damage and reduction in crop productivity.

Nitrogen oxides (NO_x) and volatile organic compounds (VOCs) are common products of human activities, and are released in large quantities by automobiles in urban areas (e.g. Brasseur *et al.*, 2003). Those pollutants tend to accumulate in the boundary layer under stable meteorological conditions, and undergo photochemical transformations when solar ultraviolet radiation is intense. They can be transported downwind and affect rural environments in the vicinity of metropolitan areas. From a local and regional perspective, NO_x and VOCs are responsible for the degradation of air quality by forming ozone and secondary particulate matters.

1.1.1 Ozone production

The reaction mechanisms for tropospheric ozone formation are complex. Photons at wavelengths shorter than 290 nm are not present in the troposphere, so that O_2 can't be photolyzed and O_3 cannot be produced via Chapman mechanism in troposphere. However nitrogen dioxide can be photolyzed at $\lambda \leq 420\ nm$, the photochemical activity of NO_2 are:

$$NO + O_3 \rightarrow NO_2 + O_2 \tag{1.1}$$

$$NO_2 + h\nu \rightarrow NO + O \tag{1.2}$$

$$O + O_2 + M \rightarrow O_3 + M \tag{1.3}$$

This cycling between NO and NO_2 takes place on a time scale of about one minute during daytime, but no net O_3 is produced.

As was first realized in early 1970s, the hydroxyl radical, OH, is the critical hydrocarbon oxidant driving O_3 formation, which dominates the daytime chemistry in the troposphere (e.g. Jacob, 1999). It does not react with the principal atmospheric constituents N_2, O_2, H_2O and CO_2; it reacts with almost all trace gases that are emitted by natural processes and anthropogenic activities into the atmosphere, such as hydrocarbons, carbon monoxide, most sulfur- and halogen-containing compounds, as well as nitrogen oxides. The OH-reaction is a radical chain reaction, OH can be recycled on the order of $10^6\, molecule\, cm^{-3}$ during daylight hours when reacting with atmospheric trace gases (Seinfeld *et al.*, 2006).

Tropospheric OH radicals originate from O_3 photolysis (at a narrow wavelength band between 300 and 320 nm) in the presence of water vapor:

$$O_3 + h\nu \rightarrow O_2 + O(^1D) \tag{1.4}$$

$$O(^1D) + M \rightarrow O + M \tag{1.5}$$

$$O(^1D) + H_2O \rightarrow 2OH \tag{1.6}$$

The concentrations of OH are much lower. However OH radicals can react with carbon monoxide and almost all hydrocarbons with much higher concentrations in the troposphere. The oxidation reactions are:

$$CO + OH \xrightarrow{O_2} HO_2 + CO_2 \tag{1.7}$$

$$RH + OH \xrightarrow{O_2} RO_2 + H_2O \tag{1.8}$$

Here RH (R is an organic group) is used as a simplified notation for hydrocarbons (including CH_4). It is the presence of NO_x that allows the propagation of the OH-reaction chain, OH is recycled and O_3 is produced. The peroxy radicals (HO_2, RO_2) react with NO, and cause NO to rapidly convert to NO_2 without consuming O_3 but

with additional OH production, viz.,

$$RO_2 + NO \xrightarrow{O_2} R'CHO + HO_2 + NO_2 \quad (1.9)$$

$$HO_2 + NO \rightarrow OH + NO_2 \quad (1.10)$$

These reactions are followed by photolysis of NO_2, which generates O_3 and also recycles NO in the troposphere,

$$NO_2 + h\nu \xrightarrow{O_2} NO + O_3 \quad (1.11)$$

The reaction chain may be terminated by loss of peroxy radicals (HO_2, RO_2, OH). At high NO_x concentrations, OH may react with NO_2,

$$OH + NO_2 + M \rightarrow HNO_3 + M \quad (1.12)$$

under low NO_x concentrations, peroxy radicals, with quite "short" life time, may react with themselves and with other peroxy radicals instead of NO, with peroxide formation.

$$HO_2 + HO_2 \rightarrow H_2O_2 + O_2 \quad (1.13)$$

$$RO_2 + HO_2 \rightarrow ROOH + O_2 \quad (1.14)$$

Hydrogen peroxides are highly soluble in water and are removed from the atmosphere by deposition in a week (Jacob, 1999). They can also photolyze or react with OH, and be the temporary reservoir for OH and HO_2:

$$H_2O_2 + h\nu \rightarrow 2OH \quad (1.15)$$

$$H_2O_2 + OH \rightarrow HO_2 + H_2O \quad (1.16)$$

and

$$ROOH + h\nu \rightarrow RO + OH \tag{1.17}$$

$$ROOH + OH \rightarrow RO_2 + H_2O \tag{1.18}$$

Ozone is mainly produced within the troposphere during daylight by oxidation of CO and hydrocarbons in the presence of sufficient NO_x (e.g. Finlayson-Pitts, 2000). The sequence of reactions (R1.7, R1.8) + (R1.10, R1.9) + (R1.11) are chain mechanisms for O_3 production. During urban or small scale ozone episodes, CH_4 may be excluded from consideration due to its relatively slow oxidization rate, and non-methane hydrocarbons (NMHCs) or VOCs (other than CH_4) are the focus for rapid ozone production.

Loss of O_3 from the troposphere takes place by photolysis (R1.4 - R1.6) in the visible and ultraviolet regions. Besides reacting with NO (R1.1), Ozone can also be consumed by reactions with OH, and HO_2,

$$OH + O_3 \rightarrow HO_2 + O_2 \tag{1.19}$$

$$HO_2 + O_3 \rightarrow OH + 2O_2 \tag{1.20}$$

additional removal of O_3 takes place by dry deposition at the surface.

Ozone is largely controlled by photochemical production and loss within the troposphere. Transport from the stratosphere and dry deposition at the surface are relatively small terms. Chemical production dominates the source of tropospheric O_3 ($4100\ Tg\ yr^{-1}$), as compared with $400 - 500\ Tg\ yr^{-1}$ estimated for transport down from the stratosphere. The net chemical production (production - loss) is $\sim 400 - 500\ Tg\ yr^{-1}$, and the dry deposition accounts for about $800 - 1000\ Tg\ yr^{-1}$ of loss (e.g. Wang *et al.*, 1998). The globally averaged tropospheric sources and sinks

for ozone are roughly in balance. Chemical production of O_3 results primarily from reactions of peroxy radicals with NO, which about 70% are $HO_2 + NO$, about 20% are $CH_3O_2 + NO$, and the remainder are larger peroxy radical $RO_2 + NO$. Ozone chemical loss results mainly from O_3 photolysis to $O(^1D) + H_2O$ ($\sim$ 40%), $HO_2 + O_3$ ($\sim$ 40%), and $OH + O_3$ ($\sim$ 10%) (Jacob, 1999).

1.1.2 Nitrogen oxides (NO_x)

The nitrogen oxides are released into the atmosphere by human activities or by natural phenomena, the estimated sources of NO_x is shown in Table 3.1 of Brasseur *et al.* (2003). The predominant source of NO_x is surface-based fossil fuel combustion ($\sim$ 22 $TgNyr^{-1}$), which accounts for about half of the total global source. This source is concentrated at mid-latitudes in Northern Hemisphere. Biomass burning ($\sim$ 8 $TgNyr^{-1}$) and emissions from soils ($\sim$ 7 $TgNyr^{-1}$), mostly in the tropical boundary layer, accounts for about another 35%. Production of NO_x by Lighting ($\sim$ 5 $TgNyr^{-1}$) is the major source in the free troposphere.

NO_x is emitted mainly as NO. During the daytime, NO and NO_2 interconvert by photochemical NO_x cycle (R1.10 - R1.2), the major loss for NO_x is the oxidation of NO_2 to HNO_3 (R1.12). The lifetime of NO_x increases from 1-2 days at the surface to about 2 weeks in the upper troposphere (Seinfeld *et al.*, 2006), In the upper troposphere, HNO_3 can be converted back to NO_x by photolysis and reaction with OH on a time scale of a few weeks.

$$HNO_3 + h\nu \rightarrow OH + NO_2 \tag{1.21}$$

$$HNO_3 + OH \rightarrow NO_3 + H_2O \tag{1.22}$$

But in the mid-lower troposphere, HNO_3 is removed principally by dry and wet deposition and is not an effective reservoir for NO_x.

PAN, peroxyacetyl nitrate ($CH_3C(O)OONO_2$), is another reservoir species. Reservoir species are those trace constituents, such as HNO_3, N_2O_5, that are produced from the more reactive trace species, but are longer-lived and less reactive. Those gases act as temporary reservoirs for the more reactive ozone-producing or -destroying species. PAN is produced in the troposphere by photochemical oxidation of carbonyl compounds in the presence of NO_x. For example, the formation of PAN from acetaldehyde (CH_3CHO) by

$$CH_3CHO + OH \rightarrow CH_3CO + H_2O \tag{1.23}$$

$$CH_3CO + O_2 + M \rightarrow CH_3C(O)OO + M \tag{1.24}$$

$$CH_3C(O)OO + NO_2 + M \rightarrow CH_3C(O)OONO_2 + M \tag{1.25}$$

PAN acts as a reservoir species for both $CH_3C(O)OO$ radicals and NO_x. As sinks for NO_x, formation of PAN is less important than formation of HNO_3. However, in contrast to HNO_3, PAN is only sparingly soluble in water and slightly removed by deposition. Thus, thermal decomposition is the principal removal process for PAN:

$$PAN \xrightarrow{heat} CH_3C(O)OO + NO_2 \tag{1.26}$$

PAN is relatively stable when the temperatures are sufficiently low. The lifetime of PAN is only 1 hour at 295 K, but several months at 250 K. In the lower troposphere, NO_x and PAN are typically near chemical equilibrium. But PAN can be transported over long distances in the middle and upper troposphere, and decompose to release NO_x far from its source. PAN is an effective reservoir for NO_x (e.g. Jacob, 1999; Seinfeld *et al.*, 2006).

1.1.3 Night-time chemistry - NO_3

At high NO_x levels, the nitrate radical, NO_3, takes over from OH as the dominant oxidizing species in the troposphere at night. The diurnal impact of OH and NO_3 is complementary, OH is generated photochemically during the day, while NO_3 is rapidly photolyzed with a lifetime of ~ 5 second at noon (Seinfeld *et al.*, 2006), and can survive only at night.

At nighttime, NO_2 does not photolyze, and NO reacts rapidly with O_3 (R1.1); as a result, the concentration of NO drops near zero, and NO_x is mostly present as NO_2. The chemistry of the NO_x family at night is totally different from that during daytime. The NO_2 reacts with O_3 to form NO_3,

$$NO_2 + O_3 \rightarrow NO_3 + O_2 \tag{1.27}$$

NO_3 reacts with NO_2 to produce N_2O_5, and N_2O_5 itself can thermally decompose back to NO_2 and NO_3, and the reactions establish an equilibrium on a timescale of only a few minutes:

$$NO_2 + NO_3 + M \rightleftharpoons N_2O_5 + M \tag{1.28}$$

As temperature decreases and NO_2 levels increase, the equilibrium is shifted more and more to the right. N_2O_5 can react with H_2O on aqueous aerosol surface to form HNO_3.

$$N_2O_5 + H_2O \xrightarrow{aerosol} 2HNO_3 \tag{1.29}$$

together with reaction of $OH + NO_2$ in daytime, this is one of the major loss for atmospheric NO_x with significant consequences for the tropospheric O_3 budget.

NO_3 can also react with hydrocarbons

$$RH + NO_3 \rightarrow R + HNO_3 \quad (1.30)$$

$$R + O_2 \rightarrow RO_2 \quad (1.31)$$

and followed by:

$$RO_2 + NO_3 \rightarrow RO + NO_2 + O_2 \quad (1.32)$$

$$RO + O_2 \rightarrow R'CHO + HO_2 \quad (1.33)$$

So the radicals such as RO_2 and HO_2 are generated in the reactions with NO_3 during nighttime. Although NO_3 is generally much less reactive than OH with hydrocarbons, the peak concentration of NO_3 is higher with respect to that of OH during the day. The nitrate radical NO_3 plays an important part in atmospheric chemical transformations (e.g. Wayne, 2000).

1.2 Chemical sensitivity of ozone formation

As discussed in above section 1.1.1, daytime ozone production is non-linearly dependent on the concentrations of NO_x and hydrocarbons or VOCs (e.g. Jacob, 1999). At low NO_x state, O_3 production rate is limited by, and therefore sensitive to NO_x. At high NO_x state, O_3 production rate is limited by the supply of VOCs, and at sufficiently high NO_x, even inhibited by any additional NO_x. Figure 1.1 shows O_3 concentrations at 16:00 LST as a function of NO_x and hydrocarbon emissions simulated using a two-layer box model (Sillman *et al.*, 1990; Jacob, 1999). The details of the box model see Sillman *et al.*, 1990. The ozone ridge line (thick line on the figure) separates the two different photochemical regimes. To the top-left of the line

is the NO_x-limited regime: O_3 concentrations increase with increasing NO_x and are less sensitive to hydrocarbons. To the bottom-right of the line is hydrocarbon-limited regime: O_3 concentrations increase with increasing hydrocarbons and decrease with increasing NO_x.

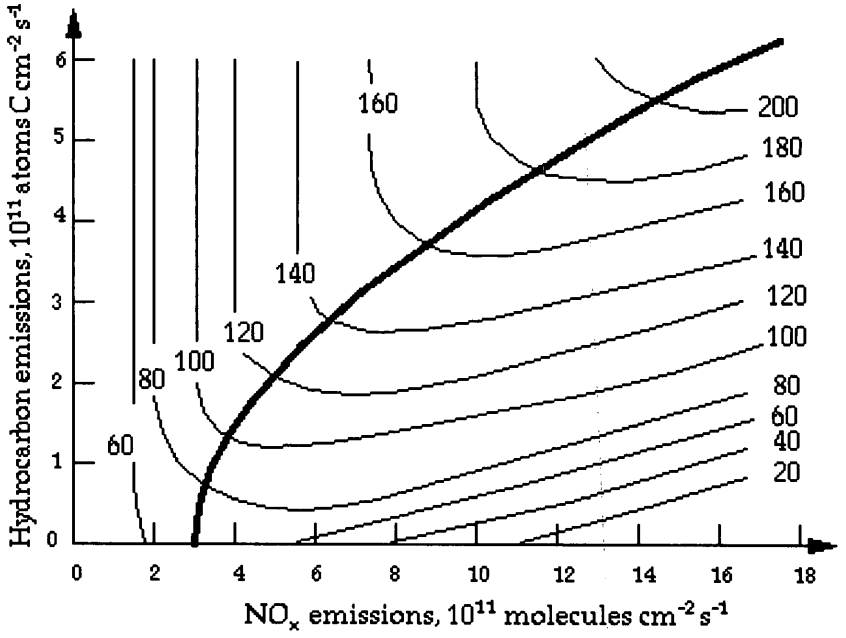

Figure 1.1: Ozone concentration (ppbv) at 16:00 LST simulated by a two-layer box model as a function of NO_x and hydrocarbon emissions. The thick line separates the NO_x-limited (top left) and hydrocarbon-limited (bottom right) regimes (Sillman *et al.*, 1990; Jacob, 1999).

The division between NO_x-sensitive and VOC-sensitive photochemical regimes is determined by the relative size of reactions (R1.13 - R1.12) (Sillman, 1995). When the formation of nitric acid (R1.12) represents the major sink of odd hydrogen radicals ($OH + HO_2 + RO_2$), OH must decrease with increasing NO_x, while VOCs are still sources of odd hydrogen (R1.7 - R1.10), OH will also increase slightly with increasing VOCs. The rate of O_3-producing reactions, being proportional to R1.7 and R1.8,

increases rapidly with increasing VOCs and decreases with increasing NO_x (ozone production is under the VOC-limited regime). When the formation peroxides (R1.13 and R1.14) represents the major sink of odd hydrogen radicals, then the concentration of HO_2 radical is fixed by the size of the odd hydrogen source and is independent of NO_x. The HO_2 concentration also shows little sensitivity to VOCs. The concentration OH is governed by the interconversion of OH, HO_2 and RO_2 (R1.7 - R1.10). OH increases with increasing NO_x (R1.10) and decreases with increasing VOCs (R1.8). The rate of O_3 production increases with increasing NO_x but is insensitive to VOCs (ozone production is under NO_x-limited regime).

Kleinman (1997) used a simple quantity of L_N/Q, the fraction of free radicals ($OH + HO_2 + RO_2$) removed by reactions with NO_x, to estimate the sensitivity of O_3 production to NO_x and VOCs. Here L_N is the loss rate due to all reactions of radicals with NO_x, and Q is total radical production rate. Free radicals are produced principally from photolysis reactions, and removed by two major categories of reactions: combination reactions between radicals (mainly R1.13 and R1.14) and reactions between radicals and NO_x (primary reaction R1.12). The conservation statement for free radicals can be written as,

$$Q = L_N + L_R$$

where L_R is the loss rate due to radical reactions, and is approximated as:

$$L_R \approx 2k_{eff}([HO_2] + [RO_2])^2$$

where k_{eff} is an effective rate constant for peroxide formation (Kleinman, 1997),

$$K_{eff} = k_{1.13}(1-\alpha)^2 + k_{1.14}(1-\alpha)\alpha$$

and

$$\alpha = [RO_2]/([HO_2] + [RO_2])$$

The evolution of an airmass from a high NO_x state with L_N/Q near 1 to a low NO_x state with L_N/Q near 0 due to chemical oxidation of VOCs and NO_x is accompanied by a transition between VOC sensitive O_3 to NO_x sensitive O_3 chemistry. In low NO_x as $L_N/Q \rightarrow 0$, it is assumed that radical loss by peroxide formation is equal to radical production (Kleinman, 2004), and O_3 production is approximated as:

$$P_{O_3} = K_t/(2k_{eff})^{1/2}Q^{1/2}[NO] \tag{1.34}$$

where P_{O_3} is the O_3 production rate, K_t is a composite rate constant for R1.10-R1.9. Under high NO_x, $L_N/Q \rightarrow 1$, and P_{O_3} is given by

$$P_{O_3} = Q\sum Y_i k_i[VOC_i]/k_{1.12}[NO_2] \tag{1.35}$$

where Y_i is the total number of peroxy radicals formed in R1.7 and R1.8, and assuming that they are all react with NO in R1.10-R1.9. K_i is the rate constant for reaction VOC_i with OH, and total OH reactivity with VOCs is defined as

$$VOC_R = \sum k_i[VOC_i]$$

Here the peroxide formation reactions (R1.13 and R1.14) can be ignored, and the reaction of OH with NO_2 (R1.12) is the predominant radical sink:

$$L_N \approx k_{1.12}[OH][NO2]$$

The O_3 production rate at high NO_x is approximated as

$$P_{O_3} = \sum Y_i k_i [VOC_i][OH] \tag{1.36}$$

The estimate of OH reactivity VOC_R is a measure of the local O_3 photochemical production. A simple expression for P_{O_3} valid at intermediate NO_x concentration is based on the relative sensitivity of P_{O_3} to NO_x and VOCs in terms of L_N/Q (Kleinman, 1997):

$$\frac{d\ln P_{O_3}}{d\ln[NO_x]} = \frac{1-3/2L_N/Q}{1-1/2L_N/Q} \tag{1.37}$$

$$\frac{d\ln P_{O_3}}{d\ln(VOC)} = \frac{1/2L_N/Q}{1-1/2L_N/Q} \tag{1.38}$$

Ozone production is said to be NO_x-limited at low [NOx] where $d\ln P_{O_3}/d\ln[NO_x] > d\ln P_{O_3}/d\ln[VOC]$, At high $[NO_x]$, $d\ln P_{O_3}/d\ln[VOC] > d\ln P_{O_3}/d\ln[NO_x]$, O_3 production is VOC-limited. The significance of L_N/Q is that it distinguishes low NO_x states in which radicals are removed by forming peroxides from high NO_x states in which radicals are removed by reactions with NO_x ((Kleinman, 1997). $L_N/Q = 1/2$ ($d\ln P_{O_3}/d\ln[NO_x] = d\ln P_{O_3}/d\ln[VOC] = 1/3$) indicates that the transition between NO_x and VOC-limited conditions, and O_3 production is equally sensitive to both NO_x and VOCs; at $L_N/Q = 2/3$ ($d\ln P_{O_3}/d\ln[NO_x] = 0$), O_3 production has a maximum value with respect to changes in NO_x concentrations (Kleinman, 2004).

The O_3 production is also sensitive to other factors, such as detailed VOC speciation and biogenic VOCs, the VOC/NOx ratio is not sufficient to establish O_3, NO_x and VOC sensitivity regime. Several species or species ratios were also used as indicators of NO_x or VOC sensitivity, total reactive nitrogen (NO_y), for an example, low values of afternoon NO_y (< 12 ppb) were consistently associated with NO_x-sensitive, and high values of NO_y (> 25 ppb) were associated with VOC-sensitive (Milford *et*

al., 1994). In addition, Sanford (1995) used correlations between the afternoon concentrations of various trace gases (e.g. O_3/NO_y, $O_3/(NO_y - NO_x)$, $HCHO/NO_y$, and H_2O_2/HNO_3) to determine the chemical sensitivity, which is considered NO_x-limited when the ratios are high and VOC-limited when the ratios are low. Martin *et al.* (2004) used tropospheric column amounts of $HCHO$ and NO_2 to estimate the transition between the VOC- and NO_x-limited regimes for the local O_3 production.

The O_3-NO_x-VOC sensitivity for individual locations and events are often highly uncertain. Ozone formation in Los Angeles is found to be strongly VOC-limited (e.g. Milford *et al.*, 1989; Harley *et al.*, 1993) and primarily VOC-limited in the San Francisco area (Steiner *et al.*, 2006) and in Phoenix (Kleinman *et al.* 2005). New York is typically VOC-limited (Kleinman *et al.*, 2000), although the urban plume likely becomes NO_x-limited at some point downwind (Sillman, 1995). Philadelphia and Houston appear to have mixed NO_x-VOC-limitations, VOC-limited in the morning and make a transition to NO_x-limited by the afternoon (Daum *et al.*, 2004; Kleinman *et al.*, 2005), while Atlanta is primarily NO_x-limited (Sillman *et al.*, 1995) with high surrounding biogenic emission. Mexico City is generally VOC-limited (Tie *et al.*, 2007, Lei *et al.*, 2007) and NO_x-inhibited in the workdays (Stephens *et al.*, 2010), and Shanghai is strongly VOC-limited (Tie *et al.*, 2009a). Overall, there is a tendency towards more VOC-limited conditions in urban centers and more NO_x-limited conditions in rural and suburban regions (Milford *et al.*, 1989, 1994).

1.3 Dust aerosol

Aerosol particles

Aerosol is defined as a suspension of solid or liquid particles in a gas (e.g. Seinfeld *et al.*, 2006). Aerosol particles in the atmosphere arise from natural sources, such as

windborne dust, seaspray, and volcanoes, and from anthropogenic activities, such as combustion of fuels. Aerosols may be emitted directly as particles into the atmosphere or formed by chemical reactions, as primary or secondary particles, respectively. Atmospheric aerosol particles exhibit a wide range of sizes, from nanometers to micrometers, and a range of shapes, and different chemical composition, and different optical properties. They can change their size and composition by condensation of vapor species or by evaporation, by coagulating with other particles, by chemical reaction, or by activation in the presence of water supersaturation to become fog and cloud droplets. Aerosols are removed from the atmosphere by dry and wet processes, deposition at the Earth's surface (dry deposition) and incorporation into cloud droplets during the formation of precipitation (wet deposition). Residence times of particles in the troposphere vary from a few days to a few weeks.

Fine aerosol particles, those with radius of less than 2.5 μm or $PM_{2.5}$, such as sulfate, nitrate, ammonium, organic carbon, elemental carbon, are almost all from condensation of precursor gases, which are produced during fossil fuel combustion, volcanoes, and other sources. Elemental carbon (also called black carbon or soot) is emitted directly into the atmosphere, predominantly from incomplete combustion of carbonaceous material. Coarse particles (> 2.5 μm in radius), including sea salt, soil dust, and vegetation debris, are mainly formed by wind, and usually are contributed from both natural and human-made sources. Human activities include land use practice and construction.

Dust particles

Dust is the suppression of solid particles with radius less than 1000 micrometers or PM_{10}, Dust particles in the atmosphere arise from various sources such as soil dust lifted up by wind, volcanic eruptions, and pollution. Soil-derived dust particles emit mainly from arid and semi-arid surface and soil degradation through wind erosion.

Emissions of dust are dependent on surface properties (e.g. texture, roughness, composition, moisture, and vegetation), and also depend strongly on wind speed. The average lifetime of dust particles in the atmosphere is about 2 weeks. Dust is considered an aerosol in the coarse mode, and is often the major components of aerosols. Globally, dust emission is the second largest after sea salt, and accounts for one third to one half of total annual aerosol emissions by mass (e.g. Penner *et al.* 2001).

Dust particles can have significant effects on solar radiation, climate, and photochemistry in the troposphere. For example, dust contributes significantly to shortwave scattering and absorbing (Tegen and Lacis, 1996), resulting in visibility reduction and changes in surface temperature and atmospheric heating rates (Miller *et al.* 2004). The reduction of solar radiation can also significantly affect atmospheric photochemistry on global scale (He and Carmichael, 1999; Perlwitz *et al.*, 2001); Bian and Zender, 2003; Tie *et al.*, 2005; and Bian *et al.*, 2007) and regional scale (Zhang *et al.*, 2009). and dust particles cause significant reductions in OH and O_3 in dust dominated regions. Dust particles exhibit large regional and seasonal variations, and dust plumes containing small particles can travel thousands of kilometers and may dominate the light scattering downwind of dust source regions (Chiapello *et al.*, 1999). In addition, dust particles have important influence on cloud formation and properties (Wurzler *et al.*, 2000, Ansmann *et al.*, 2005). Dust particles can also have a significant impact on the chemistry by providing a large surface for heterogeneous reactions (e.g. Dentener *et al.*, 1996). Dust particles absorb HNO_3, for an example, and substantially reduce the O_3 precursor NO_x. Due to reactions on soil dust, O_3 was calculated to decrease by 10% nearby the dust source areas.

Despite the progress of previous studies for dust formation and distributions, and dust-induced O_3 variation, dust is still poorly characterized in global and regional models, especially on regional scales. For example, the dust properties remain poorly quantified in the Mexico City area.

1.4 Air pollution in the Mexico City area

Mexico City (MC) is one of the largest megacities in the world. During the twentieth century the Mexico City metropolitan area (MCMA) experienced huge increases in population and urbanized area. The population grew from fewer than 3 million in 1950 to over 18 million in 2000. The urbanized area within the MC region has increased by a factor of 13, from just 120 km^2 in 1940 to 1500 km^2 by 1995 - representing about 30% of the metropolitan area were urbanized. In this geographical setting, nearly 20 million residents, over 3.5 million vehicles and over 40,000 industries consume daily more than 40 million liters of fuel. Stationary and mobile fossil fuel combustion sources produce thousands of tons of directly emitted pollutants that react in the atmosphere to generate secondary pollutants (Molina *et al.*, 2007). Mexico City has become a megacity with severe air pollution problems. The urban emissions also significantly influence air quality on the regional scale (Mena- Carrasco et al., 2009).

1.4.1 Ozone episodes

The MC area (centered around 19°25′N and 99°10′ W) lies within an elevated basin at an average altitude of 2 km above mean sea level (MSL). The approximately 50×50 km^2 nearly flat basin (like a U shape) is surrounded on the three sides (east, south and west) by high mountains with average height over 3 km above MSL, but with a broad opening to the north and a narrower gap to the south-southwest in the mountainous terrain (see Fig. 1.2). The urban area is ringed by mountains, and experiences frequent thermal inversions (Fast and Zhong, 1998). Thermal inversions can trap pollutants within the basin that is enclosed by mountains. The mountain ranges tend to restrict pollutant dispersion. Because of its tropical latitude and high altitude, Mexico City receives the intense sunlight during the whole year, which promotes photochemical activity and drives the production of ozone and secondary particulate

matter. The unique topography and meteorology of MC basin also contributes to the intensification of its air pollution (see Fig. 1.3).

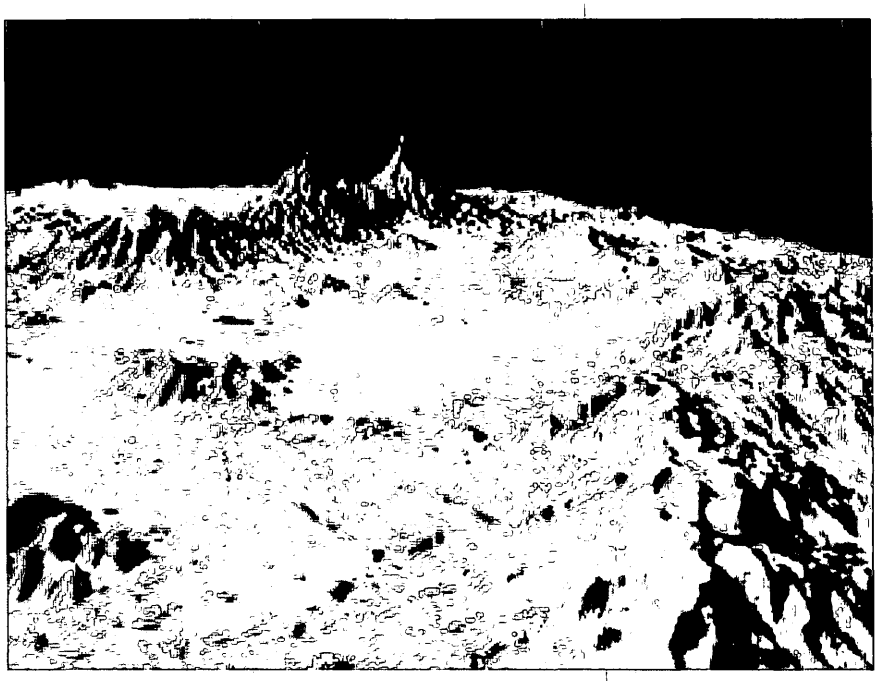

Figure 1.2: The topography (computer generated) of the MC basin: showing topography height from 2-4 km above MSL (see also Fig. 2.2); and about 100 km in the horizontal directions.

In contrast to midlatitude megacities, ozone exceedances in the MC area can occur during the winter as well as the summer; and air pollution is even worse in the winter when rain is less common and thermal inversions are more frequent (Molina and Molina, 2002). Hourly averaged ozone concentrations in the MC area exceed the Mexican air quality standard of 110 ppbv almost every day at one or more stations and often exceed twice the standard. Ozone concentrations as high as 441 ppbv have been measured during the most severe air pollution events.

Much research has been under taken to study meteorology and the air pollution of the MC area. For examples, Bossert (1997) studied the meteorological systems

Figure 1.3: The air pollution over the MC basin during the 2006 MILAGRO field campaign. Photo by C. McNaughton.

and showed that both regional and synoptic scale flows affect the MC basin: Mexico City is subjected to the influence of thermally driven, terrain-induced diurnal thermal mesoscale wind circulation that dominates the dispersion and transport of pollutants: upslope during the day and downslope during the night. de Foy *et al.* (2005, 2006a) discussed the wind circulation patterns in the MC basin due to the interaction of the gap winds with the synoptic flow and three different convergence patterns were analyzed according to three ozone episode types (O_3-South, Cold Surge, and O_3-North) during MCMA-2003. Under these three different meteorological conditions in Mexico City, ozone photochemical formation is characterized and ozone sensitivity to emission changes is discussed in Lei *et al.* (2007, 2008). In addition, three extra meteorological episode types, O_3-South Venting (O_3-SV), O_3-Convection South (O_3-CnvS) and O_3-Convection North (O_3-CnvN) were identified to account for meteorological conditions during 2006 MILAGRO experiment (de Foy et al., 2008). Days with the poorest air quality were often associated with the strongest vertical

wind shear. In contrast, persistent southerly winds likely contributed to low pollutant concentrations in the basin. The diurnal variations of air pollutants were consistent with the boundary layer growth (Tie *et al.*, 2007, Herndon *et al.*, 2008). The oxidation of alkenes and aromatic hydrocarbons dominated the O_3 production in the MC area (Tie *et al.*, 2007), while the regional (with a diameter of 500 km - 1000 km) OH reactivity and ozone production is dominated by oxygenated VOCs and CO (Tie *et al.*, 2009, Emmons *et al.*, 2010).

1.4.2 Ozone production and sensitivity

Both model sensitivity simulations and measurement analysis indicate that ozone production in the MC area is generally VOC-limited in the urban area. Tie *et al.* (2007) investigated the ozone sensitivity to changes in magnitudes of HCs and NO_x emissions, suggested that Mexico City is under VOC-limited regime. Both simulated behavior of O_3 production and its sensitivities to reduction in precursor emissions suggest that mid-day O_3 formation is VOC-sensitive in the urban region (Lei *et al.*, 2007). Sensitivity analysis of O_3 production to precursor emissions under different meteorological conditions during MILAGRO, along with chemical indicator analysis using H_2O_2/HNO_3, illustrated that the MC urban core area is VOC-limited for all meteorological episodes, while the surrounding areas with relatively low-NO_x emissions can be either NO_x- or VOC-limited regime depending on the meteorology (Song *et al.*, 2009).

A comparison of calculated radical production rates with the observed production rate of NO_z suggest that O_3 production in the MC area is VOC-limited (Wood *et al.*, 2009). Lower mixing ratios of hydrogen peroxide was measured during 2006 MILAGRO field campaign in Mexico, which is consistent with low or negative net

peroxide production rates due to high NO_x concentrations in the MC area, also indicated that VOC-limited regime (Nunnermacker *et al.*, 2008). An analysis of weekly patterns of surface concentrations of CO, NO_x, PM_{10}, and O_3, shows a clear weekend effect, which provides empirical evidence that O_3 production is VOC-limited and NO_x-inhibited during workday (Stephenes *et al.*, 2008). Decreases in the concentrations of CO and VOCs over the past decade have increased the ratios of NO_x/CO and NO_x/VOC, and increased the VOC-limitation of O_3 production in the urban area. Furthermore, meteorological conditions led to large variations in the regime for the relatively low-NO_x emission area (Song *et al.*, 2010).

1.4.3 Dust events

As a result of drying of lakes and deforestation in the twentieth century, dust storms were very common phenomena in the MCMA even in the sixties, especially during the dry season (e.g. Molina and Molina, 2002). Several projects have been implemented to recover and protect conservation land and to increase the vegetation cover, soil erosion is still the major source of PM_{10} in the MCMA (40% of the total PM_{10} emissions). During the 2006 MILAGRO (Megacity Initiative: Local and Global Research Observations) field campaign (http://www.eol.ucar.edu/projects/milagro), extensive dust events were often observed (see Fig. 1.4).

Chow *et al.* (2002) reported that PM_{10} concentrations were highly variable location by location, and that dust was the major cause of PM_{10} differences, and geological material is the largest component of PM_{10}, constituting ~50% of PM_{10} mass. Querol *et al.* (2008) found that soil matter accounted for 25-27% of PM_{10} at the urban sites and a larger fraction (up to 43%) at the suburban and rural sites. They also found that soil matter accounted for 15% and 28% of the $PM_{2.5}$ at the urban and rural sites. Dust was one of the most important particulate sources in the urban

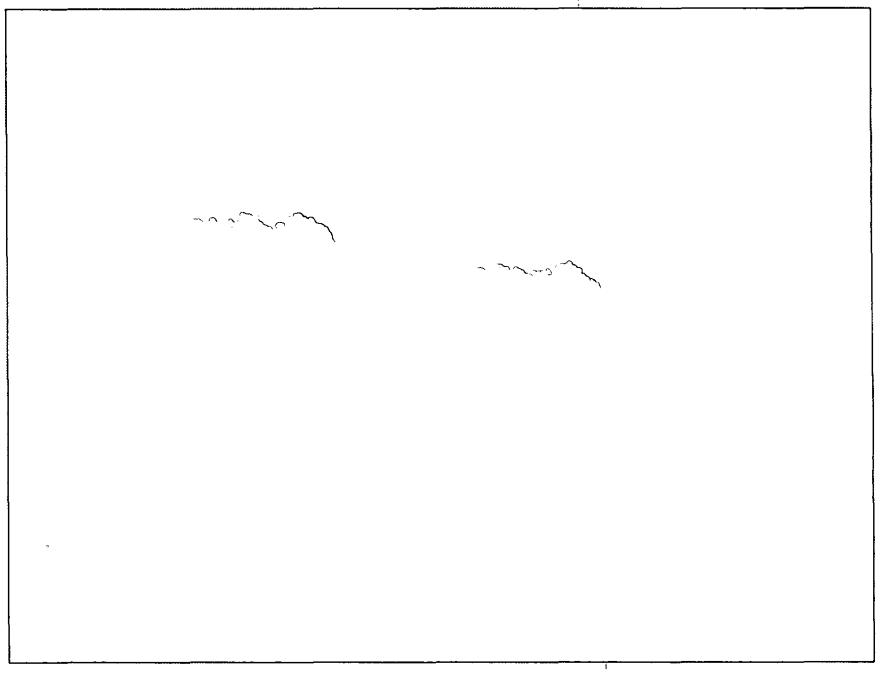

Figure 1.4: A typical dust event in the Mexico City region. The photo was taken by S. Springston from the G-1 aircraft on March 18, 2006 during the MILAGRO field experiment.

site, with 26% contribution during the MILAGRO campaign (Mugica *et al.*, 2009). The most important source of dust emissions are probably the dry lakebeds, located at the northern part of metropolitan area (Molina and Molina, 2002). Díaz-Nigenda *et al.* (2010) found that wind-erosion is a major cause of high PM_{10} concentrations in Mexico City, and the dry lake of Texcoco and agricultural lands to the east and southeast of Mexico City is the most important dust source that affects the northeast part of the city.

1.4.4 Meteorological conditions

The Mexico City basin meteorology is usually classified into *three seasons*: the *cold dry season* from November to February, the *warm dry season* from March to April, and the *rainy season* from May to October (de Foy *et al.*, 2005). During the *dry*

winter months (November to April), the prevailing meteorology consists of high pressure systems, light winds above the basin and nearly cloudless skies. This leads to the development of strong surface-based thermal inversions at night that persist for several hours following sunrise. Thus there is sufficient time for the photochemical formation of ozone in the morning, before the development of the deeper mixed layers by the afternoon.

The *warm dry season* (March - May) is also the biomass burning season; many fires occur in the pine forests on the mountains surrounding the city, both inside and outside the basin. Typically, the biomass burning intensifies in late March, reaching a maximum in May (Fast *et al.*, 2007).

During the *wet summer months* (June to September especially), moist easterly flow over Mexico City brings in ample tropical moisture from the Gulf of Mexico with frequent cloudiness and rainfall. Clouds inhibit photochemistry and rainfall removes trace gases and particulates from the air. Thus extremely high ozone episodes and dust events are less frequent during the wet summer months.

1.4.5 Air quality trends

The air pollution problem in the Mexico City region has been well recognized as a major social concern since 1970s (Molina and Molina, 2002), and significant progress has been made on improving air quality in the MC area during the past decade (Molina it et al., 2010). Figure 1.5 shows the air quality trends for the MC area from Stephenes *et al.* (2008), where the morning maximum of CO and the afternoon maximum of O_3 decreased in the early 1990s, and continued to decline in the 2000s; while the morning maxima of NO_x and PM_{10} show little or no change in the last decade. Although substantial reductions in the concentrations of lead, sulfur dioxide (SO_2) and carbon monoxide (CO) were achieved, the concentrations of ozone, nitrogen oxides, and

particulate matters still remain exceeding the air quality standards (Molina *et al.*, 2010).

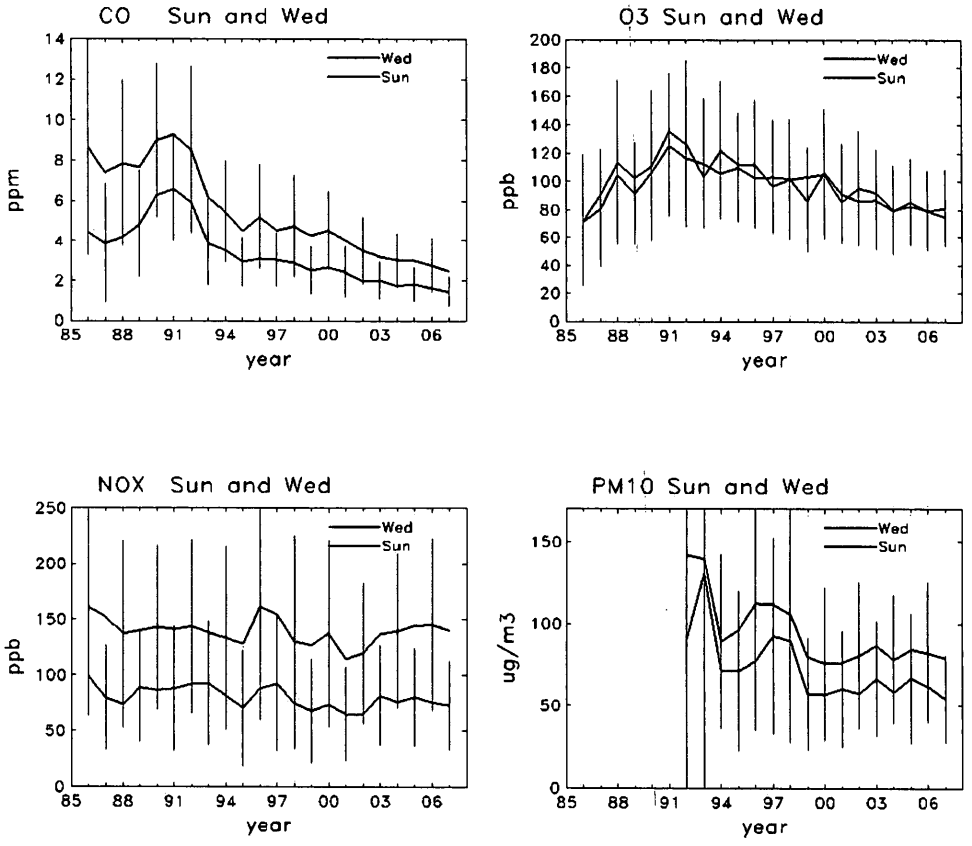

Figure 1.5: Long term trends in the concentrations of CO, NO_x, and PM_{10} in the morning (average of the three highest concentrations between 7 AM and 12 noon) and O_3 in the afternoon (average of the three highest concentrations between 11 AM and 5 PM) averaged over all stations for Wednesdays (red lines) and Sundays (blue lines). From Stephenes *et al.* (2008).

1.5 MILAGRO field experiments

As one of the most highly populated and polluted cities in the world, with unique meteorology and topography, Mexico City has been the location of many air pollution field studies. The Mexico City Air Quality Research Initiative (MARI) project

gathered surface and vertical profile observations of meteorology and pollutants during 1990-1994 (LANL/IMP, 1994; Streit and Guzman, 1996). The IMADA-AVER (Investigació n sobre Materia Particulada y Deterioro Atmosférico, Aerosol and Visibility Evaluation Research) campaign in February-March 1997 yielded comprehensive meteorological measurements in the basin, and provided insights into particulate composition (IMP, 1998; Doran *et al.*, 1998; Edgerton *et al.*, 1999; Molina and Molina, 2002). The MCMA-2003 measurement campaign was carried out during April 2003, a better understanding of the emission sources, ozone formation and its sensitivity to VOCs and NO_x, and the composition, size distribution and atmospheric mass loadings of both primary and secondary fine PM were obtained (Molina *et al.*, 2007).

MILAGRO (Megacity Initiative: Local and Global Research Observations) field campaign (website: http://www.eol.ucar.edu/projects/milagro) is an international collaborative project to examine properties, evolution, and export of atmospheric emission from a megacity. Mexico City, the second largest megacity in the world and most populous city in North America, was selected as the case study to characterize the sources, concentrations, transport, and transformations of the gases and fine particles emitted to the MC's atmosphere, and to evaluate the regional and global impacts of these emissions (Molina *et al.*, 2010). There are 4 coordinated components (MCMA-2006, Max-Mex, MIRAGE-Mex, and INTEX-B) that took place simultaneously during March 2006, and each component has different science objectives and different interesting and geographic coverage area. Figure 1.6 shows the geographic coverage area in the MILAGRO campaign. The MCMA-2006 (Mexico City Metropolitan Area - 2006 experiment) focused on the emissions and surface concentrations within the Mexico City basin; Max-Mex (Megacity Aerosol Experiment: Mexico City) focused on the aerosol evolution during transport, and the chemical and physical nature of the aerosol affected scattering and absorption of atmospheric radiation; MIRAGE-Mex (Megacity Impacts on Regional and Global Environments -

Mexico) examined the chemical/physical transformations of gaseous and particulate pollutants exported from Mexico City; INTEX-B (Intercontinental Chemical Transport Experiment-B) was to investigate and understand the transport and transformation of gases and aerosols on transcontinental/intercontinental scales and to assess their impact on air quality and climate.

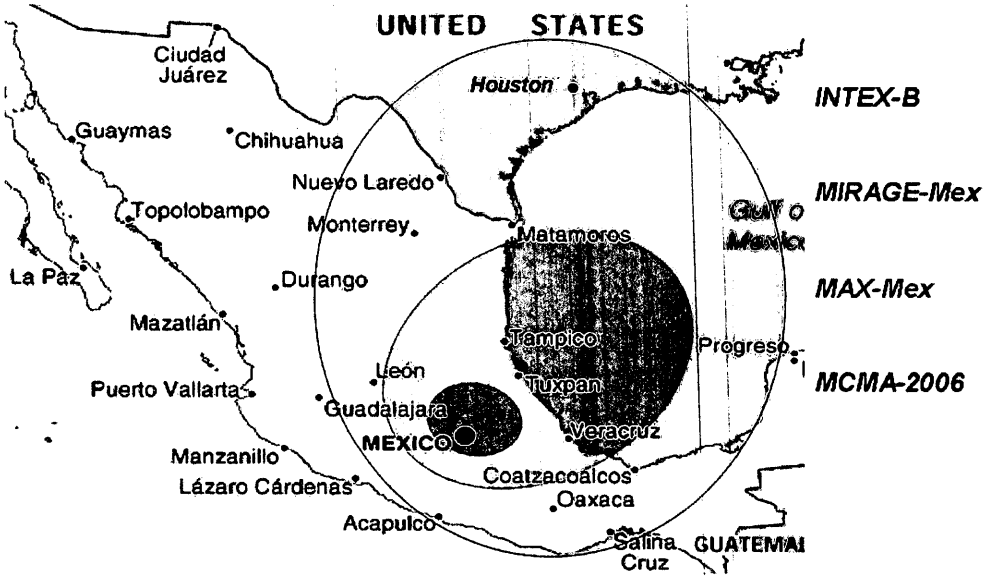

Figure 1.6: Geographic coverage for MILAGRO campaign. The size of the circle indicates the geographic coverage for the four coordinated components.

The measurement of MILAGRO experiment consisted of a month-long series of carefully coordinated observations of the chemistry and physics of the atmosphere in and near Mexico City during 2006, using a wide of instruments at ground sites, on aircraft and satellites. Three ground supersites (T0, T1, T2), spaced about 30 km apart, were setup to examine the evolution of the pollutants (primary emitted gases and fine particles) exported from urban areas (Molina *et al.*, 2010). The aircraft measurement data provide a unique opportunity to evaluate the interaction between emission, meteorology and chemistry near and further from the urban center. During

the MILAGRO campaign, a rich array of aircraft measurements of gases and aerosols were obtained, and were applied in evaluating model performance and interpreting the O_3 formation, evolution and transport in the urban plume from Mexico City (e.g., Tie *et al.*, 2009, Song, *et al.*, 2010).

The month of March was selected for the field campaign because of the dry, mostly sunny conditions observed over central Mexico at this time of the year. Clouds and precipitation that usually increased during April, and the synoptic conditions during March were representative of the warm dry season (de Foy *et al.* 2008).

1.6 Objectives of this research

This research is a numerical study of the air pollution in the Mexico City (MC) area using the WRF/Chem Model during the period of the 2006 MILAGRO experiments, especially the changes in O_3 concentrations caused by variations of surface emissions and dust effect. The following aspects are to be discussed: (1) characterization of chemical oxidants and sensitivity of O_3 to NO_x and VOCs; (2) the impact of the diurnal variations of surface emissions (NO_x and VOCs) on O_3 concentrations; and (3) the effects of dust, especially dust particles originated from the large dry land areas northeast of the MC, on total aerosol mass and ozone concentrations.

Chapter 2

Numerical Model and Simulations

This chapter briefly describes the WRF/Chem model and the model configurations used in this study. The initial and boundary conditions for meteorological fields and chemical species, the surface anthropogenic and biogenic emissions for gas-phase species, and primary emissions for fine particular matters; and the surface measurement of RAMA network and the MILAGRO field experiment are also presented.

2.1 The WRF/Chem model

The Weather Research and Forecasting (WRF) model with online chemistry, or the WRF/Chem model, is used in this study. The model simulates the emission, transport, mixing, and chemical transformation of trace gases and aerosols simultaneously with the meteorology. The WRF/Chem model is flexible, with multiple choice of gas-phase chemistry, photolysis schemes, and aerosol models, or it can be used as a transport model. The biogenic emissions can either be calculated online using different modules of biogenic emissions (such as Guenther *et al., 1994* emissions, or MEGAN (Model of Emissions of Gases and Aerosols from Nature) (Guenther *et al.,*

2006), or be turned off. A brief description of the WRF/Chem model is given in Appendix A.

WRF/Chem model is widely used to examine the meteorological conditions, chemical species, aerosols in different regions, for examples , in Mexico City (.e.g. Tie *et al.*, 2007, Barnard *et al.*, 2010), in Houston (Fast *et al.*, 2006), in Shanghai (Tie *et al.*, 2009a), and in Hongkong (Jiang *et al.*, 2008). Chapman *et al.* (2006) used the WRF/Chem model to investigate the local and regional influence of elevated point sources on summertime aerosol forcing and cloud-aerosol interactions in northeastern North America. In general, the synoptic-scale circulations are simulated reasonably well by WRF model, although the details (i.e., timing and strength) of local and regional winds affected by terrain variations around Mexico City are more difficult to reproduce by model (e.g., Fast et al., 2009; Hodzic et al., 2009). The diurnal variation in the simulated boundary layer depth was similar to observation; however, relatively large errors were produced during the afternoon and at night, which will affect predicted dilution of trace gases and aerosols. Simulated primary organic aerosols (POA) were consistently lower than the measured organic matter at the ground sites, which is consistent with the large underestimation of the secondary organic aerosol (SOA) production by WRF model in polluted region (Fast et al., 2009; Hodzic et al., 2009).

There are several off-line chemistry models, such as the Comprehensive Air Quality Model with Extensions (CAMx) (Lei *et al.*, 2007; Song *et al.*, 2010) and the Community Multiscale Air Quality modeling system (CMAQ) (Herwehei *et al.*, 2011). As WRF/Chem, MC2AQ, a Canadian regional air quality model, is driven on-line by a mesoscale compressible community meteorological model (MC2), which includes complex oxidant gas-phase chemistry, deposition, anthropogenic and on-line biogenic emissions. MC2AQ (no longer used) has been used successfully to simulate O_3 concentrations in Eastern Canada and the United States and also for Europe

(Plummer *et al.*, 2001; Yang *et al.*, 2003). But MC2AQ model did not have multi-choices of gas-phase chemical mechanisms, photolysis schemes, it did not include an aerosol module.

2.2 Model configurations

The model in this study includes online dynamics and physics calculations, transport, dry deposition (Wesely, 1989), gas phase chemistry, photolysis (Madronich and Flocke, 1999, Tie *et al.*, 2003), and on-line calculation of biogenic emissions (Guenther *et al.* 1994). The gas-phase chemistry is represented by the modified RADM2 (Regional Acid Deposition Model, version 2) gas-phase chemical mechanism (Chang *et al.*, 1987; Stockwell *et al.*, 1990) which includes 57 chemical species and 158 gas-phase reactions, of which 21 are photolytic. More details can be found in http://www.epa.gov/asmdnerl/CMAQ/ch08.pdf. EPA (Environmental Protection Agency) Community Multiscale Air Quality (CMAQ)/Models-3 aerosol module (details can be found in the website: http://www.cmaq-model.org) was added in the model. The photolysis rates is calculated using the fast Tropospheric Ultraviolet-Visible (FTUV) radiation model, that takes into account the impact of the simulated clouds and aerosols (see Appendix A). Some of physics options chosen are: Purdue Lin et al. microphysics scheme (Lin *et al.*, 1983), Yonsei University PBL scheme (Hong *et al.*, 2006), Noah land-surface model (LSM) (Chen and Dudhia, 2001), RRTM long-wave radiation (Mlawer *et al.*, 1997), and MM5 (Dudhia) Shortwave scheme (Dudhia, 1989).

The model domain is 660km $\times$ 660km centered in Mexico City, with horizontal resolution of 6 km and 28 non-uniform vertical levels up to 50 mb. The model resolution has important effects on the simulated O_3 and its chemical precursors. Their concentrations simulated with 3 km and 6 km resolutions, are generally in agreement

with the measured concentrations. There are less noticeable differences between the simulated results for 3 km and 6 km resolutions. Considering the model performance and required computation time, the 6 km resolution is an optimal resolution for the simulation of O_3 and its precursors in Mexico City (Tie *et al.*, 2010). The time step used in simulation is 30 seconds (see Appendix A for a discussion of timestep limits). Each simulation started at 0000 UTC (1800 LST) and integrated for 30 hour model time, the results of the first 6 hours were not used in the analysis. The meteorological fields were re-initialized every 24 hours. The chemistry was spun-up for 4 days: 4-day prior to the simulation period was used for model "spin-up", and results of these days are not included. The chemical fields used previous 24-hour simulations, and continued throughout the length of the simulation.

The simulation time periods were selected in March 2006 during MILAGRO experiment. A few days with high concentrations of O_3, March 12-15, 2006, were chosen as the simulation periods for photochemical air pollution in chapter 3 and chapter 4. Dust event days during March 16-20, 2006 were chosen as dust simulation periods in Chapter 5.

2.3 Initial and lateral boundary conditions

The geophysical data are derived from the two-dimensional global geophysical data (see *http://www.mmm.ucar.edu/wrf/users/download/get_sources.htm*). These datasets include topography height, 24-category USGS landuse, 16-category top-layer soil types and 16-category bottom-layer soil types, with resolutions of 30-arcsecond, 2-arcminute, 5-arcminute and 10-arcminute; and monthly vegetation fraction and monthly surface albedo (10-arcminute); and annual mean deep soil temperature, maximum snow albedo and 14-category slope index (1-degree).

The meteorological initial and boundary conditions use the NCEP (National Centers for Environmental Prediction) global Final (FNL) analysis (6 hour intervals with 1-degree horizontal resolution and 26 vertical levels from 1000 mb to 10 mb). Details of the data can be found at *http://dss.ucar.edu/datasets/ds083.2/data*. Considering the WRF three-dimensional variational (3D-VAR) data assimilation system (Barker *et al.*, 2004) may refine the local flow, which dominates the dust transport, the initial and boundary conditions of meteorological fields were re-calculated by using the WRF 3D-VAR data assimilation system in the dust simulations in chapter 5.

The chemical initial conditions are from the spun-up simulations, which were initialized by using idealized profile. After 4-day spin-up runs (every run starts from previous 24-hour simulations), the magnitudes, diurnal cycles, and the distributions of the chemical species get their balance. The chemical boundary conditions are derived from the simulations of the Model for OZone And Related chemical Tracers model, version 4 (MOZART-4). The MOZART model is a comprehensive global chemical transport model developed at NCAR (see Horowitz *et al.*, 2003 and *http://www.acd.ucar.edu/gctm/mozart* for model details). The data used here were 3-hour averages from MOZART-4 simulations with the 0.7-degree horizontal resolution. The MOZART-4 simulations of O_3, CO and NO_x agree well with observations, but the model substantially underestimates oxygenated VOCs (Emmons *et al.*, 2010).

2.4 Surface emissions

Megacities, such as Mexico City, produce a complex array of emissions including hundreds of different VOCs. As most large cities, the transportation emissions in Mexico City are responsible for substantial levels of CO, NO_x, and a number of high reactive aromatic and olefinic VOCs. According to the government's 2002 emission inventory, mobile sources contribute over 99% of all CO, 84% of NO_x, 39% of hydrocarbons

(HCs), 58% of SO_2, and 52% $PM_{2.5}$, 19% PM_{10} emitted in the Mexico City area (Jiang *et al.*, 2005).

Non-methane hydrocarbons (NMHCs) have primary anthropogenic emission sources which can include evaporative, exhaust, industrial, biogenic, and biomass burning emissions. Motor vehicles are the predominant daytime source of aromatic hydrocarbons, while wood and garbage burning are important nighttime sources (Marr *et al.* 2006). Sources of oxygenated volatile organic compounds (OVOCs) include primary anthropogenic emissions, primary biogenic emissions, biomass burning, and secondary photochemical formation from anthropogenic, biogenic, and biomass burning sources. Aldehydes result from fossil fuel combustion and are formed from the oxidation of primary NMHCs (Atkinson, 1990). Glyoxal is mostly formed from VOC oxidation (Volkamer *et al.*, 2005). Garcia *et al.* (2006) estimated the formaldehyde ($HCHO$) levels due to mobile emission and photochemical production of VOCs, and found that 40% of $HCHO$ can be attributed to emissions and 38% to photochemical production. The emission source is dominant in the early morning, later afternoon and at night, while the photochemical source becomes dominant later in the morning and be the largest daytime sources, producing up to 80% of $HCHO$ in few hours around noon.

Overall, major VOCs in terms of ozone production in the Mexico City are of anthropogenic origin from vehicles. Biomass burning is a minor source of VOCs (e.g. de Gouw *et al.*, 2009), and biogenic VOCs seem to be relatively insignificant, the biogenic component of VOC emissions has been estimated to contribute no more than 7% in the valley of Mexico (Velasco *et al.* 2007).

Anthropogenic emissions for gas-phase species

Hourly surface emission data for primary chemical species (SO_2, CO, NO_x, NH_3) and 14 lumped RADM2 non-methane VOCs (ETH, HC3, HC5, HC8, OL2, OLT,

OLI, ISO, TOL, XYL, CSL, HCHO, ALD and KET, see Appendix A for details) were implemented in the model. The emission rates were based on anthropogenic inventory for Mexico City and for the surrounding area (Garcia, 2004). The inventory contains temporal, spatial, and detailed chemical composition of emissions from anthropogenic sources. In this inventory, in addition to the emissions from Mexico City, the emissions from small cities in the surrounding area are also estimated by assuming that emissions are proportional to the population density. The emission rates for lumped NMVOCs (non-methane VOCs) in this study were evaluated and adjusted according to the average ambient concentrations of major NMHCs measured during MCMA-2002 and 2003 studies at urban, rural and industrial sites of the Valley of Mexico (Velasco *et al.*, 2007). For alkanes, the emission rate of HC8 is increased by 150%; The emission rates of alkenes are increased by 20% for OL2, and 5% for OLT; There is also 60% increase for the emission rate of TOL. The total VOC emissions increase by about 9% after the adjustment.

The emission inventory for primary chemical species is summarized in Table 2.1, and the detailed emissions for each NMVOC species are shown in Table 2.2. It can also been seen that there is a small amount of isoprene emission (5,389 tons/yr) in the MC area, which is consistent with results that most of the isoprene observed in the urban area is likely of anthropogenic origin (Hodzic *et al.*, 2009). Figure 2.1 illustrates the diurnal cycles of the emissions (10 NMHCs along with CO and NO_x) at the center of Mexico City, and the horizontal distribution of the estimated NO emission rate at 0800 LST in Mexico City and its surrounding area is shown in Fig. 2.2.

Biogenic emissions

The biogenic emission is calculated online (Guenther *at al.*, 1994), see Appendix A for detailed description. The estimated domain total biogenic emissions for nitrogen, isoprene, monoterpenes, and other VOCs (OVOC) are shown in Table 2.3, which are

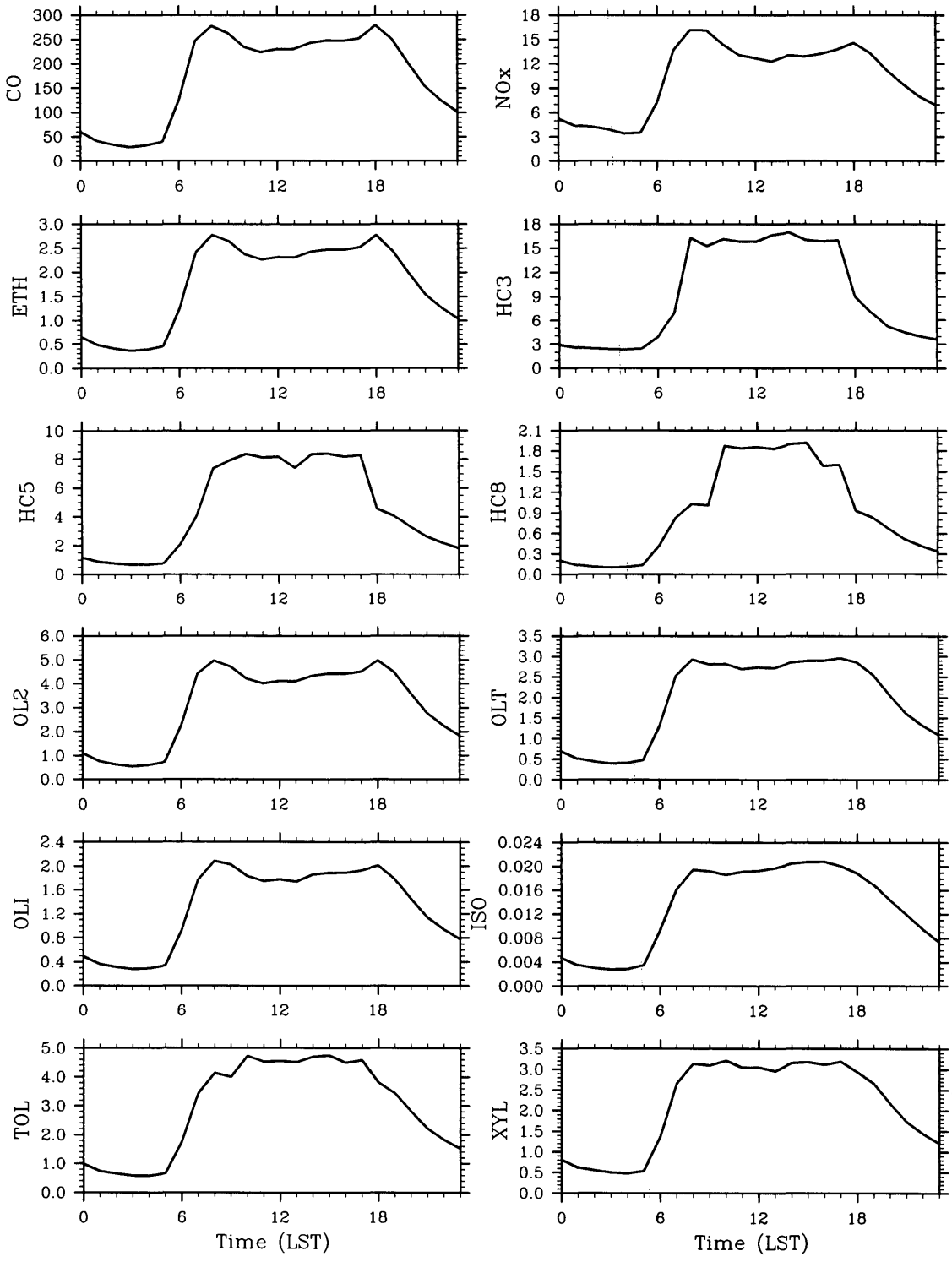

Figure 2.1: The diurnal cycles of the estimated emission rates (mole/s) over the grid cell of 6km × 6km at a site (99.14 W, 19.43 N) in Mexico City.

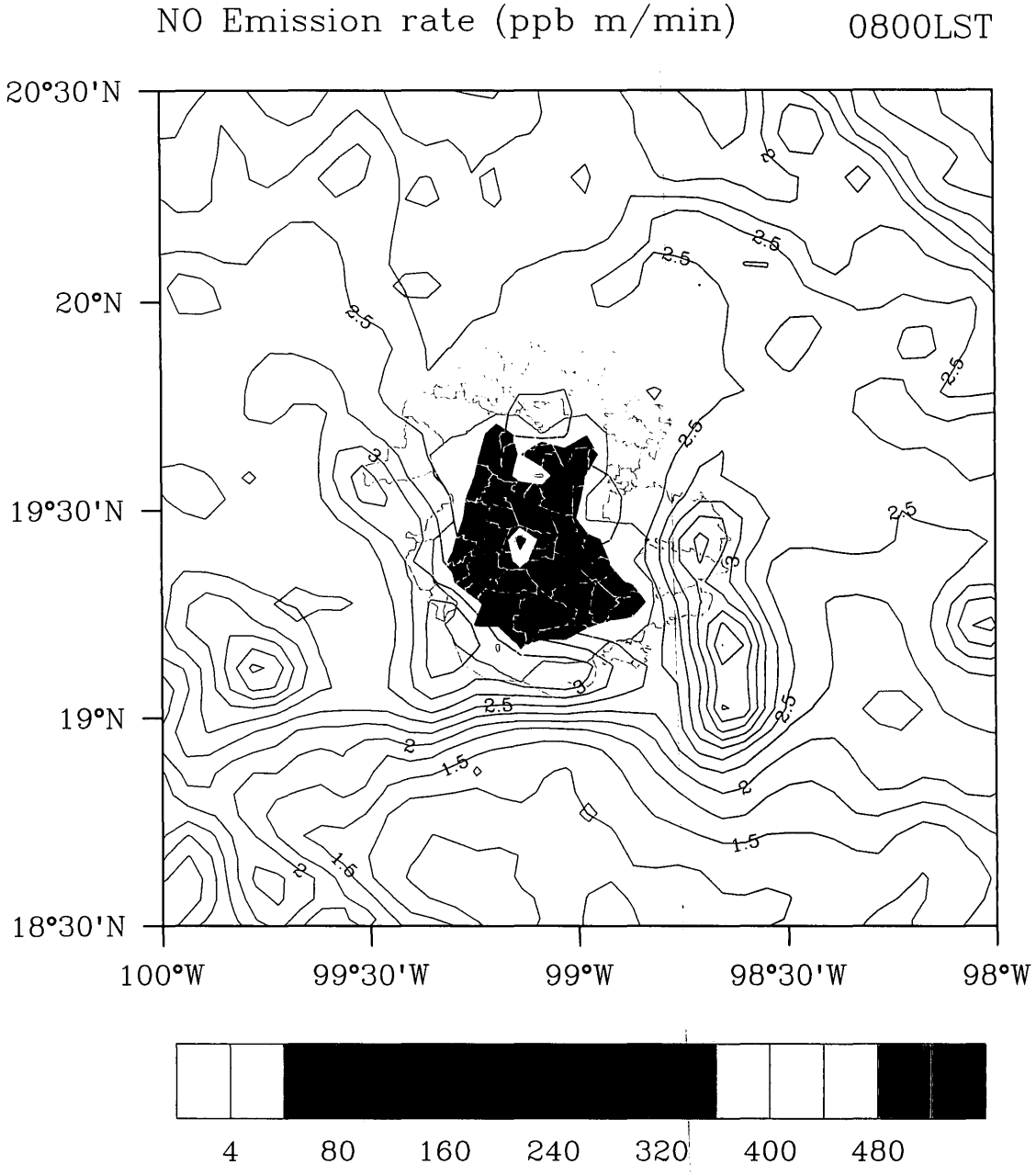

Figure 2.2: Spatial distribution of the *NO* emission rate (mole/s) at 0800 LST with grid cell of 6km × 6km in Mexico City and the surrounding area. The contour lines show the terrain height around MC area, with contours (km) from 1 to 4 by 0.25.

Table 2.1: Anthropogenic emission inventories (tons/yr) for Mexico City and the surrounding area

	SO_2	CO	NO_x	VOCs
Mexico City (MC)	2.09×10^4	2.19×10^6	1.57×10^5	1.17×10^6
MC & surrounding area	2.94×10^4	2.31×10^6	1.71×10^5	1.20×10^6

based on the model calculated results on March 12, 2006. The spatial distribution of the calculated biogenic isoprene emission rate on March 12, 2006 are also shown in Fig. 2.3.

Anthropogenic emissions for fine aerosol particles

The chemical composition for primary emissions of fine aerosol particles ($PM_{2.5}$) in the MC area is shown in Fig. 2.4, in which $PM_{2.5}$ is dominated by carbonaceous particles, which account for nearly 60% of the anthropogenic aerosol emissions [40% organic carbon (OC) and 16% elemental carbon (EC)], consistent with the finding by Kleinman *et al.* (2008) that carbonaceous aerosols have large contributions to anthropogenic aerosols in the MC region. Nitrates and sulfates account for 10 % and 11 %, respectively, and the remaining 23 % are classified as the un-speciated primary $PM_{2.5}$.

2.5 Surface measurements

The air pollutant and meteorological fields in the Mexico City area have been monitored routinely since 1986 by the RAMA (Red Automática de Monitoreo Atmosférico) network (see website: http://www.sma.df.gob.mx/simat/pnrama2.htm). The RAMA provides hourly average near-surface measurements of criteria gases (CO, O_3, SO_2

Table 2.2: NMVOC anthropogenic emission inventories (tons/yr) for MC & the surrounding area

	Mexico City (MC)	MC & surrounding area	%
ETH	25,199	26,027	2.16
HC3	339,085	350,143	29.09
HC5	222,134	229,389	19.06
HC8	71,013	73,329	6.09
OL2	39,671	40,963	3.40
OLT	41,206	42,541	3.53
OLI	36,656	37,840	3.14
ISO	5,389	5,389	0.46
TOL	150,273	155,167	12.89
XYL	126,280	130,381	10.83
CSL	1	1	0.00
HCHO	2,000	2,063	0.17
ALD	83,549	86,253	7.17
KET	23,225	23,990	1.99
Total	1,165,681	1,203,478	

* The lumped species for NMVOCs are represented in RADM2 as: ETH (ethane); HC3 (propane, n-butane, isobutane and acetylene included); HC5 (Pentanes and hexanes included); HC8 (most n-heptane, other C_7 isomers and some C_{10} and higher isomers included); OL2 (ethene); OLT (propene and other terminal olefins); OLI (trans-2-butene, cycloalkenes and other internal olefins); ISO (isoprene); TOL (benzene, toluene and other less reactive aromatics); XYL (xylenes and more reactive aromatics); CSL (cresols and other hydroxy substituted aromatics); HCHO (formaldehyde); ALD (acetaldehyde and higher aldehydes); KET (acetone, methyl ethyl ketone and higher ketones).

Table 2.3: The total biogenic emissions (tons/yr) for the model domain

Nitrogen	Isoprene	Monoterpenes	OVOC
295,969	409,955	342,129	242,770

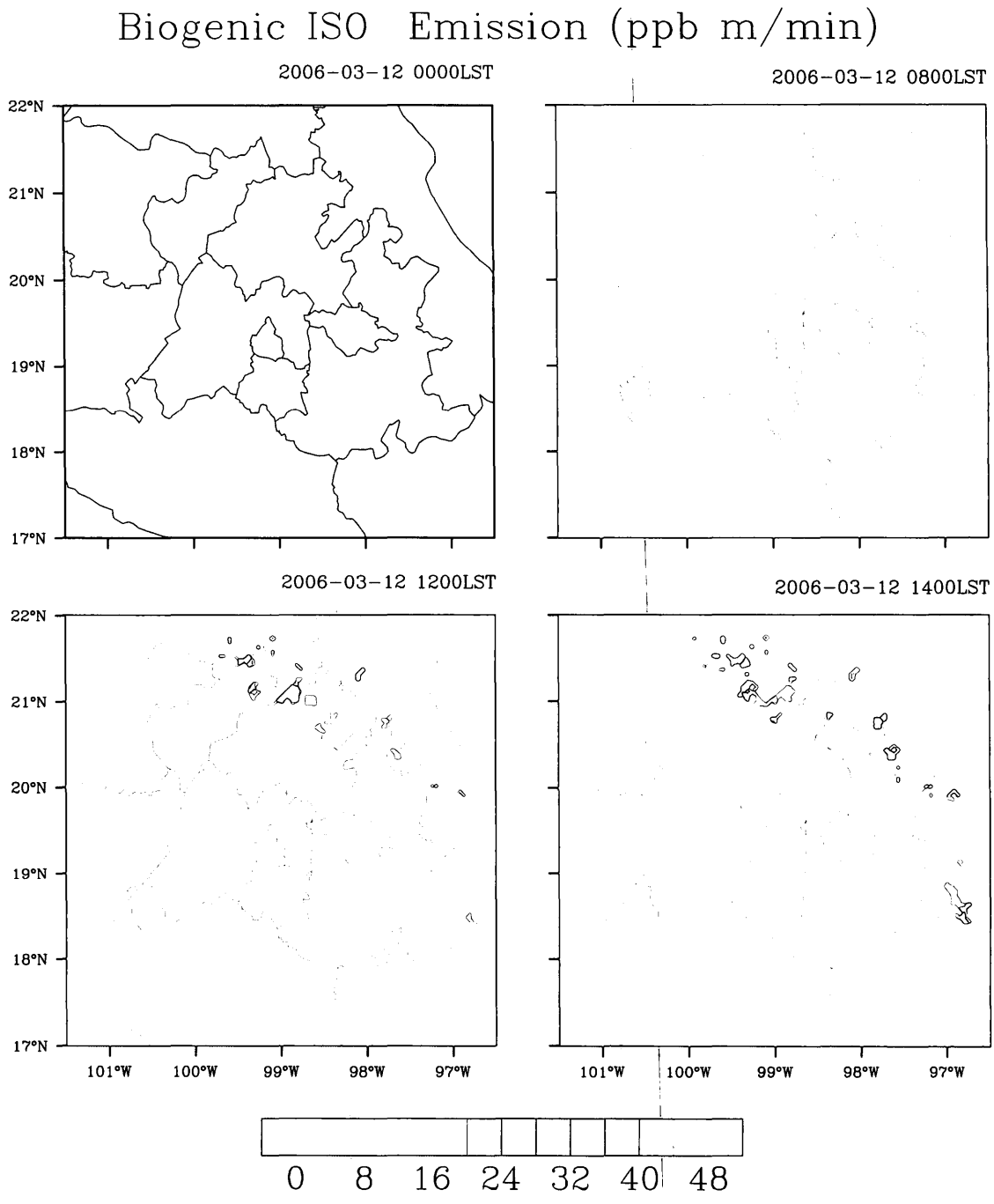

Figure 2.3: The spatial distribution of the biogenic isoprene emission rate (ppb m /min) at 0000, 0800, 1200, and 1400 LST, March 12, 2006.

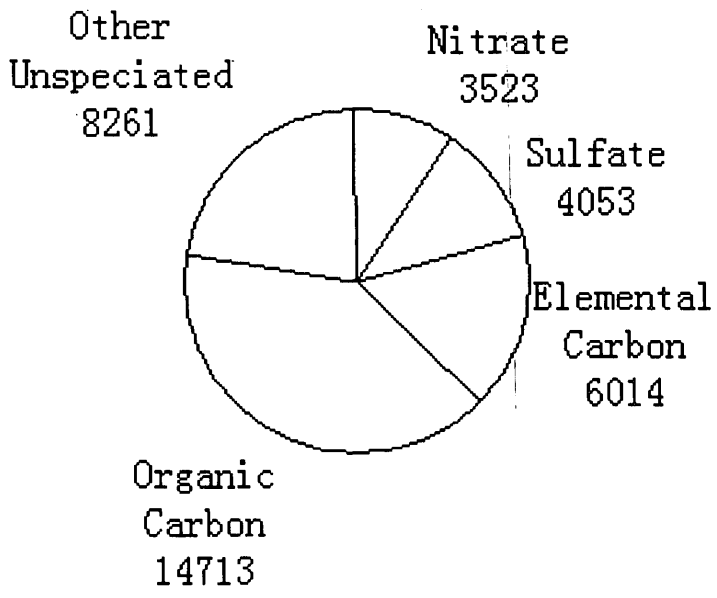

Figure 2.4: The composition of $PM_{2.5}$ particles (tons/yr) in the MC area.

and NO_2). Measurements of PM_{10} and $PM_{2.5}$ are also made routinely at RAMA sites. Meteorological measurements include ambient temperature, relative humidity, wind speed and direction. Not all stations measure all of the pollutants, in which, 15 are equipped with weather stations, 25 with CO monitors, 19 with NO_x monitors, 20 with O_3 monitors, and 16 with PM_{10} monitors. The RAMA network also includes measurements of $PM_{2.5}$ at selected 8 sites. Measurements for formaldehyde, toluene, benzene and xylene are currently made continuously at the monitoring site of La Merced (MER) (Molina and Molina, 2002).

The RAMA stations are grouped into five geographic zones: northwest (NW), northeast (NE), central (CT), southwest (SW) and southeast (SE) zones (see Fig. 5.1 in Molina and Molina, 2002). The locations of the 36 monitoring sites are shown in Fig. 2.5, with the detailed locations and measured fields given in Table 2.4. The

RAMA network does not provide any measurements outside of the Mexico City basin, and does not cover some of the rural regions within the basin.

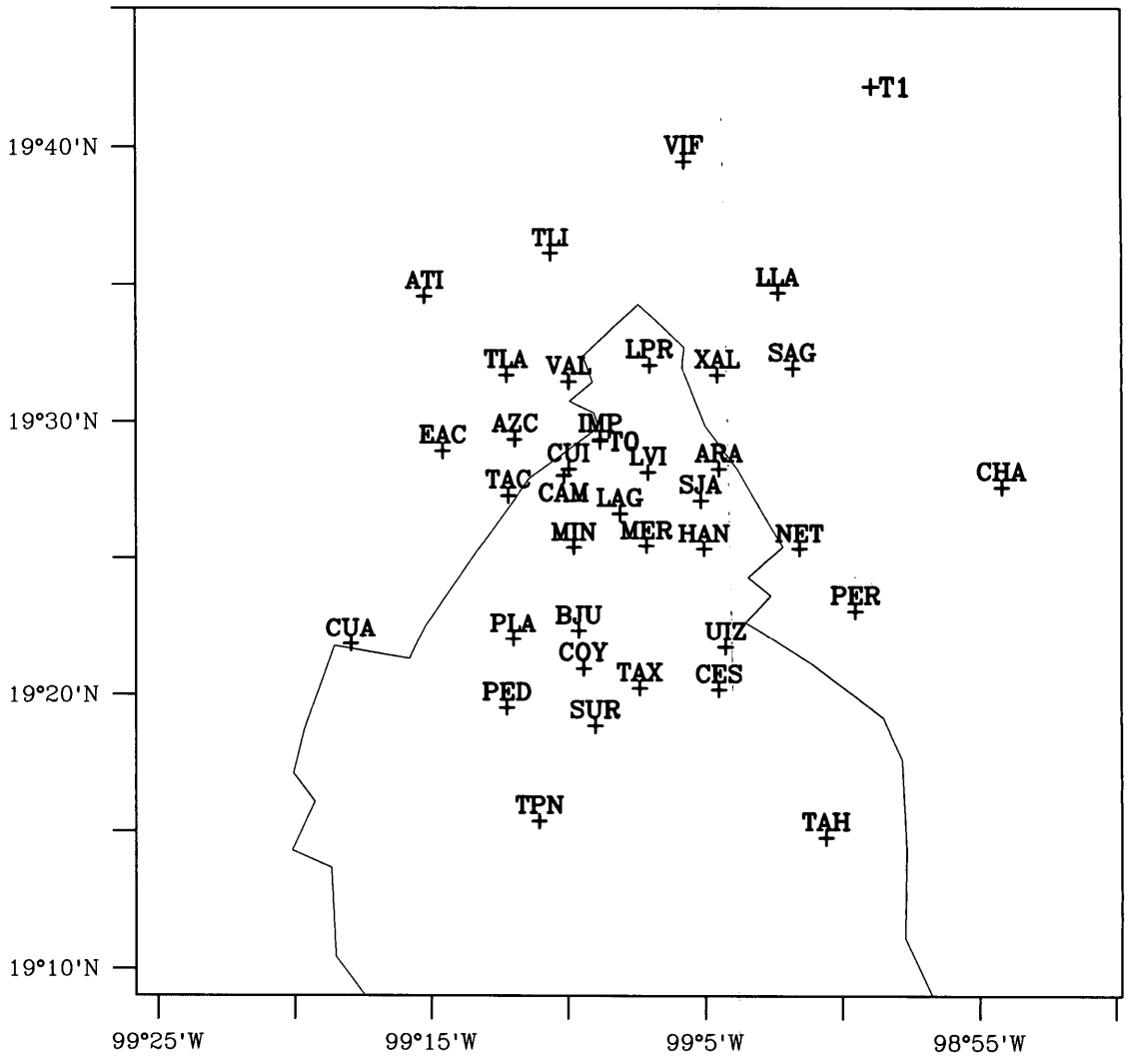

Figure 2.5: Locations of RAMA measurement sites. The red sites T0 and T1 are monitoring sites during MILAGRO field experiment.

During MILAGRO 2006 experiment, three ground supersites (T0, T1, T2), spaced about 30 km apart, were setup to characterize the chemical/physical transformations and ultimate fate of pollutants exported from urban areas (Molina *et al.*, 2010). The T0 site was located inside of Mexico City, T1 was located about 30 km

Table 2.4: Summary of RAMA measurement sites and measured fields

Site	Latitude	Longitude	T,**V**,RH	CO	NO_x	O_3	SO_2	PM_{10}	$PM_{2.5}$
ARA	19.471	-99.075		x			x		
ATI	19.576	-99.254		x	x		x		
AZC	19.489	-99.199		x	x	x	x		
BJU	19.372	-99.160		x	x	x	x		
CAM	19.467	-99.169							x
CES	19.336	-99.075	x	x	x	x	x	x	
CHA	19.460	-98.903	x			x			
COY	19.349	-99.157							x
CUA	19.364	-99.299	x			x			
CUI	19.471	-99.166		x					
EAC	19.482	-99.243	x	x	x	x	x	x	
HAN	19.422	-99.084	x	x	x	x	x	x	
IMP	19.489	-99.147		x					
LAG	19.444	-99.135		x	x	x	x		
LLA	19.578	-99.039					x		
LPR	19.534	-99.117					x		
LVI	19.469	-99.118					x	x	
MER	19.424	-99.119	x	x	x	x	x	x	x
MIN	19.423	-99.163		x					
NET	19.422	-99.026		x			x	x	
PED	19.325	-99.204	x	x	x	x	x	x	
PER	19.384	-98.992							x
PLA	19.367	-99.200	x	x	x	x	x	x	
SAG	19.532	-99.030	x	x	x	x	x	x	x
SJA	19.452	-99.086							x
SUR	19.314	-99.150		x	x	x	x	x	
TAC	19.455	-99.203	x	x	x	x	x		
TAH	19.246	-99.010	x			x	x	x	
TAX	19.337	-99.123		x	x	x	x	x	
TLA	19.528	-99.204	x	x	x	x	x	x	x
TLI	19.602	-99.177		x	x		x	x	
TPN	19.256	-99.184	x			x			
UIZ	19.362	-99.071		x	x	x	x		x
VAL	19.524	-99.166		x			x		
VIF	19.658	-99.096	x	x	x		x	x	
XAL	19.528	-99.076	x	x	x	x	x	x	
Total = 36			15	25	19	20	26	16	8

northeast of T0 (see Fig. 2.5 for the locations), and T2 (not shown in Fig. 2.5) was located another 30 km north of T1. The designations of "T0", "T1", and "T2" refer to the timing of transport of the urban plume to different points in space and time.

2.6 Numerical simulations

Three set of numerical simulations were performed in this study: (1) Chemical species were simulated and compared with the measurements. Several sensitivity simulations were conducted to calculate the response of O_3 concentrations to changes in surface emissions of NO_x and VOCs; (2) The impact of diurnal variations of surface emissions on O_3 and O_3 precursors was simulated; and (3) Dust aerosol and its effect on photochemistry were simulated.

Chapter 3

Simulation of Air Pollutants in the Mexico City Area

In this chapter, model simulations using the WRF/Chem model (version 2.2) for the meteorological conditions and chemical species, and the O_3-NO_x-VOC sensitivity in the MC area are presented. Section 3.1 briefly describes the meteorological conditions and simulations during March 12 -15, 2006. In section 3.2, simulations of chemical species are compared with the measured values, and the diurnal variations of CO, NO, NO_2, O_3, and O_X are then discussed. The sensitivity of O_3 to NO_X and VOCs is presented in section 3.3; and the OH reactivity with VOCs is discussed in section 3.4.

3.1 Meteorological conditions and simulations

Dry air, clear skies, and weak winds are usually observed over Mexico during March. Typically, the synoptic flow is dominated by anti-cyclone circulations over central southern Mexico and the Gulf of Mexico, and westerly flows aloft north of 20° N (de Foy *al.*, 2005, Fast *al.*, 2007). This synoptic-scale condition leads to subsidence over

the Mexico Basin with weak surface winds which are favorable to the development of thermally driven circulations.

The model simulations were based on the period between March 12 and 15, 2006, during which, the MC region is under clear sky conditions. On March 12, an upper-level trough, propagating and developing over the western US, and moved over north-central US on March 13. Between March 14 and 15, a series of troughs and ridges propagated from west to east across the US, and affected the position of the high pressure system over the Gulf of Mexico and led to variable wind directions over central Mexico (see Fig. 3.1 for 700 hPa geopotential height and wind fields).

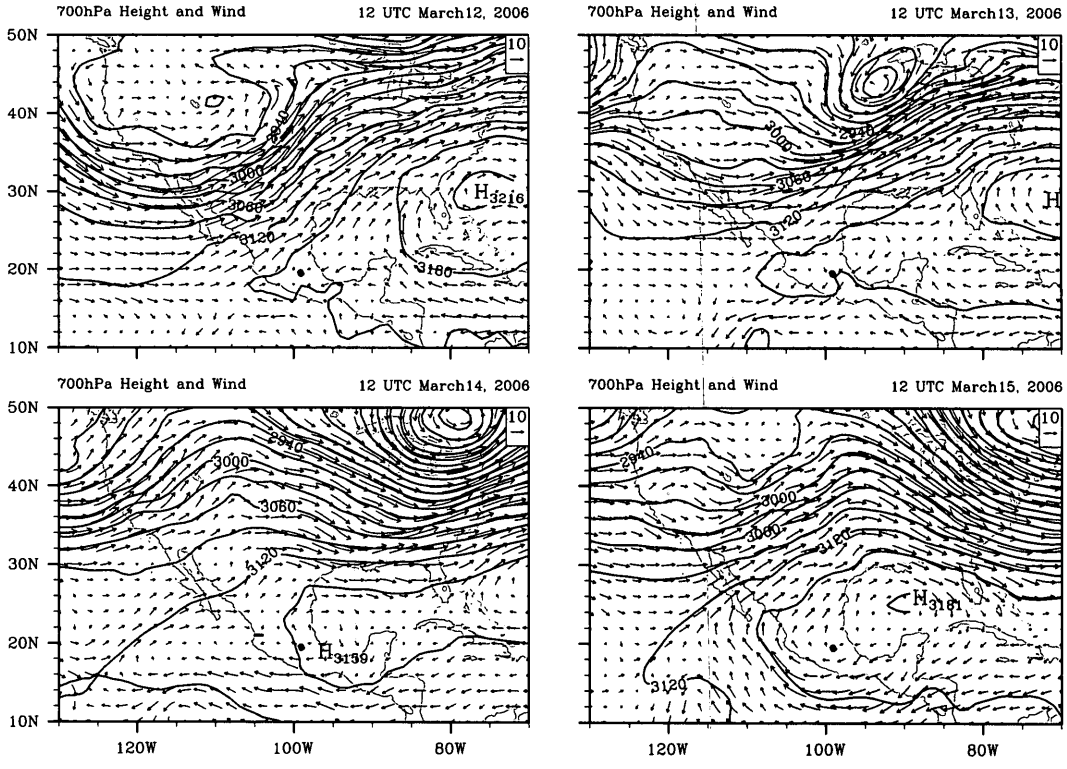

Figure 3.1: Weather map on 700 hPa at 12:00 UTC March 12 - 15, 2006. Data is from NCEP global Final (FNL) analysis.

The sea-level pressure and surface wind (10 m) fields at 12:00 UTC during March 12 - 15, 2006 are shown in Fig. 3.2. During March 12 and 13, a high pressure

system is located over the Gulf of Mexico while low pressure systems are situated over the central US. Strong sea breezes develop under these conditions, bringing warm moist air from the Gulf. With the low pressure system moving to eastern US, a high pressure system over Texas with convergence aloft, leads to strong northerly near-surface flow of cold air down to the Gulf of Mexico (called "Cold Surge") on March 14 and 15. The types of weather on these days are conducive to ozone production. Mostly sunny skies occurred over central Mexico during March 12-13; and between March 14-15, clear skies were mostly observed during the morning and partly to mostly cloudy skies with an increase in low-level clouds during the afternoon (Fast *et al.*, 2007).

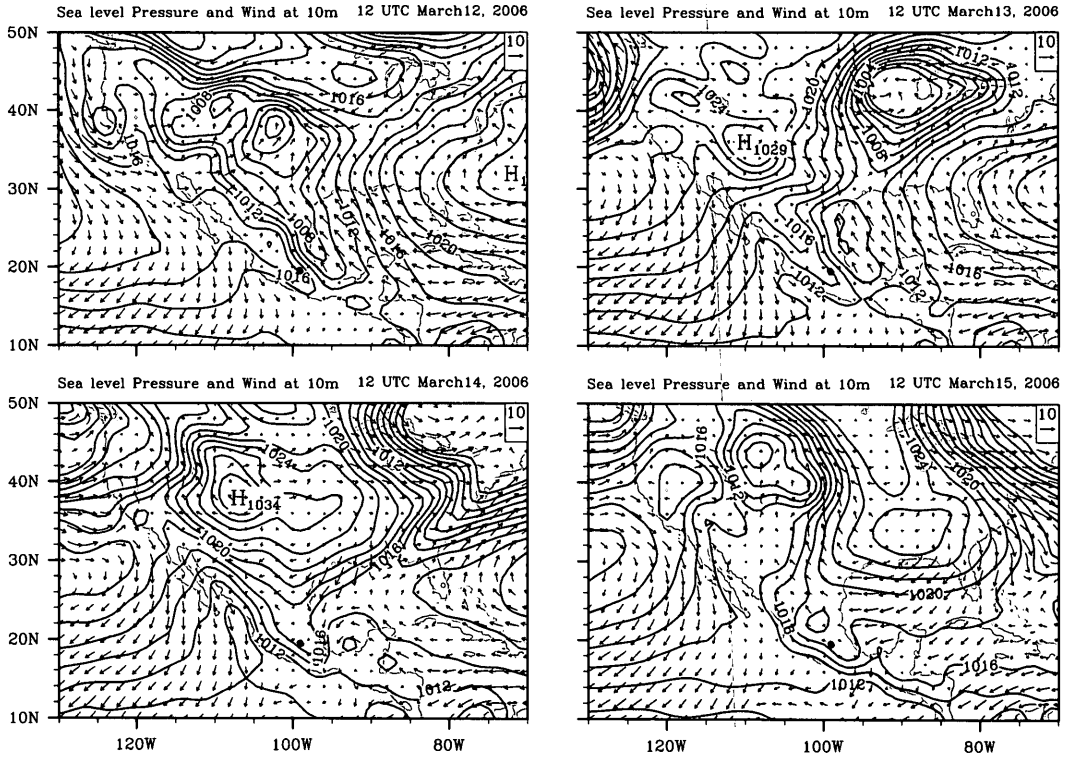

Figure 3.2: Weather maps on the surface at 12:00 UTC March 12 - 15, 2006. Data is from NCEP global Final (FNL) analysis.

Figure 3.3 shows the simulated and measured surface temperature, relative humidity, wind speed and direction at the measurement sites of MER (city site) and SAG (northern suburb site) during March 12 - 15, 2006. The measurements and simulations all show that warm, dry and weak winds occurred on March 12 and 13, while cooler air with increased humidity, and relatively windy with predominant northerly winds occurred during March 14 and 15. Comparing with the measurements, we found that the timing of the diurnal cycle and the minimum nighttime temperature are fairly well represented. However the surface temperature maxima were underestimated in the *urban area* (MER), but were well estimated in the *suburb area* (SAG). The urban expansion in the Mexico City area, which is not well represented in USGS data, could be one reason to explain the model underestimation of the surface temperature maxima in the site of MER. The simulated relative humidity, wind speed, and wind direction were very similar to those from measurements on March 14 and 15, but relatively large differences occurred on March 12 and 13.

There are several features regarding the simulated surface winds in the Mexico City basin (Fig. 3.4 and Fig. 3.5): (1) Strong mountain breezes are evident during this period, there are up-slope winds in daytime and down-slope during the night, especially on the southwest side; (2) For wind speed, winds are weak in the early morning, increase steadily from sunrise to sunset and then decrease until about midnight; (3) The gap winds in the south-southeast gap are found to occur from day to day. In general, there are strong southerly winds in the afternoon.

The basin circulation is a combination of synoptic flows and thermally-induced mountain breezes. On March 12 and 13, the southerly wind was combined with the mountain breeze in the basin area, and as a result, southeasterly winds prevailed in late afternoon and nighttime. This turned into cyclonic conditions with weak surface winds during daytime, which prevented transport of air pollutants. The whole basin was influenced by northerly winds during March 14 and 15. After mid-afternoon

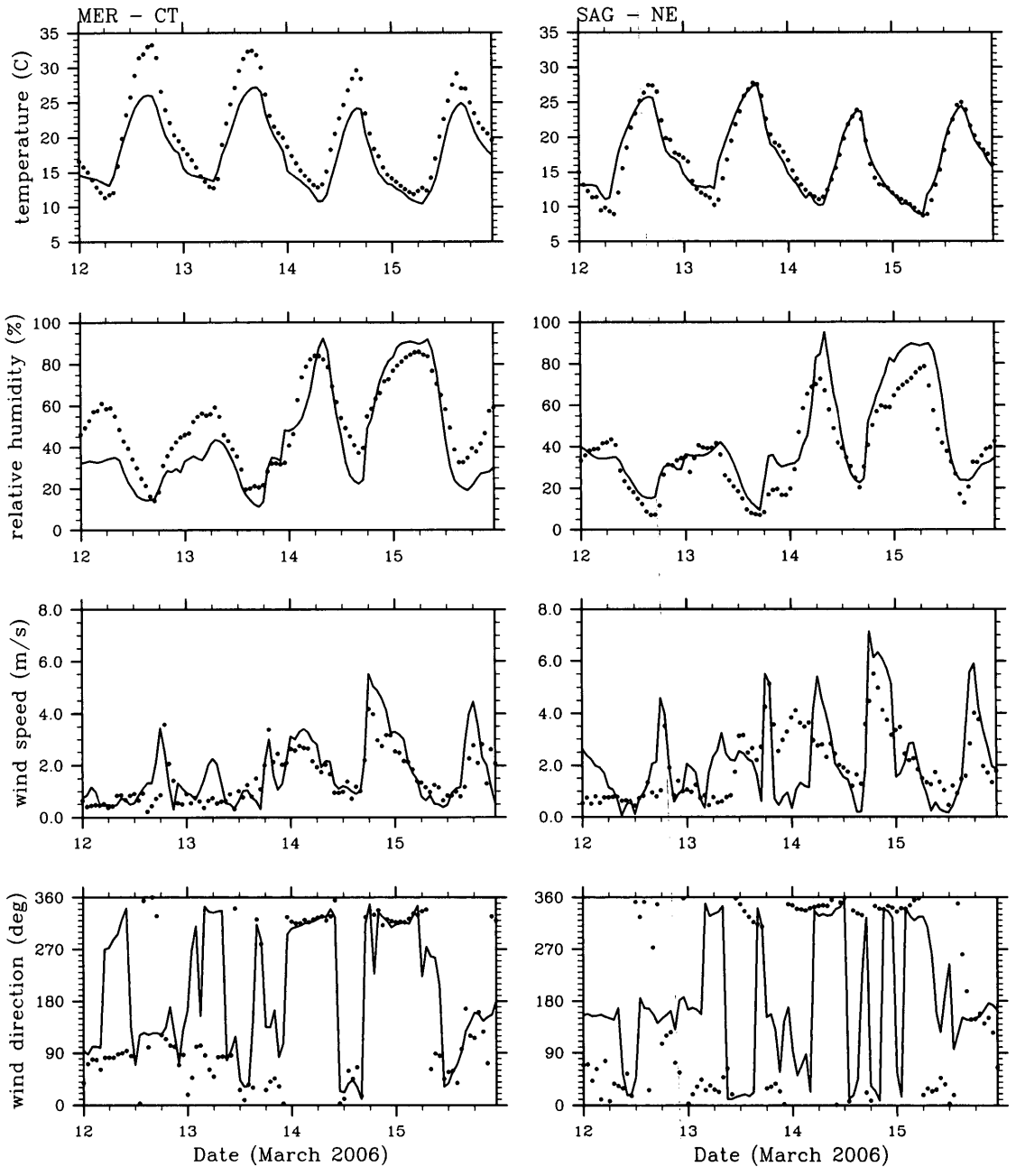

Figure 3.3: Comparison of the simulated and measured temperature, relative humidity, wind speed and direction at sites of MER (left) and SAG (right) for the 4-day period from March 12–15, 2006. Black dots represent the measurements and solid lines represent the simulations.

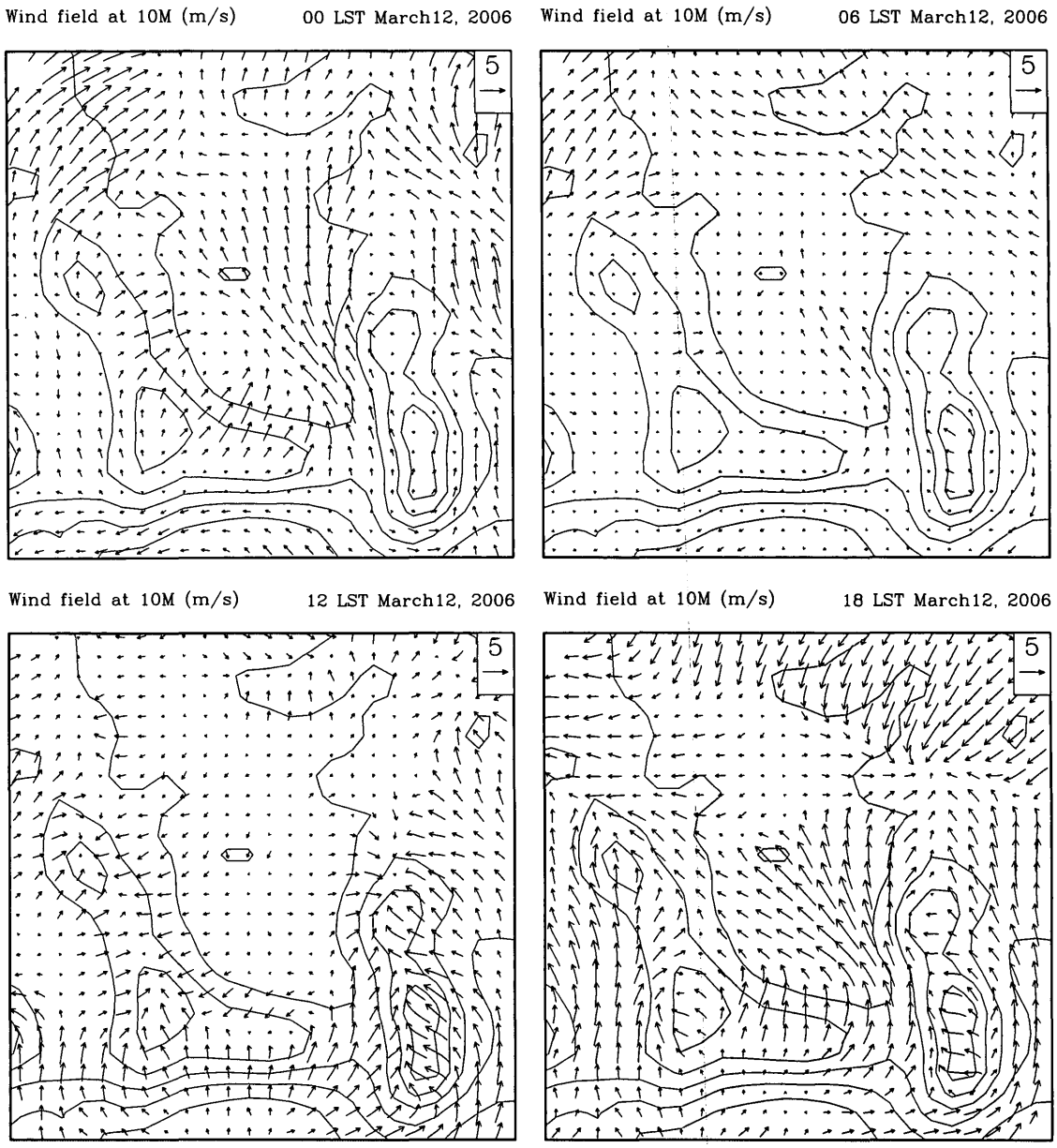

Figure 3.4: Simulated surface winds (10 m) at 0 AM, 6 AM, 12 PM and 18 PM on March 12, 2006. The contour lines are the terrain height around the MC area, with contours (km) from 1 to 4 by 0.5.

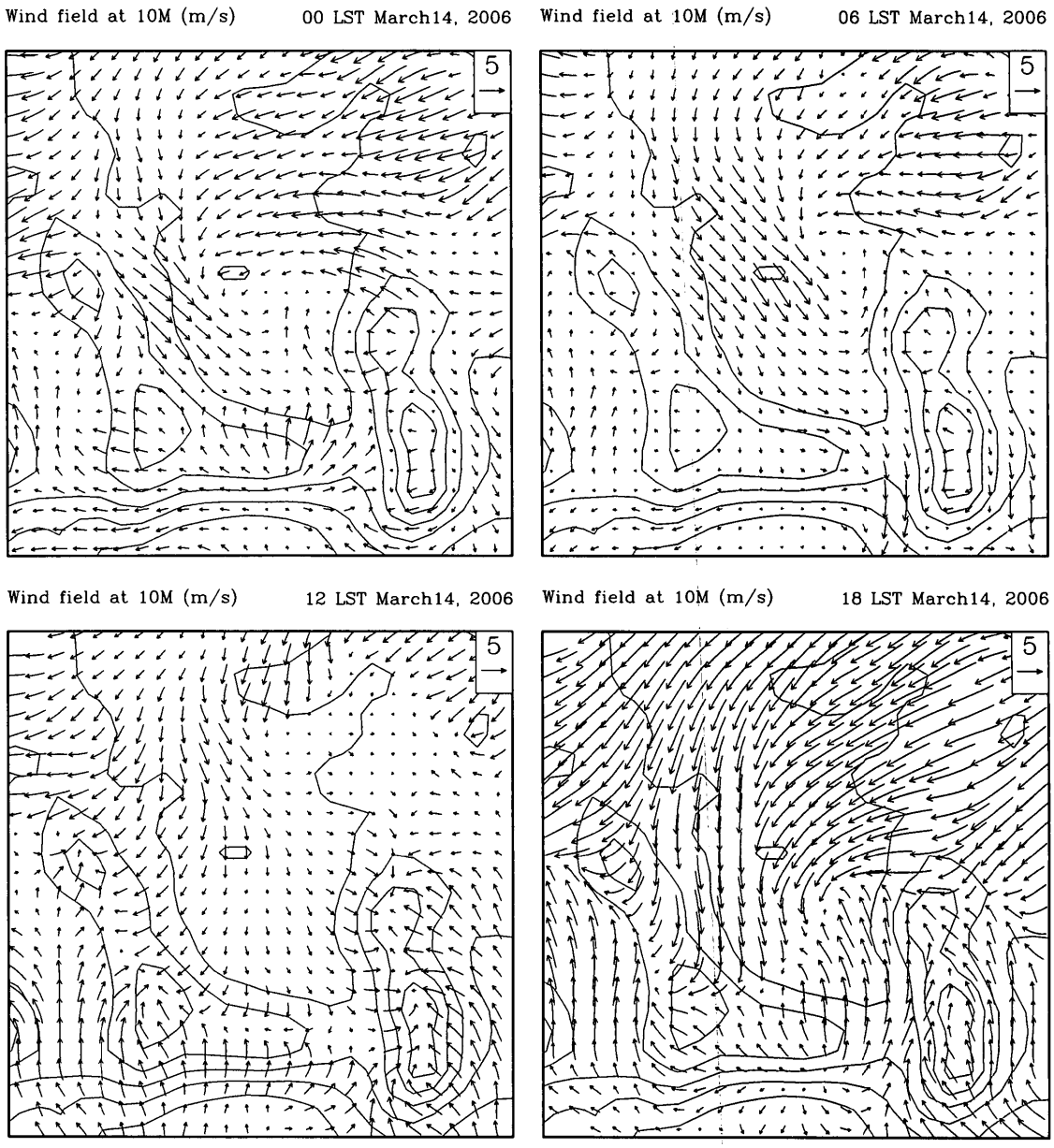

Figure 3.5: Simulated surface winds (10 m) at 0 AM, 6 AM, 12 PM and 18 PM on March 14, 2006. The contour lines are the same as that in Fig 3.4.

(around 3 PM), the easterly winds strengthened and changed to northerly synoptic flow while the southerly gap winds lead to a convergence in the city during the evening and the early morning.

3.2 Simulations of chemical species

To compare the simulated with the measured diurnal cycles of CO, NO, NO_2 and O_3, the model results and the measurements are averaged over all RAMA sites during the four-day period from March 12 to 15, 2006. The model simulations at the lowest model level (about 40 m above the surface) were interpolated to the RAMA sites by 4-points bilinear interpolation, and compared with the near-surface RAMA measurements. Figure 3.6 shows the averaged concentrations of the simulated and measured CO, NO, NO_2 and O_3. The black dots represent the measurements and the solid lines represent the simulations. The magnitudes and timings of the model simulated diurnal cycles of these chemical species are generally in agreement with the measured diurnal variations, especially for O_3. However, there are also discrepancies between the simulations and the measurements. For example, the simulated morning maxima of CO, NO, NO_2 are underestimated on March 13, while overestimated during other days, suggesting that the estimated emissions of CO and NO_x, and the meteorological conditions on March 13 may not be properly represented in the model. The standard deviations (used to show how much variation from the averaged values over the RAMA sites) for the simulated and measured CO, NO, NO_2 and O_3 concentrations are shown in Fig. 3.7. The maxima for the averaged concentrations of the measured O_3 are 122, 87, 122, and 116 ppb during March 12-15, 2006, and the maxima of their standard deviations are 15, 23, 43, and 34 ppb; The maxima for the averaged concentrations of the simulated O_3 are 127, 79, 127, and 125 ppb, and

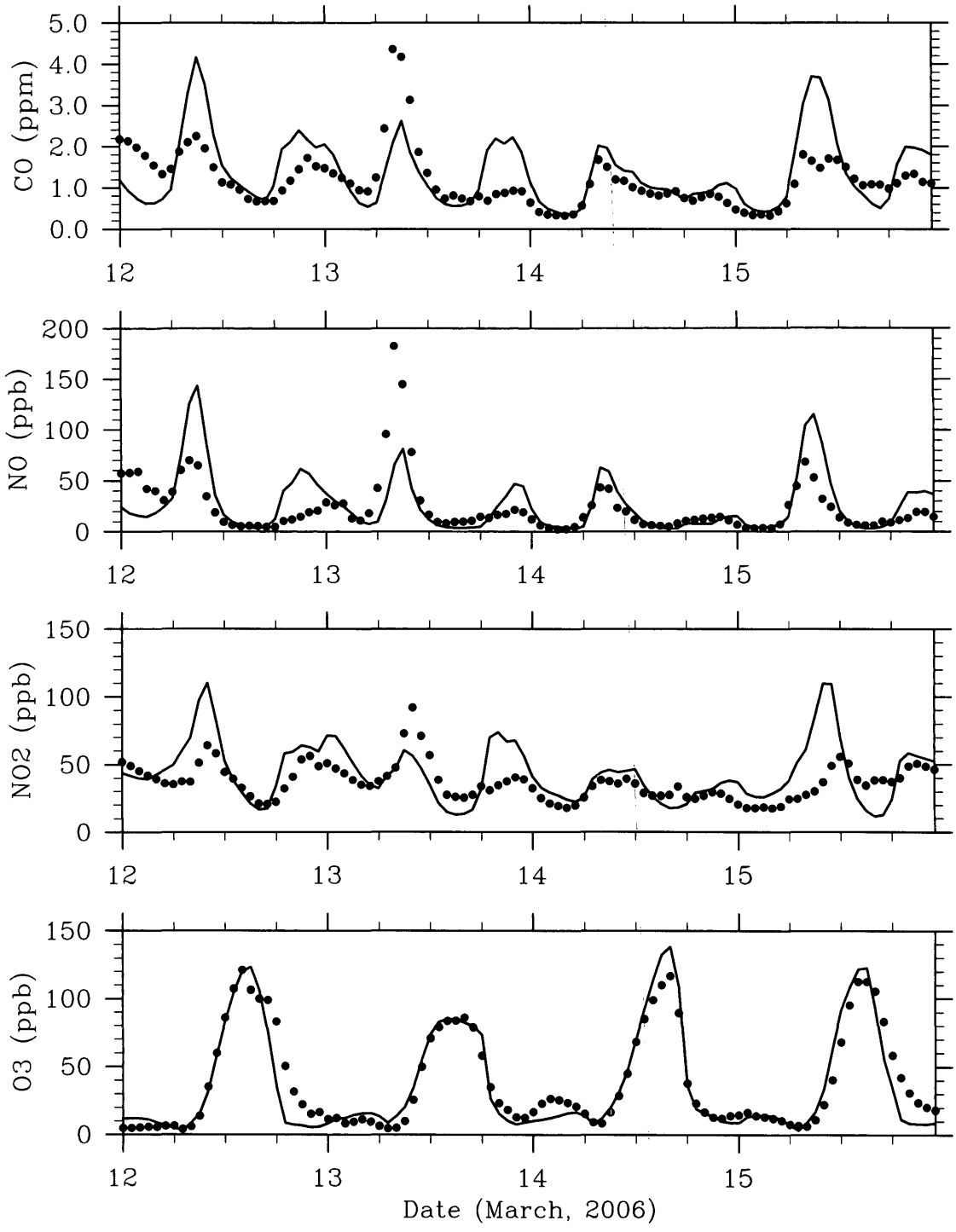

Figure 3.6: Comparison of the simulated and measured concentrations of CO, NO, NO_2 and O_3 averaged over all RAMA sites which have measurements, from March 12–15, 2006. Black dots represent the measurements and light solid lines represent the simulations.

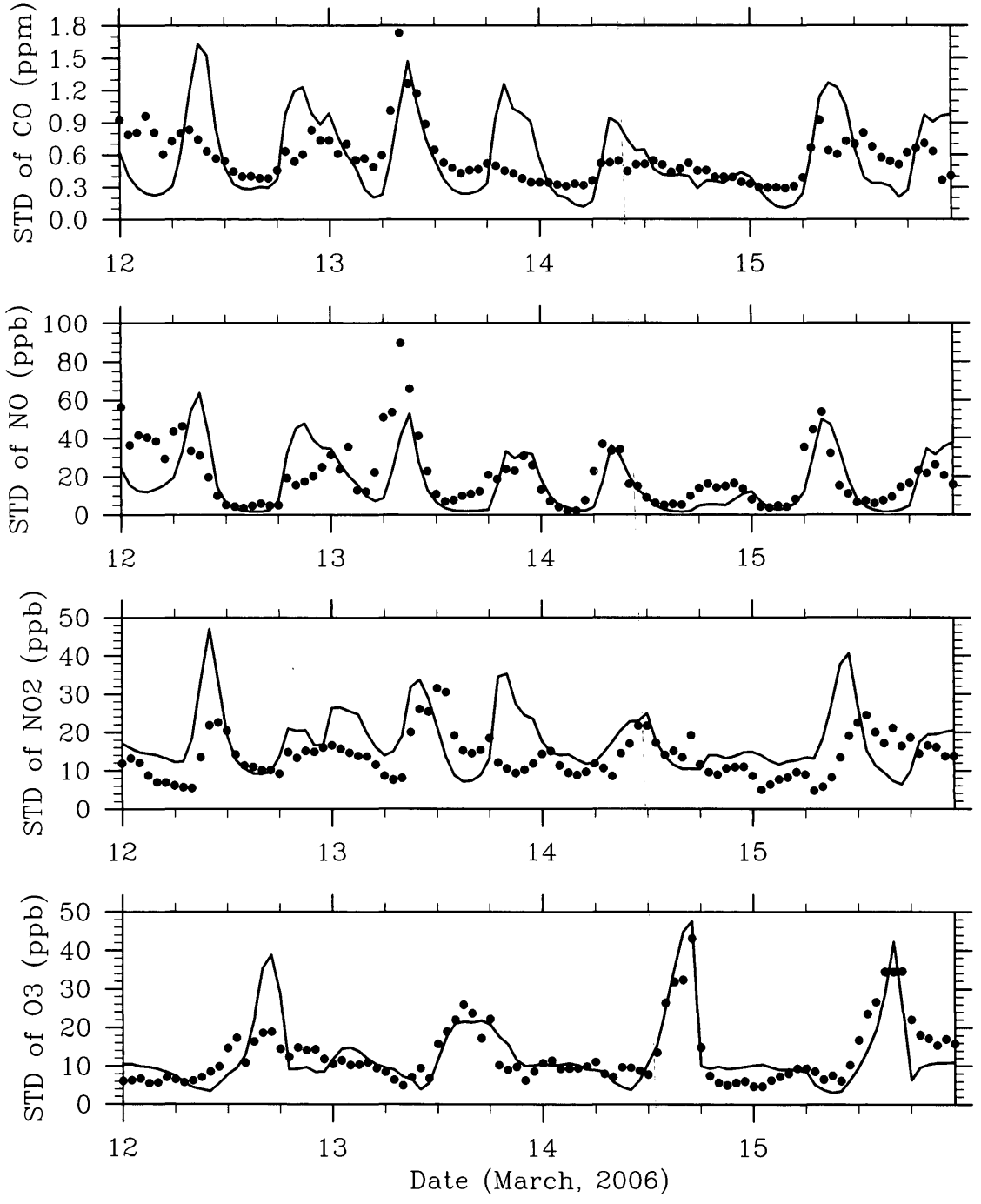

Figure 3.7: The standard deviations of the simulated and measured concentrations of CO, NO, NO_2 and O_3 during the period of March 12–15, 2006. Black dots represent the measurements and light solid lines represent the simulations.

the maxima of their standard deviations are 38, 21, 47, and 42 ppb. The standard deviations are about 20-30% of their averages.

The model simulations are also examined for individual measurement sites. In Fig. 3.8, 3.9 and 3.10, we compare the simulated surface CO, NO_x and O_3 concentrations with the measurements at selected 10 sites (2 sites in each geophysical zone, see Fig. 2.5 and Table 2.4 for site information) in the MC area. The detailed analysis suggests that: (1) The simulated concentrations of CO and NO_x in the northeastern zones are underestimated during the entire period despite of the different directions of the surface winds, suggesting that emission rates may be underestimated in the northeastern regions. (2) In March 13, the morning peaks of CO and NO_x are underestimated almost at all sites, especially in the northern sites. (3) The model overestimates of CO, and NO_x in March 12 and 15 appeared mainly at the sites in the central and southern zones. Figure 3.11 shows the simulated and measured distribution of O_3 concentrations at 3 PM, March 12, 2006; The simulated maxima of O_3 were in good agreement with the RAMA measurements, although they are overestimated in the northeastern area and underestimated in the southeastern area.

Despite these discrepancies, the model is capable of capturing many details of the diurnal variations of CO, NO, NO_2 and VOCs at all sites (see Fig. 3.12). For example, the near surface O_3 concentrations of the simulations and the measurements all show the minima in the early morning (around 7 AM) and the maxima in the afternoon (around 3 PM). In contrast to O_3, the concentrations of CO, NO and NO_2 all exhibit two peaks with the highest peak in the early morning and the second peak in the evening, although both peaks were overestimated. The timing of NO_2 was well simulated; but the simulated morning peaks of CO and NO all appeared 1 hour later than the measurements.

As discussed in Tie *et al.* (2007), the diurnal variations of PBL height have important effects on the diurnal variations of air pollutants that are emitted directly

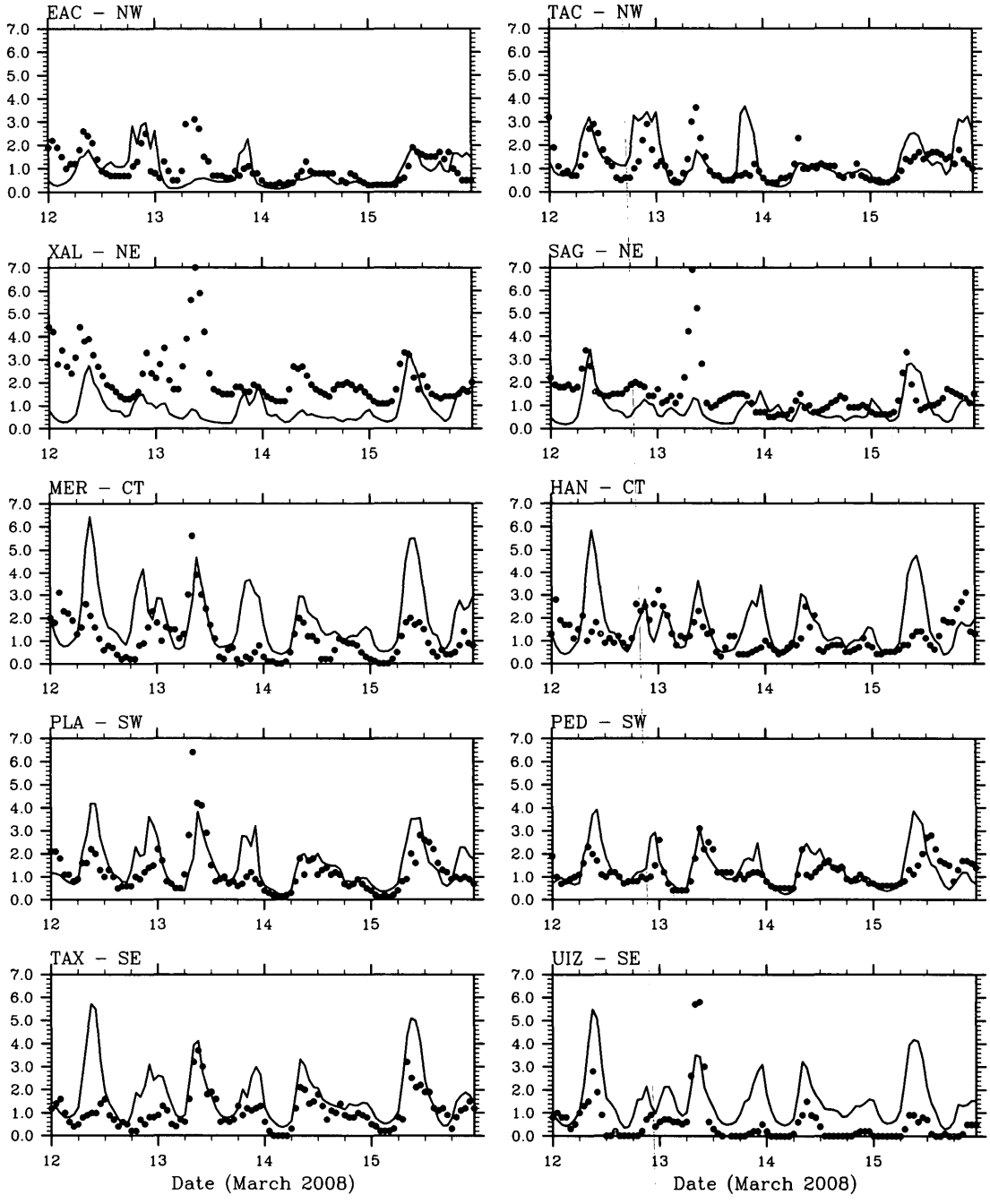

Figure 3.8: Comparison of the simulated and measured concentrations of *CO* (ppmv) at selected sites, for the 4-day period from March 12–15, 2006. Black dots represent the measurements and light solid lines represent the simulations.

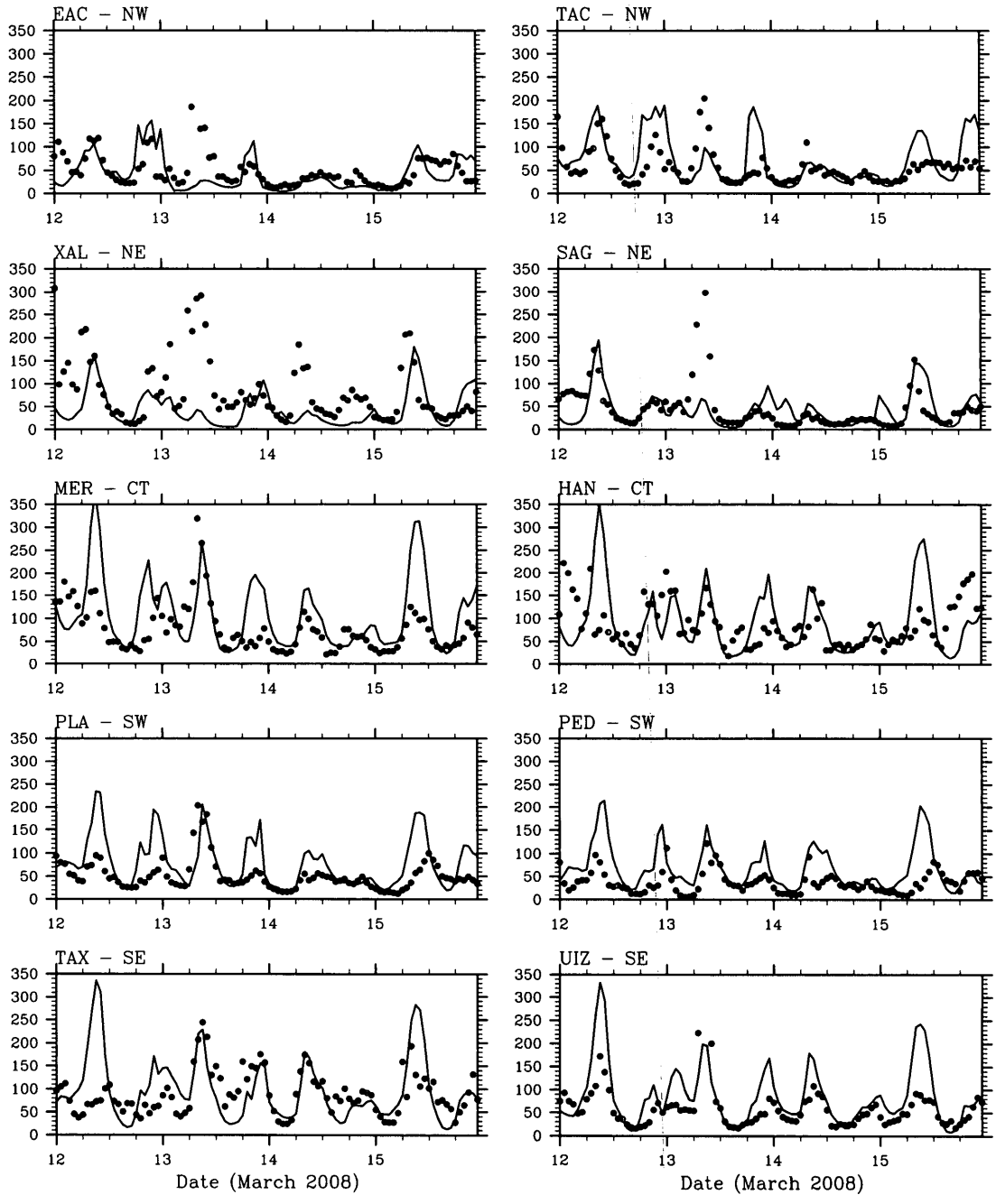

Figure 3.9: Comparison of the simulated and measured concentrations of NO_x (ppbv) at selected sites, for the 4-day period from March 12–15, 2006. Black dots represent the measurements and light solid lines represent the simulations.

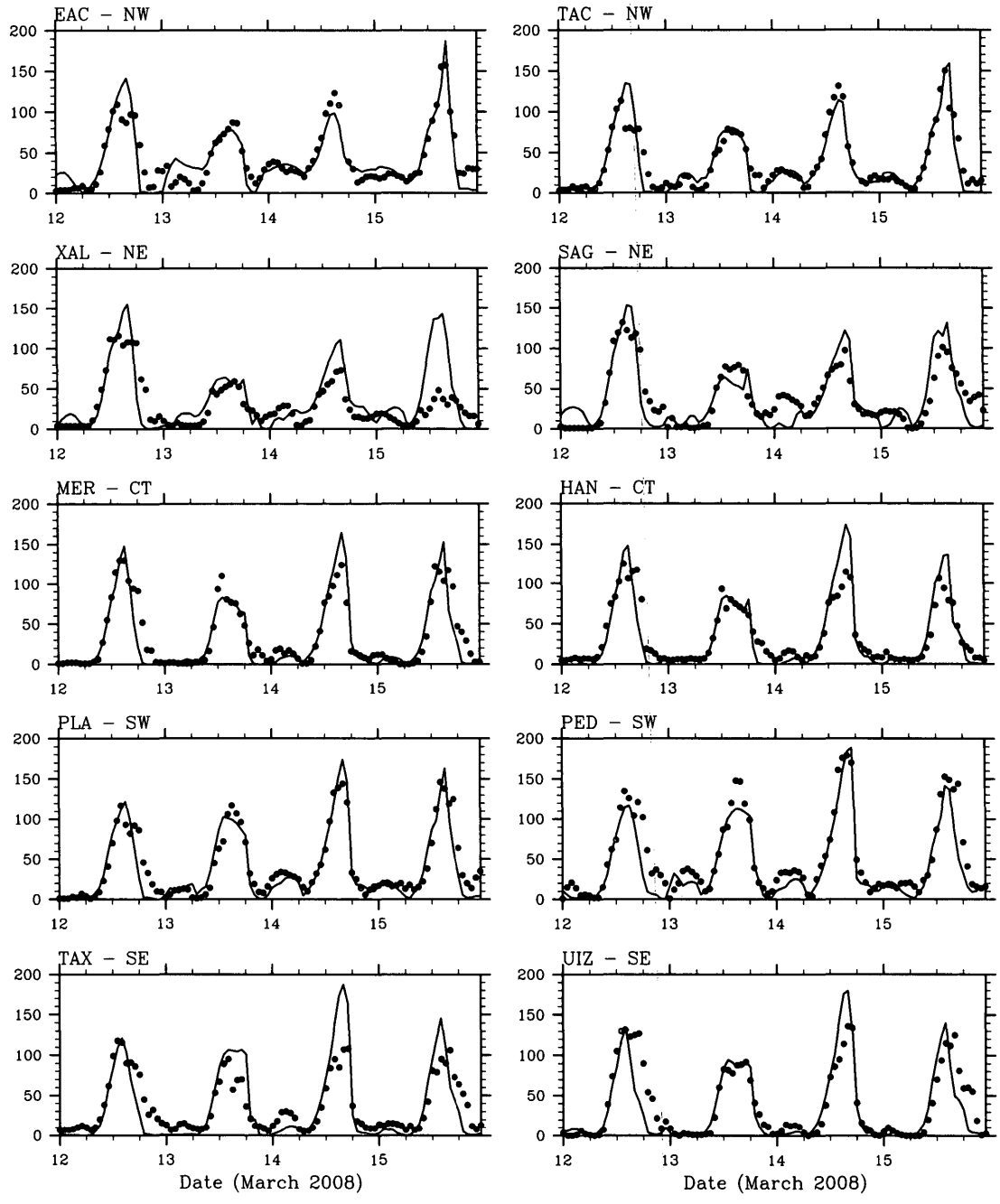

Figure 3.10: Comparison of the simulated and measured concentrations of O_3 (ppbv) at selected sites, for the 4-day period from March 12–15, 2006. Black dots represent the measurements and light solid lines represent the simulations.

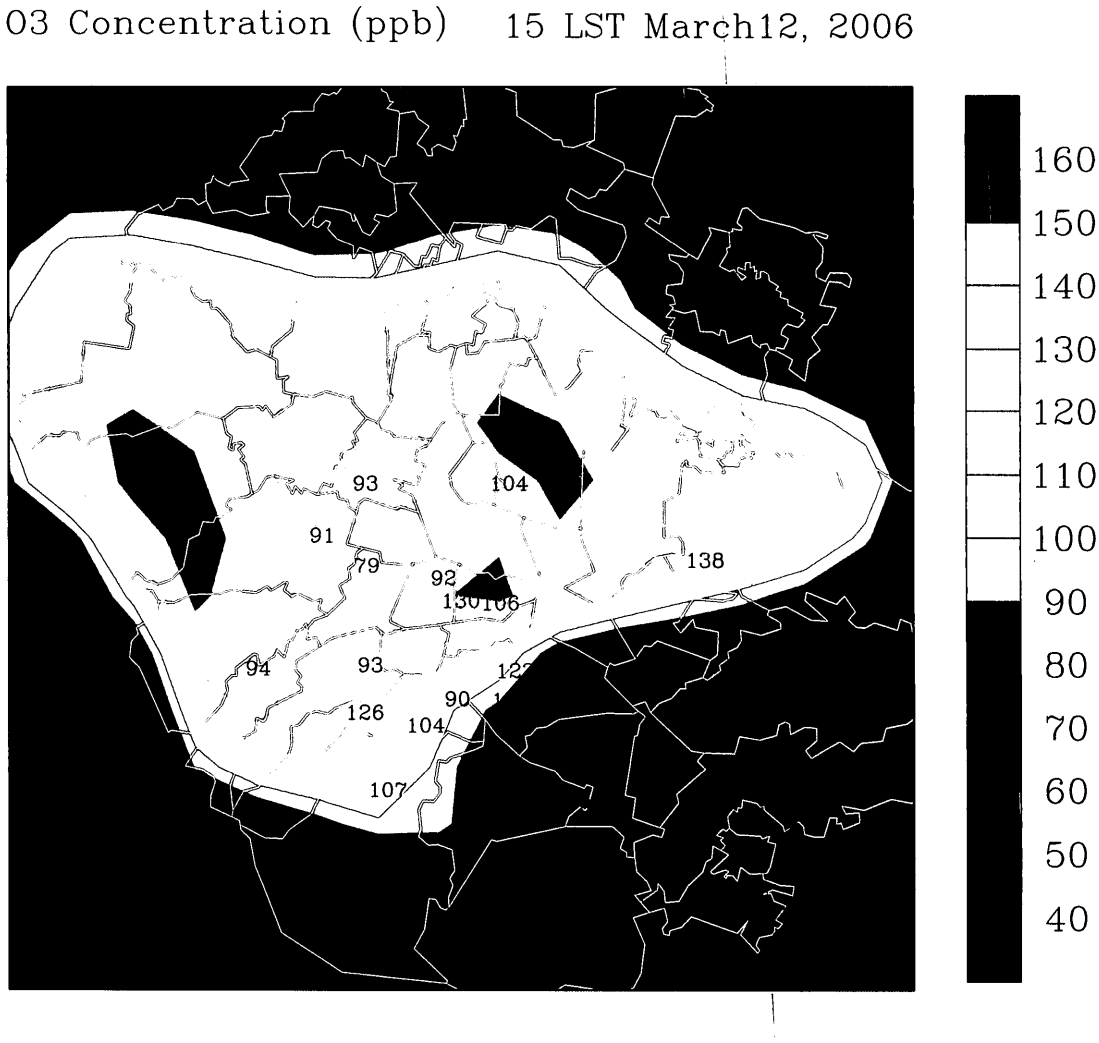

Figure 3.11: Comparison of Simulated (colored contour) and measured (black number values) near-surface O_3 concentrations (ppbv) in MC area at 3 PM, March 12, 2006.

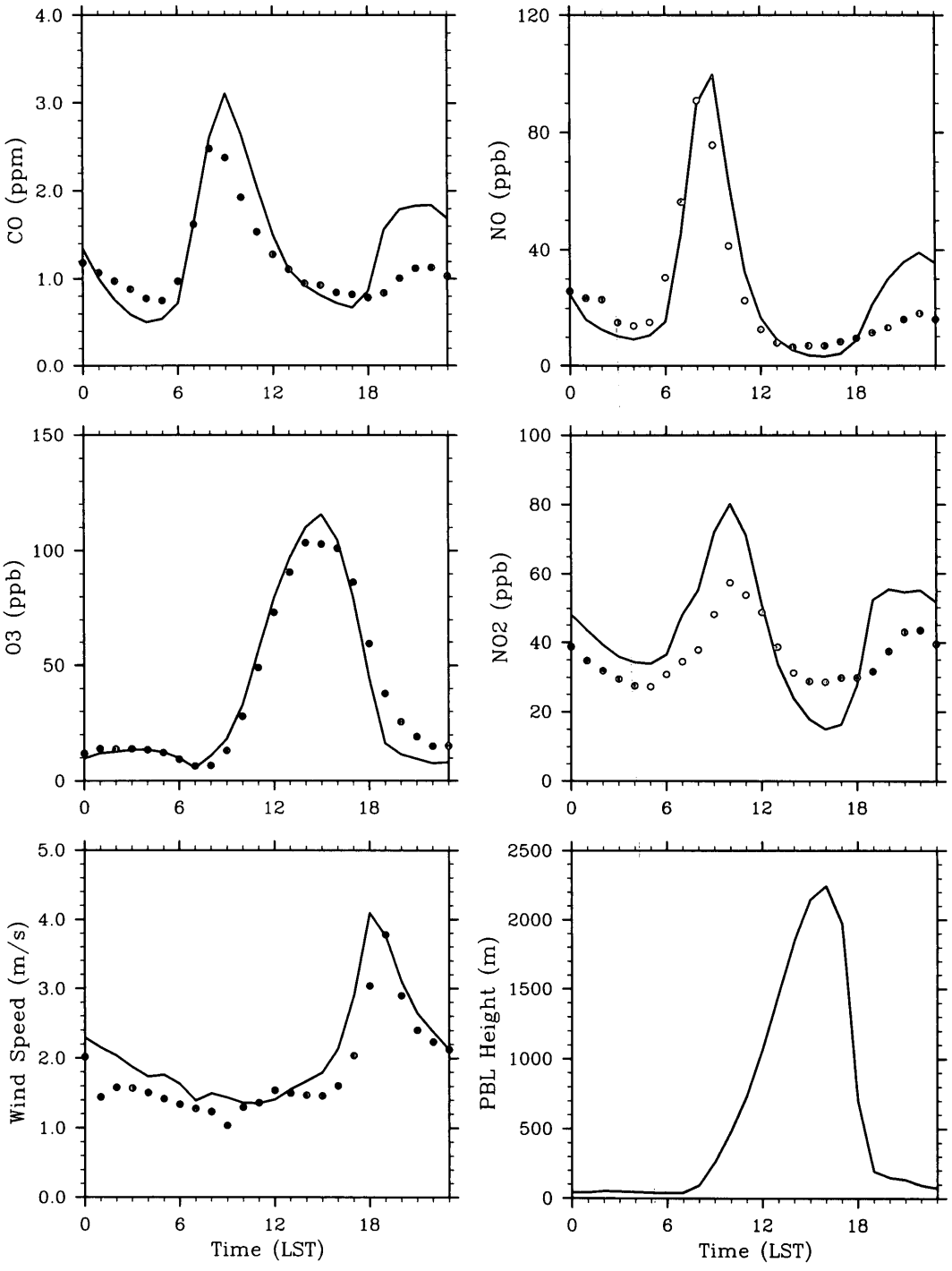

Figure 3.12: The diurnal cycles of measured and simulated CO, NO, NO_2 and O_3 concentrations, wind speed and PBL height, averaged over all RAMA measured sites which have measurements and 4-day period during March 12–15, 2006. Black dots represent the measurements and light solid lines represent the simulations.

from the surface, such as CO, NO and VOCs. The concentrations of CO and NO increased in the morning and reached their maxima around 9 AM before the mixing layer started to grow. As the daytime PBL deepens, the concentrations drop and reach a minimum around 4 PM when the PBL height reaches the maximum (see PBL height in Fig. 3.12). Since the PBL height is shrinks rapidly in the evening, their concentrations rise again with continued emissions, and reach the second maxima around 10 PM at night. Furthermore their concentrations are also affected by winds. Winds are usually calm in the early morning with minimal horizontal dispersion, wind speeds reached a maximum by sunset (around 6 PM) leading to substantial dilution of pollutants (see Fig. 3.12 for wind speed) and transport air pollutants away from urban area and out of the valley.

Emission of NO_2 is $\sim$ 10% of NO, and it is generated by oxidation of NO. So the distribution of NO_2 is determined by emission, transport and photochemistry processes. NO_2 has a strong diurnal variation which related to solar radiation, NO and O_3 concentrations. During the morning, with higher chemical production which related to NO and VOCs, NO_2 follows NO rise and reaches the maximum peak around 10 AM, Consequently NO_2 decreases significantly due to more O_3 to titrate, and reaches the minimum (about 20 ppbv) around 4 PM when transport is strong. NO is depleted and NO_2 is present at night due to O_3 titration reaction (R1.1).

Ozone is mainly produced by photochemical reactions involving NO_x and various reactive VOCs during daytime. The distribution of O_3 depends mainly on the photochemical production, and there are relatively large diurnal variations of O_3. Surface O_3 concentration rises in the morning after the sunlight is enhanced, with the precursors (NO_x and VOCs) built up in the morning rush hours. It reaches a maximum around 3 PM, then decreases. During nighttime, chemical O_3 production ceases and O_3 loss happens by reaction with NO to form NO_2, the concentration of

O_3 approaches a minimum around 7 AM, when more NO reacted with O_3 while the sunlight is still weak.

In addition to O_3, a quasi-conservative quantity, Oxidant ($O_X = O_3 + NO_2$) (Kley *et al.*, 1994) is used to represent the total O_3 level as regional and local contribution (see Fig. 3.13). The reduction of O_3 level due to NO titration effects can be accounted for by regarding difference between O_X and O_3. Due to the photochemical formation of O_X, the concentration of O_X increases quickly after 6 AM, and arrives a higher value around 11 AM when NO, NO_2 and O_3 are under photostationary state. After 3 PM, with reduced photochemical production, concentration of O_X decreases quickly until at 6 PM. During nighttime, photochemical O_X production ceases, and O_3 is the major oxidant for NO. The O_3 level is reduced due to NO titration reaction, while O_X keeps a steady higher values, and mostly is in the form of NO_2.

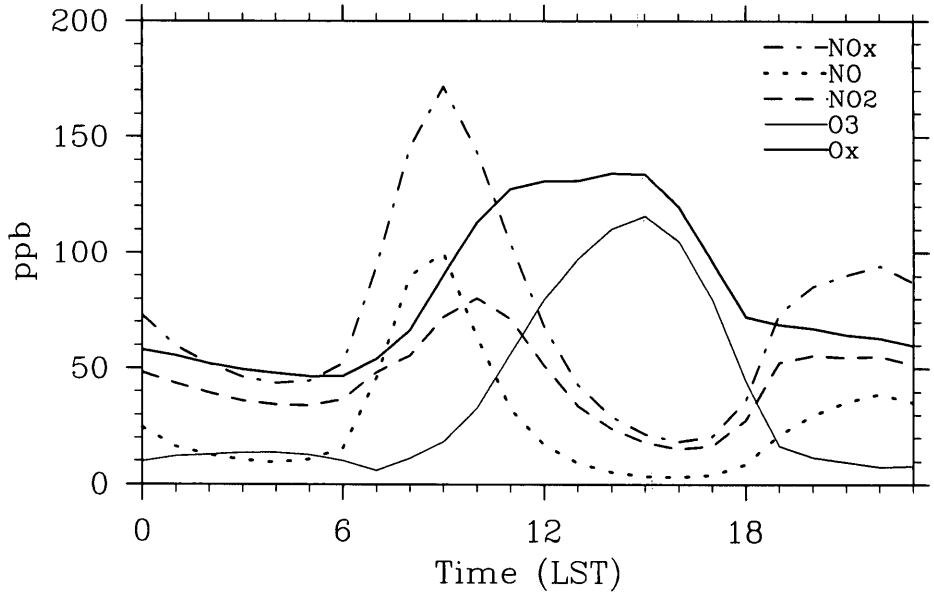

Figure 3.13: The averaged diurnal cycles of simulated concentrations of NO_x, NO, NO_2, O_3, and O_X.

3.3 Ozone-NO_x-VOC sensitivity

The daytime O_3 chemical formation in Mexico City appeared to be NO_x sensitive in the late 90s (Molina and Molina, 2002). However, more recent studies found that it is strongly VOC-limited (Tie *et al.*, 2007, Lei *et al.*, 2007, Nunnermacker *et al.*, 2008) and NO_x-inhibited (Stephens *et al.*, 2010). To better understand the O_3 formation in the Mexico City area, and the relationship between O_3 concentrations and emissions of NO_x and VOCs, several sensitivity simulations were conducted to calculate the response of O_3 concentrations to changes in NO_x and VOC emissions. In these simulations, only NO_x or only VOC emissions were increased or decreased by 50%, equally at all locations, while keeping other emissions unchanged. A total 4 simulations were completed.

Figure 3.14 shows the sensitivity of surface O_3 concentrations to emissions of NO_x and VOCs, averaged over all RAMA measurement sites and the 4 day period during March 12–15, 2006. The concentrations of NO_x and VOCs are dependent on their emissions, higher emissions result in higher concentrations, and lower emissions result in lower concentrations (Fig. 3.14a and Fig. 3.14d). Increase in VOC emissions leads to an significant O_3 increase in daytime (green dashed line in Fig. 3.14d), and decrease in VOC emissions leads to daytime O_3 greatly decrease (brown dotted line in Fig. 3.14e). The relative enhancements are about 25% and -40% for O_3 maxima, and 31% and -40% for 8-hour average O_3, respectively. Here the change of O_X concentrations (Fig. 3.14f) are consistent with that of O_3, both O_3 and O_X are increased with increased VOC emissions, which are related to the enhanced photochemical O_3 formation.

However increasing NO_x emissions leads to large reduction in daytime O_3 concentrations (red dashed line in Fig. 3.14b), with the O_3 maximum and 8-hour average O_3 reduced by about 21% and 24%. Decreasing NO_x emissions leads to

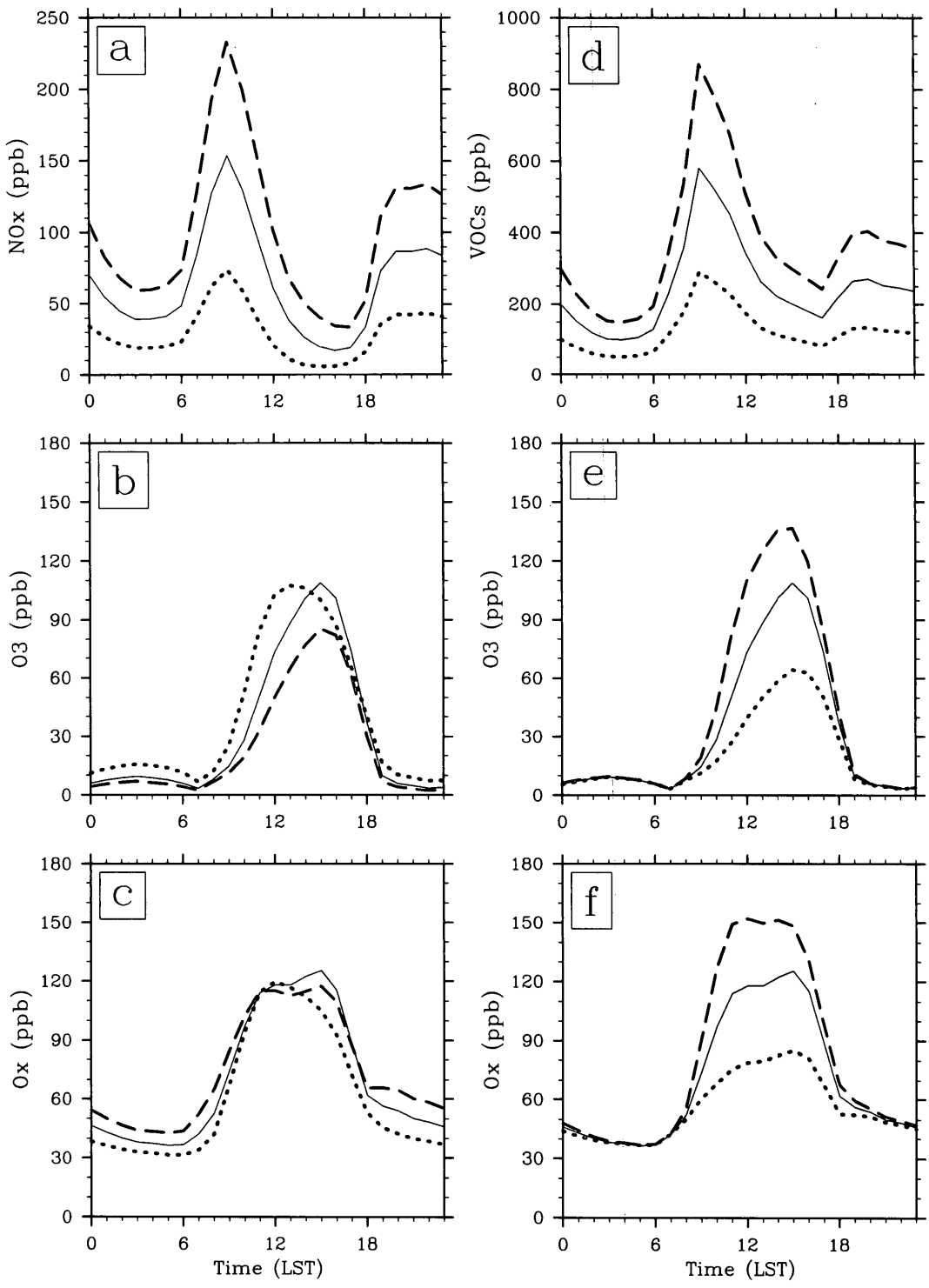

Figure 3.14: Sensitivity of averaged O_3 concentrations to emissions of NO_x (left) and VOCs (right). The responses of (a) NO_x, (b) O_3, and (c) O_X to changes in NO_x emissions, and the responses of (d) VOCs, (e) O_3 and (f) O_X to changes in VOC emissions. dashed line - emissions increased by 50%; dotted line - emissions decreased by 50%; light solid line - standard emission.

O_3 concentrations increase in the morning and early afternoon and little decrease in the later afternoon. The 8-hour average O_3 is increased 11%, but the afternoon O_3 maximum is decreased 1 ppb. Contrary to O_3, O_X is more steady (Fig. 3.14c) when increasing/decreasing NO_x emissions, more NO does decrease O_3, but does not decrease O_X. So O_3 reduction is likely caused by NO titration effects.

Why does decreasing NO_x emission tend to decrease O_3 maximum averaged over all RAMA measurement sites in the MC area? Figure 3.15 illustrates the effect of emission changes of NO_x on near-surface O_3 for the individual O_3 RAMA measurement sites. It clearly shows that decreasing NO_x emission does decrease a little the O_3 maximum for the northern sites, especially for the northeast sites, but not for the sites in the center and south area. In the north, especially in the northeast zone, the O_3 maximum is reduced whenever NO_x emission is increased or decreased; This results suggest that O_3 formation is VOC-sensitive in the MC area during the period of March 12-15, 2006. While O_3 production is near the ridge line (appearing in an O_3 isopleth diagram in Fig. 1.1) in the north, especially in the northeast zone, where the O_3 production has a maximum value with respect to changes in NO_x emissions.

Figure 3.16 shows the sensitivity of model surface OH and HO_2 concentrations to changes in emissions of NO_x and VOCs. OH decreases with increasing NO_x (Fig 3.16a), while increasing slightly with increasing VOCs in the morning time (Fig 3.16c). This result shows that the reaction R1.12 represents the major sink of odd hydrogen radicals; and VOCs are still sources of odd hydrogen (Sillman, 1995). Thus the O_3 production is under the VOC-limited regime and the rate of O_3 production is proportional to R1.7 and R1.8, which is related to the concentrations of VOCs and OH or HO_2 and RO_2. Figure 3.17 shows the averaged difference of simulated OH, HO_2, and O_3 concentrations due to emission changes in NO_x and VOCs. With NO_x emission changing, the changes in O_3 concentrations (Fig. 3.17c) coincide with the changes in OH concentrations (Fig. 3.17a), as the VOC concentrations are not

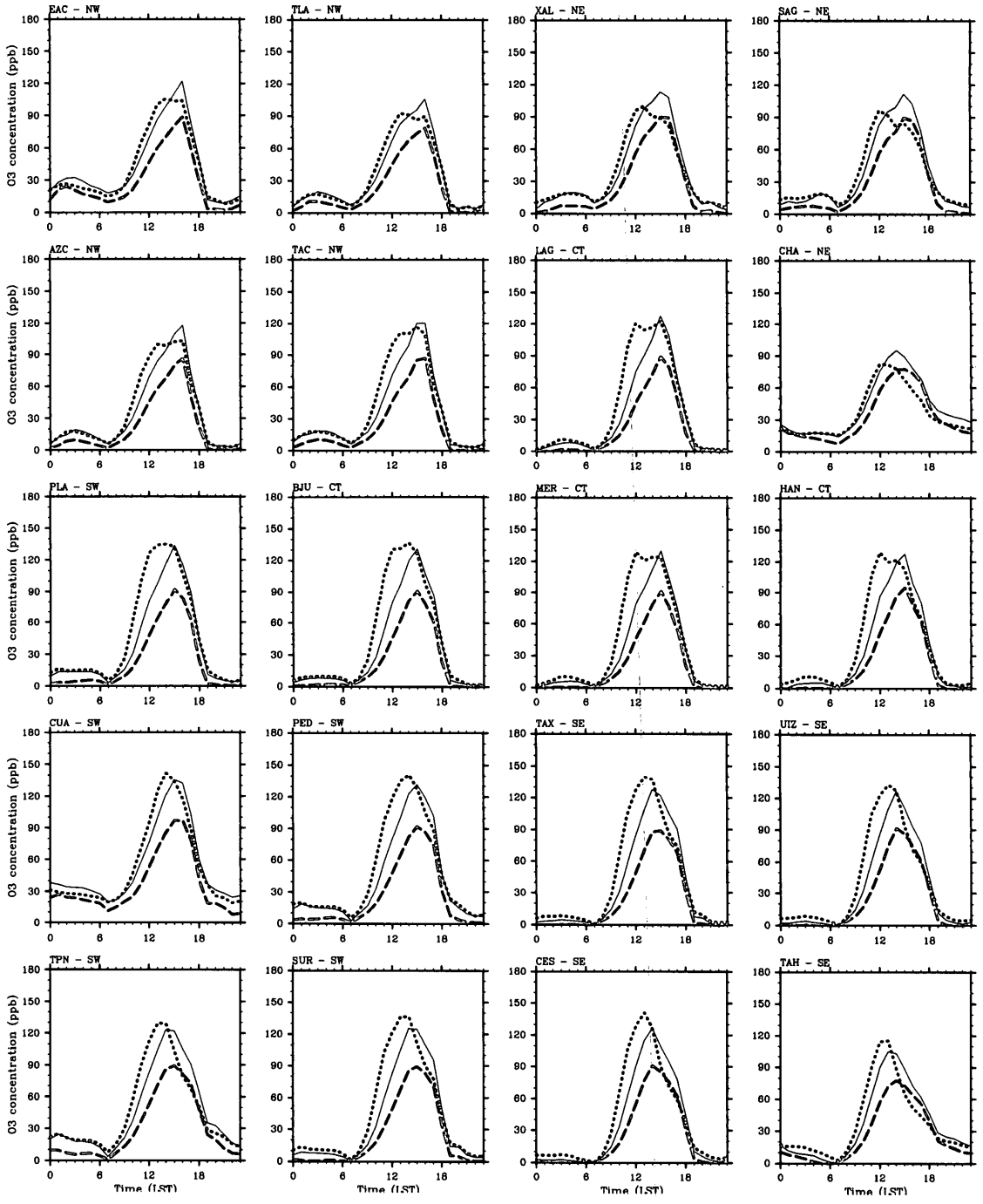

Figure 3.15: Sensitivity of O_3 concentrations to changes in NO_x emissions, averaged over the 4 day period during March 12–15, 2006, at the RAMA sites. Red dashed line - NO_x emissions increased by 50%; blue dotted line - NO_x emissions decreased by 50%; light solid line - standard emission.

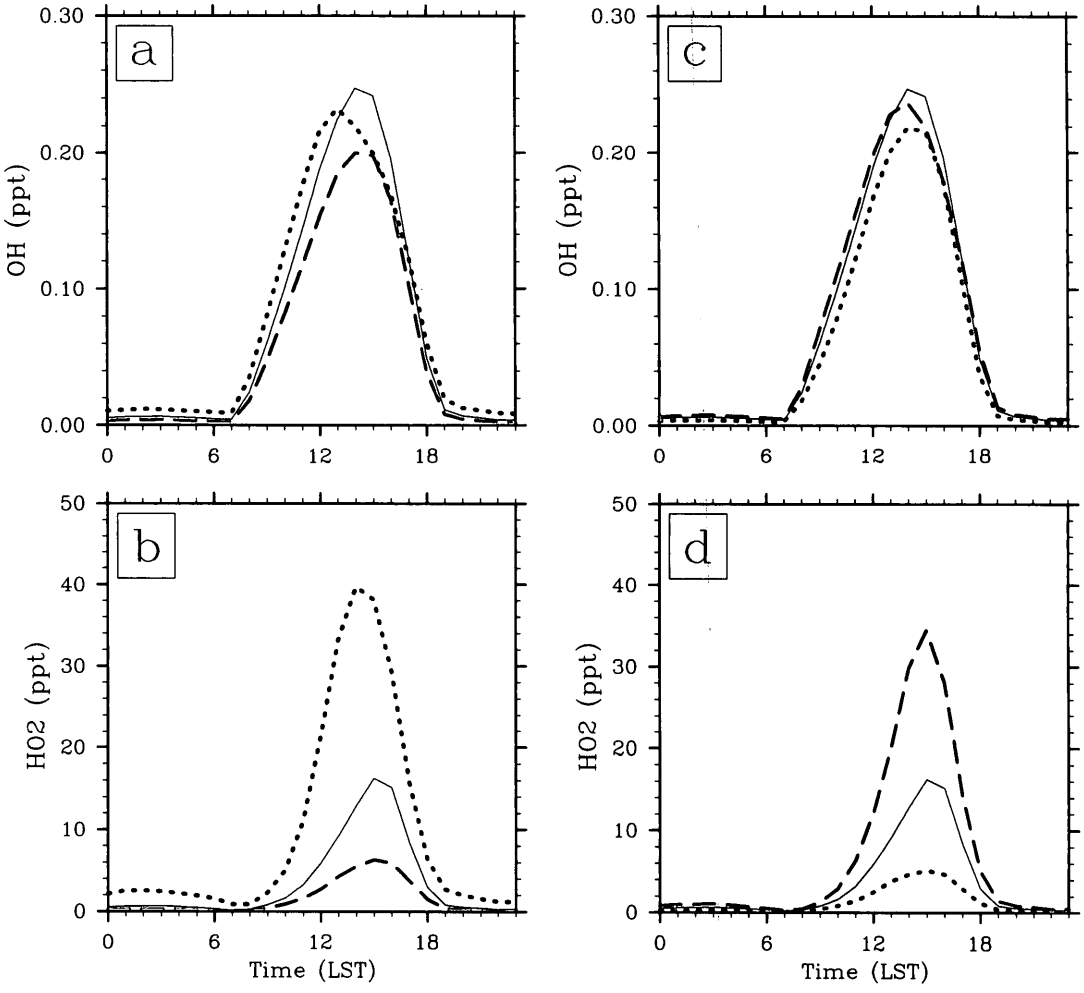

Figure 3.16: Sensitivity of OH and HO_2 concentrations to emissions of NO_x (left) and VOCs (right), averaged over all RAMA sites and 4-day period during March 12-15, 2006. dashed line - emissions increased by 50%; dotted line - emissions decreased by 50%; light solid line - standard emission.

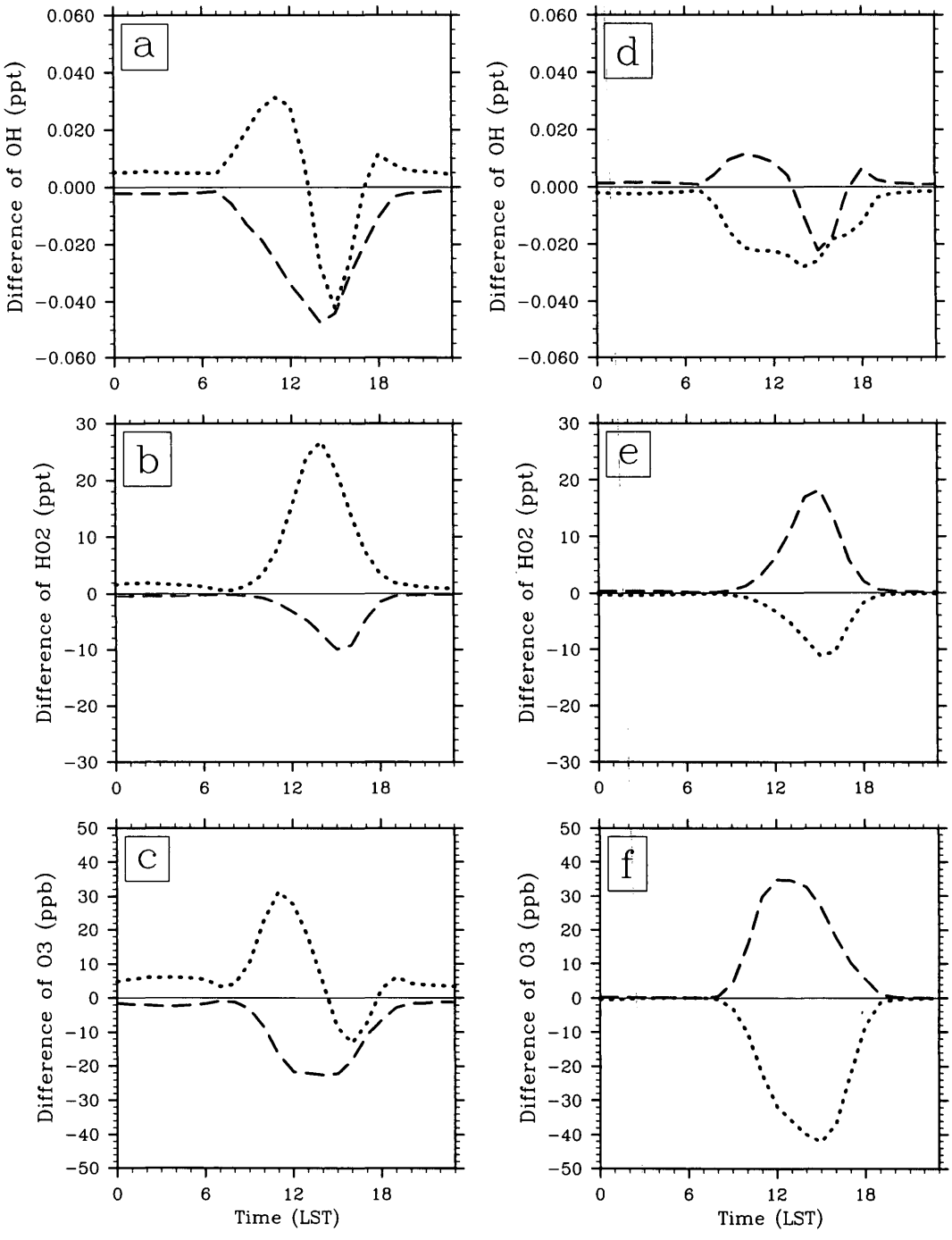

Figure 3.17: Averaged difference of OH, HO_2, and O_3 concentrations, between simulations with emission rates changes in NO_x (left) and VOCs (right) and with standard emission rates. dashed line - emissions increased by 50%; dotted line - emissions decreased by 50%; light solid line - standard emission.

changing. Increased NO_x emissions tend to destroy OH by reaction (R1.12); when less OH to react with VOCs (R1.8), there is less generation of RO_2 and HO_2, and less regeneration of OH, and less production of O_3 (red dashed lines). With less destruction of OH (R1.12) as NO_x emissions decreased, more OH reacts with VOCs (R1.8), more HO_2, OH, and O_3 are produced. But with less NO reacting with HO_2 (R1.10), OH regeneration and O_3 production are reduced in the afternoon (blue dotted lines). As VOC emission changes, in contrast, the changes in O_3 concentrations (Fig. 3.17f) are consistent with the changes in HO_2 concentrations (Fig. 3.17e), which are associated with VOC concentrations. The concentrations of O_3 and HO_2 all increase with increasing VOC emissions, and decrease with decreasing VOC emissions.

The simulated distribution of afternoon averaged NO_y and ratios of O_3/NO_y, $O_3/(NO_y - NO_x)$, and $HCHO/NO_y$ at the lowest model level are shown in Fig. 3.18, where $NO_y = NO_x + N_2O_5 + HONO + HNO_3 + PAN$. NO_y and ratios of O_3/NO_y, $O_3/(NO_y - NO_x)$, and $HCHO/NO_y$ can be used as indicators to assess the relative effect of VOCs versus NO_x (Sanford, 1995; Sillman, 1995). NO_y works as an indicator because it is related to the ratios of NO_x/VOCs NO_y also reflects the photochemical aging of an air plume which is associated with O_3 sensitivity. The VOC-sensitive regime is associated with a higher value of NO_y and lower values of O_3/NO_y, and $O_3/(NO_y - NO_x)$. Since the production of $HCHO$ is roughly proportional to the total rate of reactions of VOCs with OH, the ratio $HCHO/NO_y$ as a reactivity-weighted ratio of NO_x/VOCs, can also be used as one of indicators that VOC-sensitive regime is associated with low $HCHO/NO_y$ ratio (Sillman, 1995). This figure also indicates that the VOC-sensitive area (blue area) is especially in the center and south zone of the MC area, which generally matches with the area talked above in Fig. 3.15.

Figure 3.19 shows the sensitivity of O_3 to emission changes in NO_x and VOCs at the T0, T1, T2 sites. It can be seen that O_3 production is VOC-sensitive at the Mexico City site T0. T0 is located in the north zone of Mexico City, the O_3

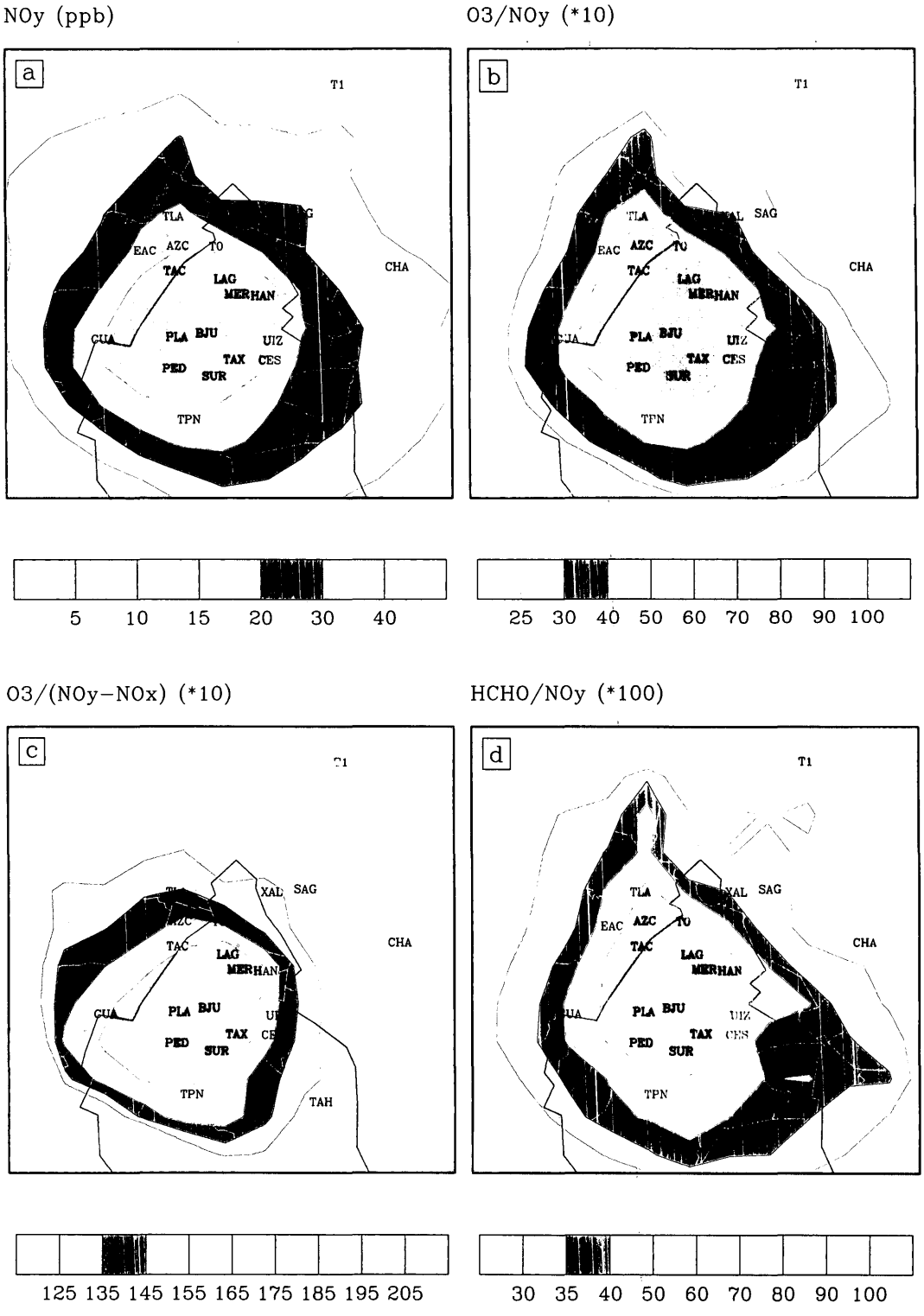

Figure 3.18: The spatial distribution of NO_y, ratios of O_3/NO_y, $O_3/(NO_y - NO_x)$, and $HCHO/NO_y$ at the lowest model level, simulated with standard emissions, averaged over 12:00-17:00 LST during March 12-15, 2006.

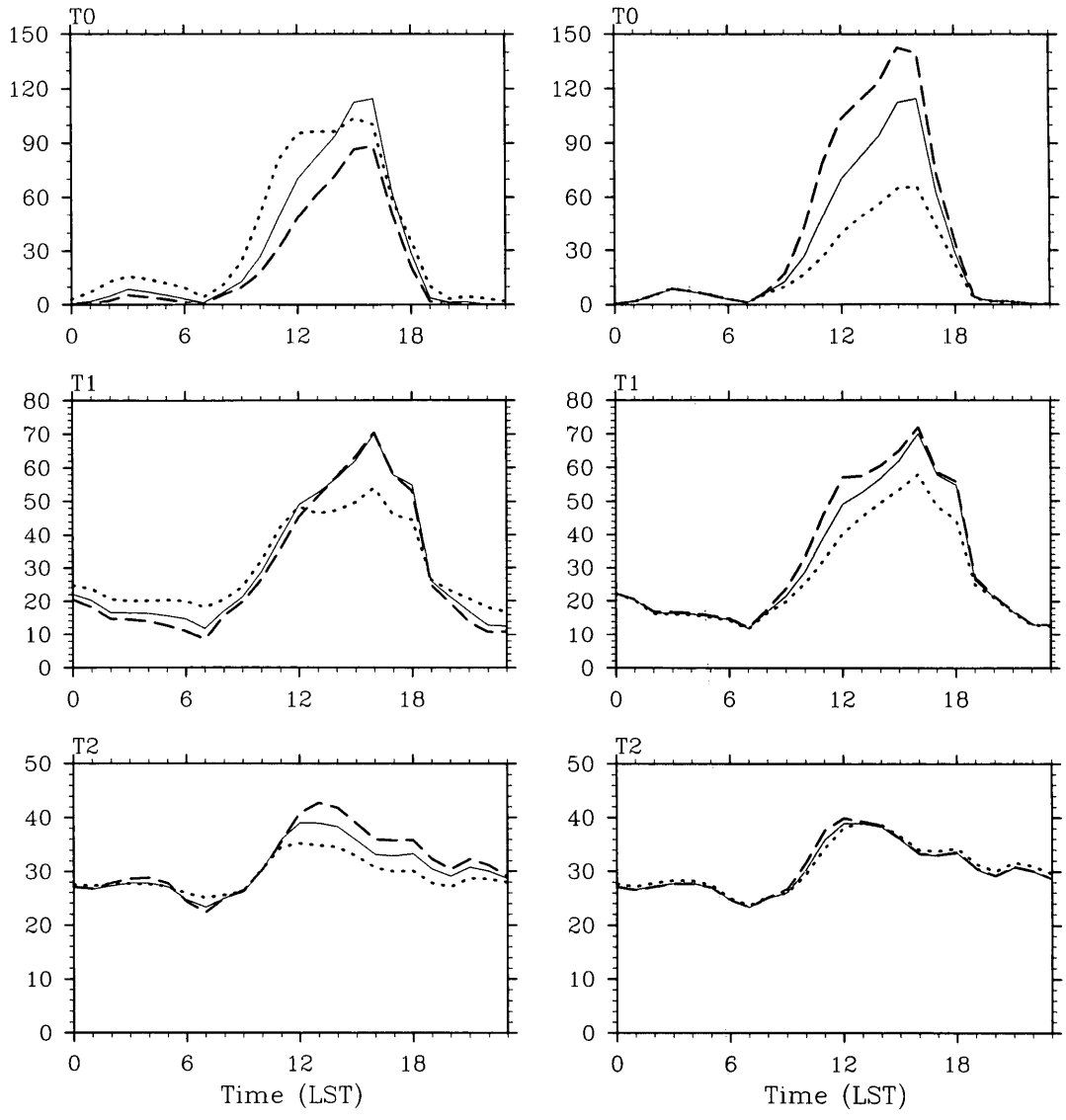

Figure 3.19: Sensitivity of O_3 concentrations to changes in emissions of NO_x (Left) and VOCs (Right) at the sites of T0, T1 and T2. Red dashed line - emissions increased by 50%; blue dotted line - emissions decreased by 50%; light solid line - standard emission.

maximum is enhanced with increasing VOC emissions; while it is reduced whenever NO_x emission is increased or decreased, like other site in the north zone. Downwind site T1, the O_3 maximum didn't change with increase in both emissions of NO_x and VOCs, it decreased with decrease in both emissions. It looks like that O_3 production is sensitive to both NO_x and VOCs at T1. At site T2, anthropogenic VOC emissions are pretty small compared with the biogenic VOC emissions: increase or decrease in anthropogenic VOC emissions does not make any noticeable difference in O_3 production. The O_3 maximum is not sensitive to VOC emissions at site T2, while it is sensitive to NO_x emissions, increasing NO_x emissions tends to increase O_3 maximum, and decreasing NO_x emissions tends to reduce O_3. This result suggests that the O_3 formation is VOC-limited in the city site T0, it is possibly sensitive to both NO_x and VOC emissions at downwind site (T1), and sensitive to NO_x at further downwind site T2. It also suggests that VOC emission reductions would be most effective in reducing local O_3 production, while NO_x emission reduction may be more important for contributions to regional O_3 and other oxidants, which is consistent with Stephens *et al.* (2010).

With the current estimates of NO_x and VOC emissions, the O_3 formation in Mexico City urban area is VOC-limited, which is consistent with the studies in Tie *et al.* (2007) and Lei *et al.* (2007). The O_3 formation is sensitive to both NO_x and VOC emissions at the downwind suburban area, and transitions to NO_x sensitive at the further downwind rural area.

3.4 OH reactivity

As suggested by the results presented in section 3.3, the chemical O_3 production in Mexico City area is VOC-limited, The chemical O_3 production can be approximated by the oxidation of VOCs (including CO, oxygenated hydrocarbons such as

$HCHO$, anthropogenic hydrocarbons, and biogenic hydrocarbons) by OH (Sillman, 1995, Kleinman, 2004), thus as discussed in Chapter 1, the O_3 production rate can be written as:

$$P_{O_3} = \sum Y_i k_i [VOC_i][OH]$$

Where P_{O_3} is the rate of O_3 production, Y_i is the total number of peroxy radicals formed in R1.8, and k_i is the rate constant for the i^{th} VOC with OH. To compare the contributions of the individual VOC species to O_3 production rate, the VOC data are presented in OH reactivity, defined for a single VOC by

$$VOC_i = k_i [VOC_i]$$

Figure 3.20 shows the daytime averaged OH reactivity during March 12-13, 2006, at RAMA (averaged over all RAMA sites), T0, T1, and T2 sites. The OH reactivity is calculated from the model simulations with the standard emission rates. The total daytime averaged OH reactivity was estimated $70s^{-1}$ at T0, $13s^{-1}$ at T1, and $2.8s^{-1}$ at T2. NMHCs (alkanes, alkenes, and aromatics) provide the major OH reactivity for T0 and T1 (67% and 61%, respectively), and other VOCc, including CO and carbonyls (oxygenated hydrocarbons) provide the most OH reactivity with 54% at T2 site. Alkenes are the largest contributor to the daytime OH reactivity at the urban site T0, followed by carbonyls, they provide OH reactivity with 31.4% and 23.7%, respectively, and CO makes relatively smaller contribution (~9%) At the downwind site T1, both alkenes and carbonyls are most important VOCs in terms OH reactivity, with 28.5% from alkenes, and 26.7% from carbonyls. Alkenes lose their importance further downwind at site T2, carbonyls dominated the OH reactivity, followed by CO (33% from carbonyls, 21% from CO, and 20% from alkenes). It is apparent that from T0 to downwind T2, OH reactivity is transforming from being

dominated by alkenes to being dominated by carbonyls, and CO plays a relatively more important role in OH reactivity.

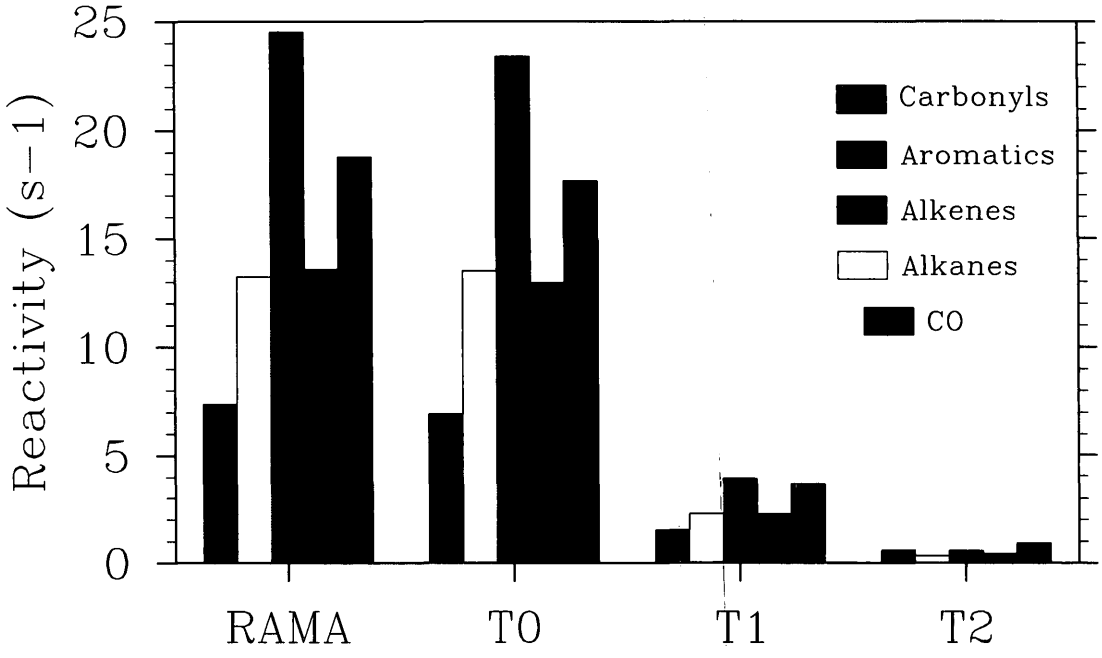

Figure 3.20: Daytime averaged OH reactivity (s^{-1}) contributed from CO, alkanes, alkenes, aromatics, and carbonyls for RAMA, T0, T1, and T2 sites.

From the detailed contributions from the VOC species (Fig. 3.21), the most important VOCs with respect to the calculated OH reactivity from model results, is ALD (acetaldehyde) for all three sites. This is consistent with the observation results, which was discussed in Molina *et al.* (2010), that formaldehyde and acetaldehyde were the two most important measured VOC species in terms of OH reactivity in the MCMA. But it can be also seen that formaldehyde ($HCHO$) is not an important contributor for sites T0 and T1, which is largely underestimated compared to the observation results (Molina *et al.*, 2010). The discrepancy may be due to that the current inventories substantially underestimated the emission of formaldehyde and

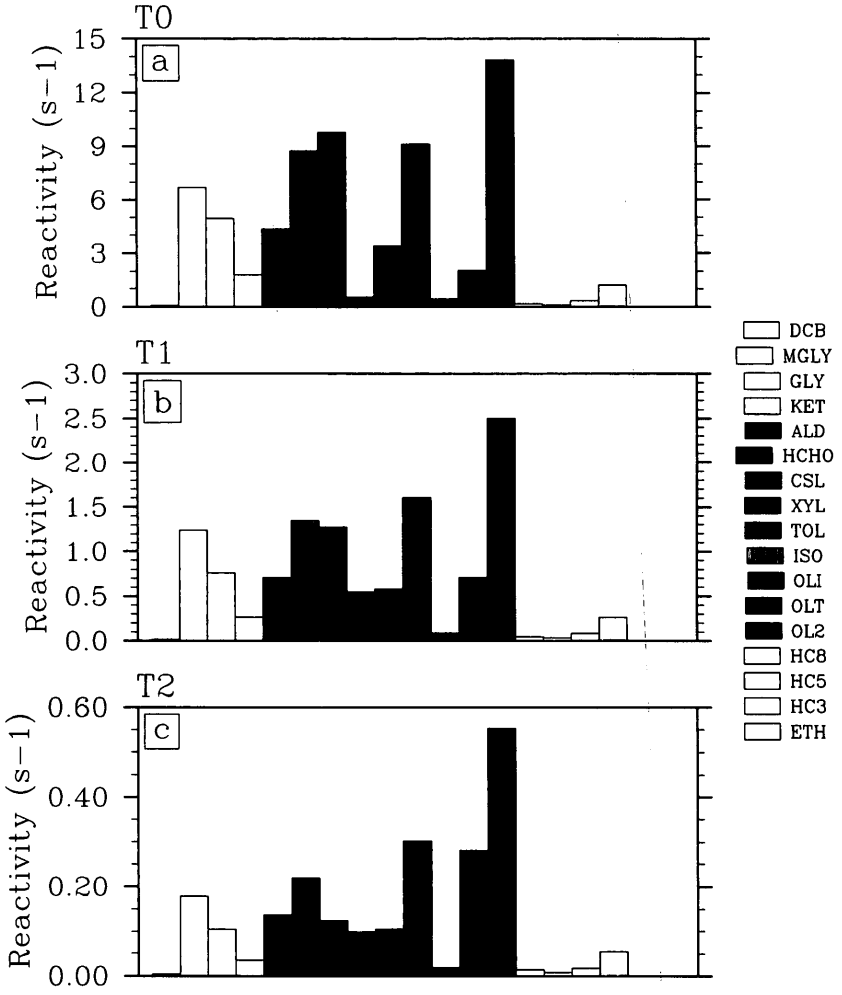

Figure 3.21: Daytime averaged OH reactivity (s^{-1}) contributed from detailed VOC species at sites T0, T1, and T2.

ethene (see Table 2.2). Ethene reacts relatively quickly to form $HCHO$ and therefore is an important contributor to secondary $HCHO$ formation (Garcia *et al.*, 2006). While at site T2, formaldehyde is the third most important VOCs, after xylene. Besides xylene, Olefins (OLI and OLT) also make significant contributions to OH reactivity, especially for T0 and T1. The simulated concentrations of olefins are ~20 ppbv for 24-hour average and ~34 ppbv for morning rush hour average, which is generally consistent with those observation of 19 ppbv and 41 ppbv for 24-hour and morning rush hour mean (Velasco *et al.*, 2009).

Based on the model results of the calculated OH reactivity, acetaldehyde, olefins and xylenes, species with relatively short lifetimes, are the most important O_3 precursors. They dominate OH reactivity, and therefore the O_3 production in the MC area. In the rural area, OH reactivity and O_3 production are dominated by oxygenated VOCs and CO.

Chapter 4

Sensitivity of Ozone Concentration to Diurnal Variation of Emission

The sensitivity of O_3 to surface NO_x and VOC emissions was discussed in chapter 3, and it was shown that the chemical O_3 formation is under a VOC-limited regime in the Mexico City area. Tie *et al.* (2007) discussed the role that the oxidation of VOCs during morning plays in controlling O_3 production, and that the titration reaction of $NO + O_3$ is mainly responsible to the O_3 minimum during early morning. Their results suggested that not only the magnitudes of the emissions of NO_x and VOCs have important impacts on O_3 formation, but the timings of the emissions of NO_x and VOCs also play important roles in determining the daily O_3 maxima and its diurnal variations. The response of O_3 concentrations to changes in the diurnal behavior of the surface emissions (NO_x and VOCs) is discussed in this chapter.

4.1 Emission scenarios

In order to better understand the relationship between O_3 concentrations and the surface missions of NO_x and VOCs in different time periods of the day, and the individual contributions of NO_x and VOC emissions to O_3 concentrations as well as the afternoon O_3 maxima, simulations were performed in which the diurnal variations of surface emissions (see Fig. 2.1) were changed according to the following four scenarios: (a) the emission rates were daily-averaged, so that no diurnal cycle effects of emissions were considered (denoted as *Run1-Mean*); (b) higher emission rates were used in morning time (0 - 11 AM) and lower rates between afternoon and evening (12 - 23 PM) (denoted as *Run2-AM*); (c) lower emission rates were used in morning time and higher rates between afternoon and evening (denoted as *Run3-PM*); (d) the diurnal cycles of emission rates were delayed for 2 hours (denoted as *Run4-Delay*). In each scenario, the *total* diurnal emissions of each species remain the same as the standard emissions. The four emission scenarios are summarized in the table 4.1. As an illustration, the four emission scenarios for NO at the center of Mexico City are shown in Fig. 4.1. In the simulations, each of the 4 emission scenarios was applied to (1) all emission species (CO, NO_x, VOCs, etc.); (2) NO_x only; and (3) VOCs only. Therefore, 12 simulations were performed in all. In these simulations, only surface emissions were changed, while other processes (such as transport, chemical scheme etc.) were unchanged. Therefore, the changes of O_3 concentrations are due to the changes of the surface emissions. The simulations with the 4 emission scenarios in the three applications were compared with the simulations using the standard emission (denoted as *Run0-CTRL*), which were discussed in chapter 3. The comparisons were averaged over all RAMA measurement sites which have measurements, and the 4 day period during March 12–15, 2006.

Table 4.1: Emission scenarios

Run1-Mean	Emission rates were daily-averaged
Run2-AM	Higher emission rates in 0-11 AM & lower rates in 12-23 PM
Run3-PM	Lower emission rates in 0-11 AM & higher rates in 12-23 PM
Run4-Delay	Diurnal cycles of emission rates were delayed for 2 hours

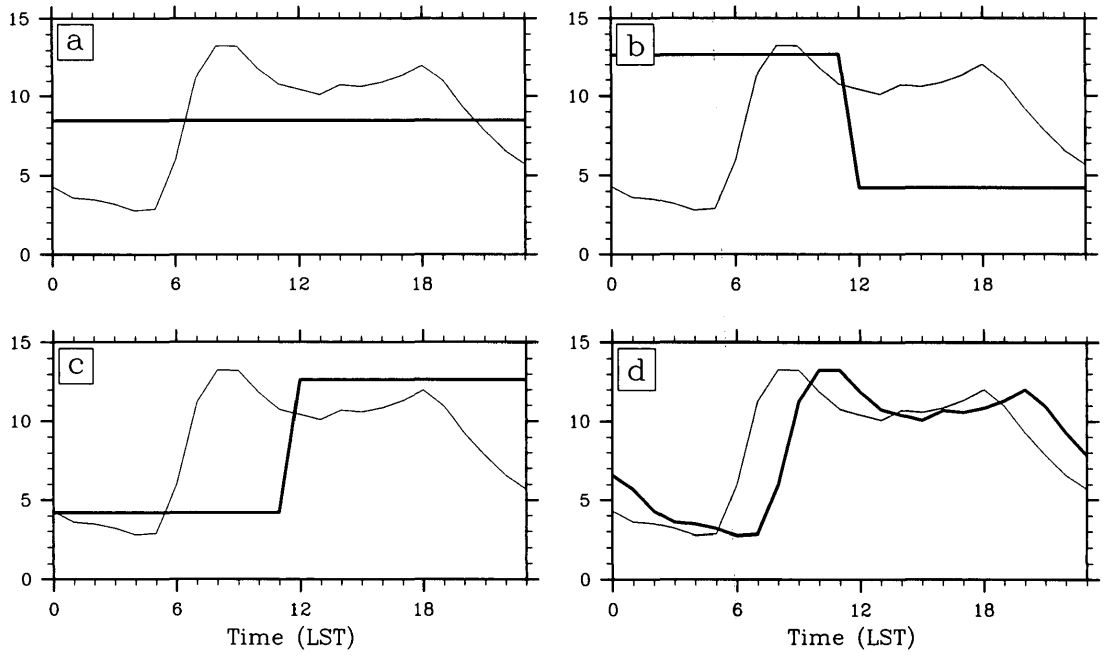

Figure 4.1: The proposed diurnal variations of NO emission rate (mole/s) centered at Mexico City (99.14W, 19.43N), changed according to the 4 emission scenarios: (a) daily average - no diurnal cycle (red line), (b) higher emissions in morning and lower emissions in afternoon (blue line), (c) lower emissions in morning and higher emissions in afternoon (green line), (d) the diurnal cycle delayed for 2 hours (brown line). The light solid lines represent the standard NO emission rate.

4.2 Sensitivity of ozone to diurnal variation of emissions

Figure 4.2 shows the diurnal variations of surface CO, VOCs, NO, NO_2, and NO_x concentrations simulated with all emission species changed according to the 4 different emission scenarios. This figure also includes simulation from *Run0-CTRL* for comparison. Despite the different variations of the surface emissions, the diurnal variations of CO, VOCs, NO, NO_2, and NO_x show some similarity. For example, there are morning peaks in all the simulations. In the case of mean surface emission (*Run1-Mean*, red solid lines), where there are no diurnal variations of the CO, VOCs, NO, and NO_2 emissions, the concentrations of these pollutants, however have strong diurnal cycles, indicating that other processes (such as evolution of the PBL and vertical mixing in the PBL) play important roles in the diurnal variations of these air pollutants. For example, as suggested in Tie *et al.* (2007), the patterns of diurnal variation of the primary surface emitted pollutants (such as CO, NO etc.) can be roughly determined by the ratio of the diurnal variations of the emissions and the diurnal variation of the PBL heights. With the constant emission rate (no diurnal variations of emissions), the variability as indicated by red solid lines are strongly controlled by the diurnal variation of the PBL height (see Fig. 4.2f for PBL height).

Furthermore, the different diurnal variations of the pollutants due to the 4 different emission scenarios indicate that diurnal variations of the surface emissions have also important effects on magnitudes of the morning and evening maxima in these pollutants. For example, the highest morning peaks of these pollutants are shown in the blue dashed lines (*Run2-AM*), and lowest peaks are indicated by the green dotted lines (*Run3-PM*). This result is understandable because the *Run2-AM* has highest morning emissions and *Run3-PM* has lowest morning emissions. In the

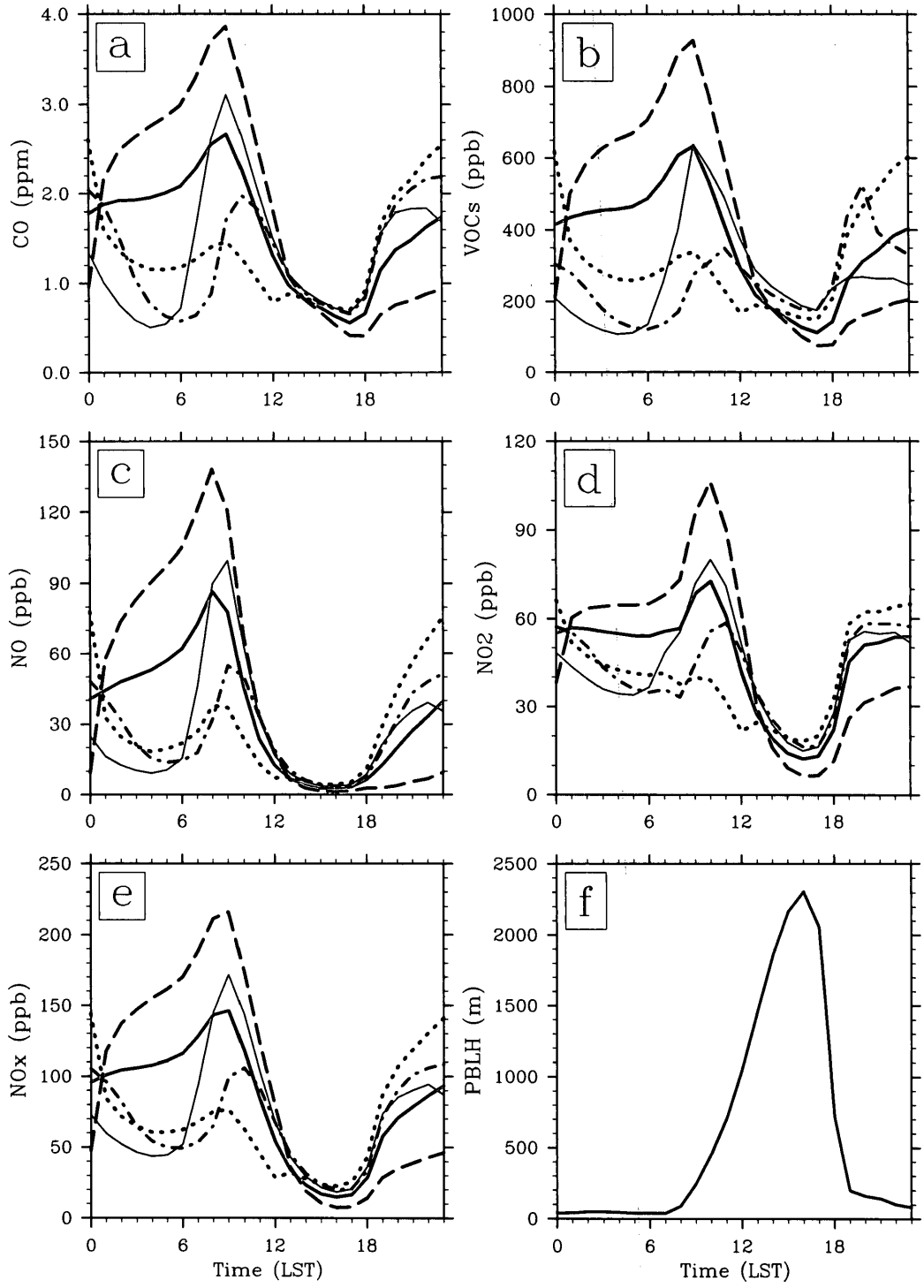

Figure 4.2: Averaged diurnal cycles of (a) CO, (b) VOCs, (c) NO, (d) NO_2, and (e) NO_X concentrations at the surface, for simulations with all emission rates changed according to the 4 emission scenarios: red solid line - *Run1-Mean*; blue dashed line - *Run2-AM*; green dotted line - *Run3-PM*; brown dash-dotted line - *Run4-Delay*. The light solid lines represent simulations with the standard emission rates (*Run0-CTRL*).

case of lower emission in the morning (*Run3-AM*, green lines), the diurnal variations of the pollutants in the morning are not obvious as the other 3 cases, showing that not only the PBL height, but also the surface emissions of the pollutants during the morning, play important role in their diurnal variations. The second lowest morning peaks are shown by the brown dash-dotted lines (*Run4-Delay*). This result suggests that the morning peaks can be greatly reduced when the emission peaks take place after 10 AM when the PBL heights start to quickly rise (see Fig. 4.2f for PBL height). So that *changes in emission timings have important effects on the maximum values of pollutants.*

The changes in O_3 precursors from the different emission scenarios have important impacts on O_3 formation and O_3 concentrations. Figure 4.3 shows that all simulations have an O_3 maximum in the afternoon and an O_3 minimum in the early morning. The O_3 maximum and minimum have different responses to the different emission changes. For example, compared to the control run (*Run0-CTRL*), the O_3 maximum that occurs at 3 PM is higher for *Run1-Mean* and *Run2-AM*, but lower for *Run3-PM* and *Run4-Delay*. On the other hand, the O_3 minimum that occurs at 7 AM is lowered for *Run1-Mean* and *Run2-AM*, but becomes higher for *Run3-PM* and *Run4-Delay*, while the O_3 minimum occurs at midnight. These results indicate that *changes in the timing of ozone precursor emissions play different roles in controlling the O_3 afternoon maximum and morning minimum* in the MC source area.

As compared to the standard run, the differences of the surface O_3 concentrations due to the 4 different emission scenarios are shown in Fig. 4.4. It can be seen that the O_3 concentration in the afternoon is increased, with maximum increase about 20 ppbv around 14 PM for *Run2-AM*, indicating that *increase in morning emissions tends to enhance the afternoon O_3 concentrations in the early afternoon.* However the daytime O_3 is decreased, with maximum decrease about 11 ppbv around 14 PM for *Run3-PM* and about 11 ppbv at 12 PM for *Run4-Delay*, suggesting that *decrease*

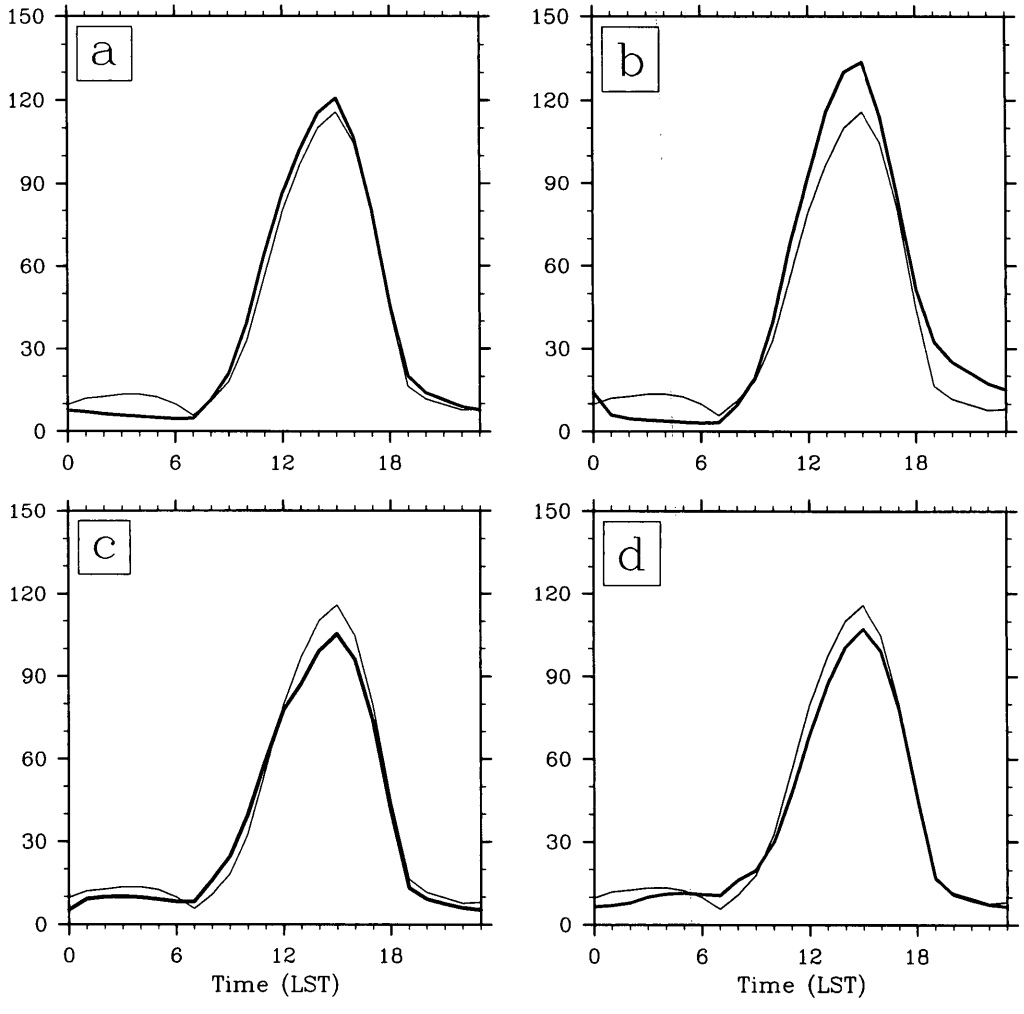

Figure 4.3: Averaged diurnal cycles of O_3 concentrations (ppbv) at the surface, for simulations with all emission rates changed according to the 4 emission scenarios: (a) *Run1-Mean*; (b) *Run2-AM*; (c) *Run3-PM*; (d) *Run4-Delay*. The light solid lines represent O_3 concentrations simulated with the standard emission rates (*Run0-CTRL*).

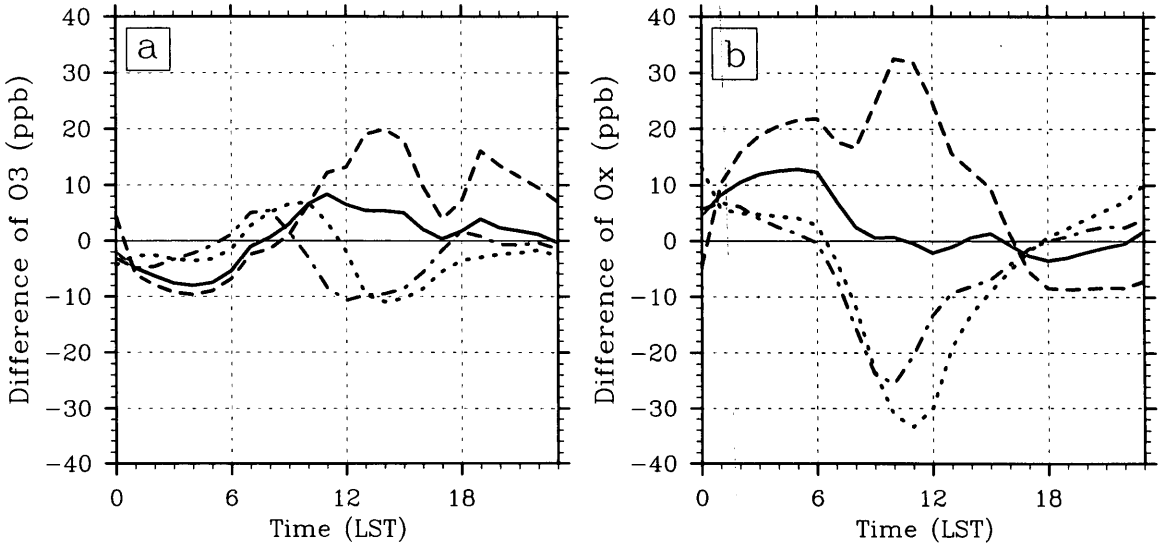

Figure 4.4: Averaged differences of surface O_3 and O_X concentrations (ppbv), between simulations with standard emission rates and with all emission rates changed according to the 4 emission scenarios: red solid line - *Run1-Mean*; blue dashed line - *Run2-AM*; green dotted line - *Run3-PM*; brown dash-dotted line - *Run4-Delay*.

in morning emissions and emission delaying tend to lower the morning maximum peaks of NO_x and VOCs, thus reduce the O_3 concentrations in daytime as well as the afternoon O_3 maxima.

In addition, the concentrations of O_X due to the 4 different emission scenarios are shown in Fig. 4.5. The daytime O_X concentrations, similar to O_3, are increased for the case *Run2-AM* (blue line), and decreased for the cases *Run3-PM* (green line) and *Run4-Delay* (brown line). But the maximum increase or decrease (Fig. 4.4b) are all occurred in the late morning (around 10-11 AM) instead of the early afternoon for O_3. So that increasing morning emission tends to an increase in O_X, and decreasing morning emission and emission delaying tend to reduction in O_X in daytime, especially in the late morning. During nighttime, the changes of O_X and O_3 are different: decreasing emissions during the afternoon (12-23 PM) results in increase of O_3, but

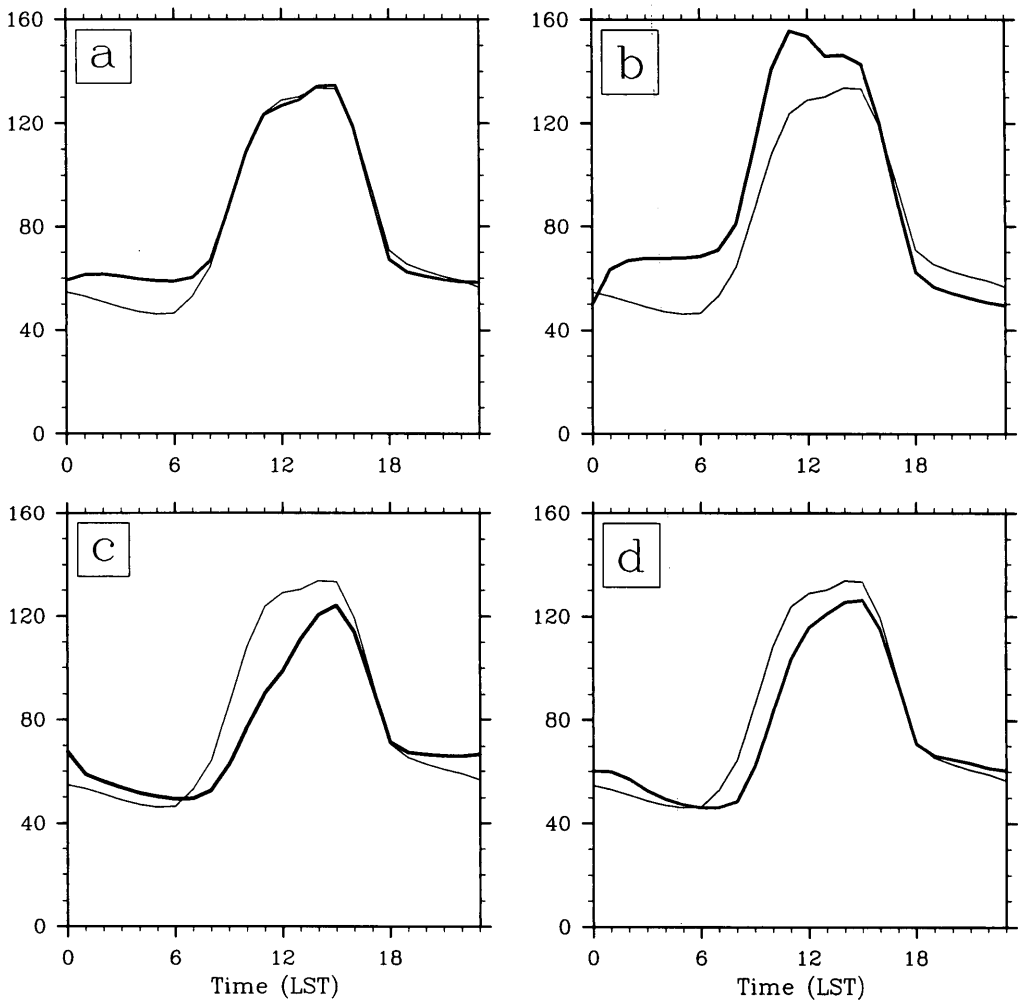

Figure 4.5: Averaged diurnal cycles of O_X concentrations (ppbv), for simulations with all emission rates changed according to the 4 emission scenarios: (a) *Run1-Mean*; (b) *Run2-AM*; (c) *Run3-PM*; (d) *Run4-Delay*. The light solid lines represent O_X concentrations simulated with the standard emission rates (*Run0-CTRL*).

decrease of O_X in the evening; however increasing emissions during the morning (0-11 AM) results in decrease of O_3, but increase of O_X in the early morning (0-7 AM).

The changes in the timing of ozone precursor emissions will also cause changes of O_3 concentrations in the downwind suburb area. Figure 4.6 shows the spatial distribution of changes in averaged afternoon O_3 maxima (averaged over 14:00-16:00 LST during March 12-15, 2006) due to the 4 different emission scenarios. Decreasing emission in the morning (*Run3-PM*) and emission delaying (*Run4-Delay*) tend to decrease O_3 maxima only in the emission source area; while increasing morning emission (*Run2-AM*) and (*Run1-Mean*) tend to increase O_3 maxima in the downwind suburb as well as in the emission source area. For the case *Run1-Mean*, the increase of O_3 maximum is even larger in the downwind suburb than in the emission source area. The O_3 maxima are increased significantly at the T1 site (see Fig. 4.7), with ~5 ppb and 10 ppb increase for case *Run1-Mean* and case *Run2-AM*, respectively, in contrast to ~4 ppb and 14 ppb increase at the T0 site. But there is almost no O_3 changes in the T2 site, far from the source area. This result suggests that *changes in the timing of ozone precursor emissions* affects the O_3 concentrations not only in the MC source area, but also in the downwind suburb area.

4.3 Sensitivity to emission changes in NO_x or VOCs

In order to better understand the causes of the O_3 changes due to emission changes in different O_3 precursors under VOC-limited regime, we conducted simulations with only NO_x emission changes according to the four emission scenarios which discussed in section 4.1, while other O_3 precursor emissions remain unchanged. Figure 4.8a shows the results of the sensitivity of O_3 to only NO_x changing are very different from the results when all species changed as shown in Fig. 4.4. In this case, the daytime O_3 is greatly enhanced by a maximum increase about 38 ppbv at 11 AM

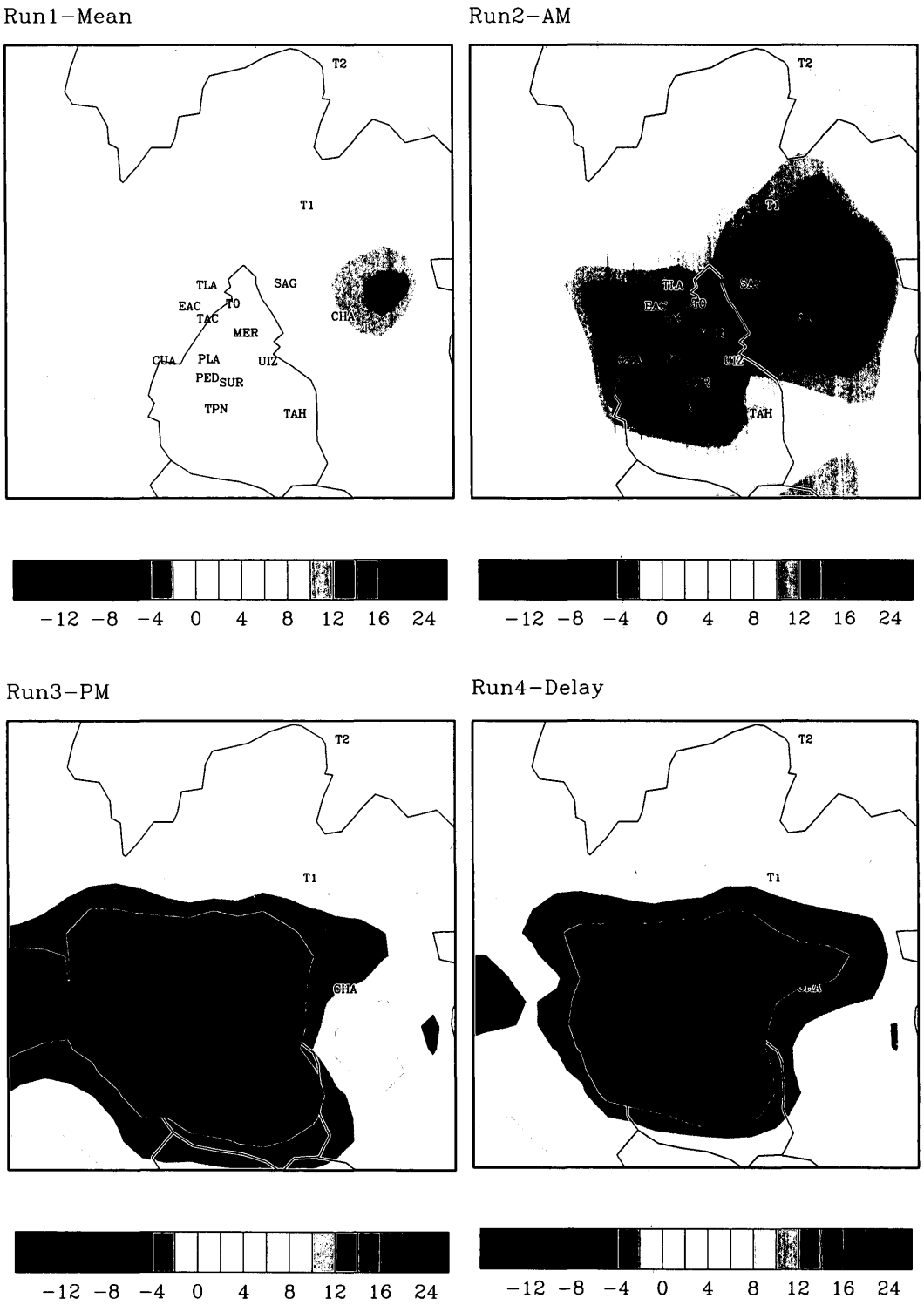

Figure 4.6: The spatial distribution of changes in surface O_3 maxima (ppbv) between simulations with standard emission rates and with all emission rates changed according to the 4 emission scenarios.

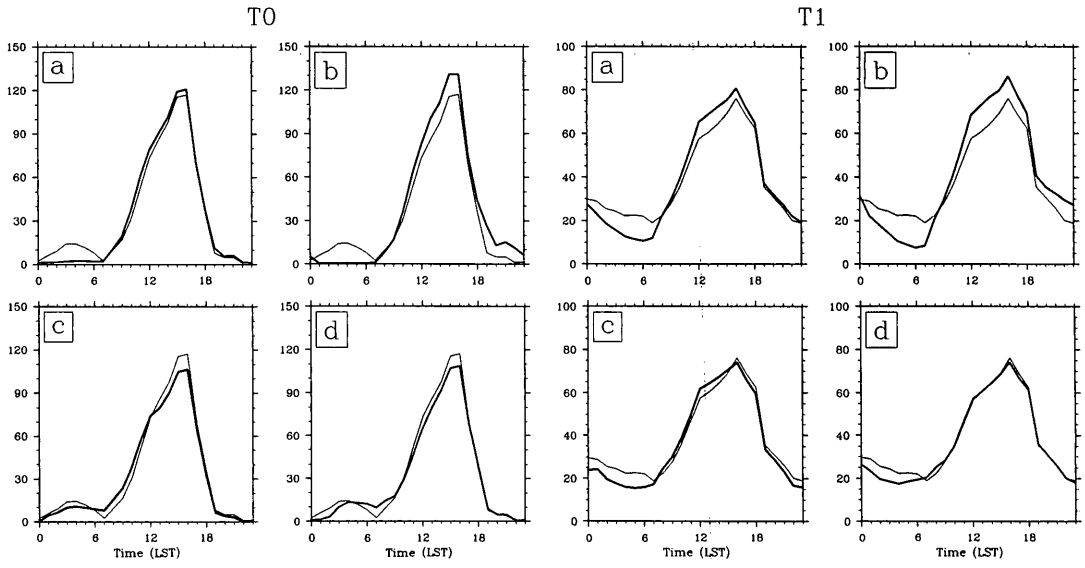

Figure 4.7: The diurnal variations of surface O_3 concentrations (ppbv) at the T0 (Left) and T1 (Right) site, for simulations with all emission rates changed according to the 4 emission scenarios: (a) *Run1-Mean*; (b) *Run2-AM*; (c) *Run3-PM*; (d) *Run4-Delay*. The light solid lines represent O_3 concentrations simulated with the standard emission rates (*Run0-CTRL*).

for *Run3-PM*, while the daytime O_3 is reduced by maximum decrease of 14 ppbv at 12 PM for *Run2-AM*. During the evening (around 19 PM), the O_3 concentration is greatly enhanced for *Run2-AM* due to significant reduction in NO_x emissions. The changes in O_X concentrations (see Fig. 4.8b) are almost contrary to changes in O_3 concentrations, for example, the O_X concentrations are greatly increased during the morning time (0-11 AM) and decreased during the afternoon and evening (12-23 PM) for *Run2-AM*. This result shows that NO_x emissions, in the morning time especially, tend to depress O_3 concentration, and the reduction of O_3 is mainly caused by NO titration effects and by OH decrease due to reaction of $OH+NO_2$. So that an increase in morning NO_x emissions leads to decrease in O_3 concentrations in the late morning and early afternoon, as well as the O_3 maximum. However a decrease in morning NO_x emissions produces an enhancement in O_3 maximum, and O_3 concentrations in the late morning especially. Similarly, a shift of the NO_x emission pattern to 2

hours later, decreases the NO_x emissions earlier in the morning (6 - 9 AM), and leads to an increase in daytime O_3 concentrations. During nighttime, photochemical production of O_3 ceases, and the concentration of O_3 is related to the NO titration effects. Increase/decrease in NO_x emissions during the afternoon and night time, tends to decrease/increase in O_3 concentrations, but tends to increase/decrease in O_X concentrations. O_3 loss is caused by NO titration reaction with NO_2 formation at night.

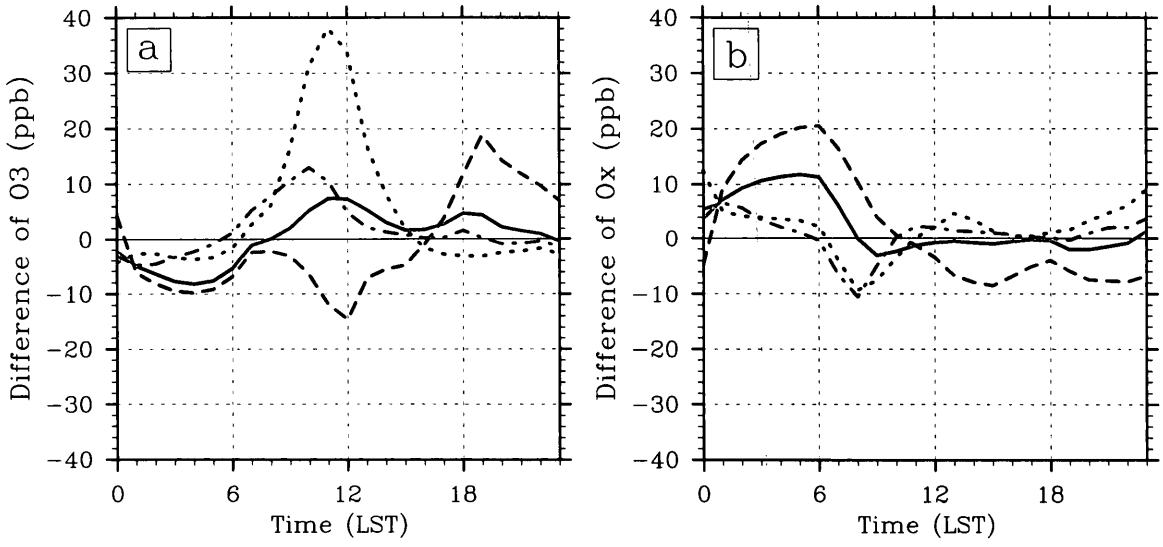

Figure 4.8: Averaged differences of surface O_3 and O_X concentrations (ppbv), between simulations with standard emission rates and with only NO_x emission rates changed according to the 4 emission scenarios: red solid line - *Run1-Mean*; blue dashed line - *Run2-AM*; green dotted line - *Run3-PM*; brown dash-dotted line - *Run4-Delay*.

Figure 4.9 shows the differences of O_3 concentrations for simulations in which there are only changes in VOC emissions according to the 4 emission scenarios, while all other O_3 precursor emissions remain unchanged. The result shows that the sensitivity of O_3 to different emission scenarios is very different from the result shown in Fig. 4.8, where only NO_x emissions were changed. In this case, the daytime O_3 concentration is greatly enhanced by maximum increase about 28 ppbv at 11 AM

for *Run2-AM*, while the daytime O_3 concentration is reduced by maximum decrease of 28 ppbv at 12 PM for *Run3-PM*. The shift of the emission pattern in VOCs to 2 hours later, decreasing VOC emissions in the earlier morning (6 - 9 AM), still reduces the daytime O_3 concentrations, especially in the late morning. The changes in O_X concentrations are consistent with that of O_3. This result also suggests that under VOC-limited regime, the morning to noontime emissions of VOCs tends to enhance daytime O_3 photochemical production, especially in the late morning. During the early morning, evening and night, the changes in O_3 concentrations are very small, suggesting that O_3 is not sensitive to VOCs in these periods, and only sensitive during daytime, especially in the morning. Decrease in VOC emissions is an most efficient way to reduce O_3 pollution in the MC area.

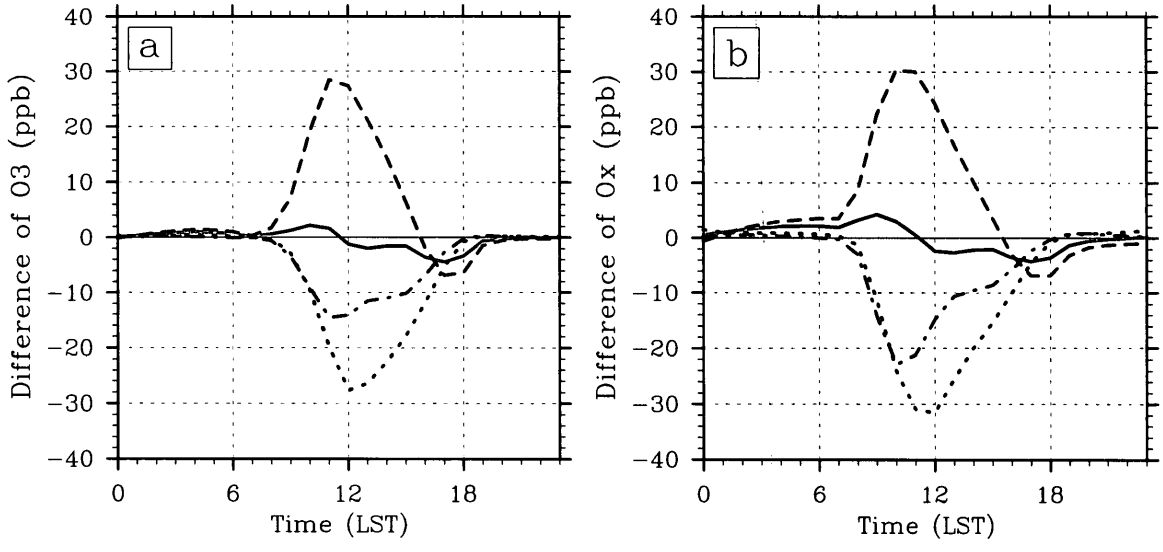

Figure 4.9: Averaged differences of surface O_3 and O_X concentrations (ppbv), between simulations with standard emission rates and with only VOC emission rates changed according to the 4 emission scenarios: red solid line - *Run1-Mean*; blue dashed line - *Run2-AM*; green dotted line - *Run3-PM*; brown dash-dotted line - *Run4-Delay*.

The above analysis shows that morning emission plays an important role in the afternoon hour O_3 concentrations in the VOC-limited regime, such as in Mexico City. Firstly, morning emitted VOCs play a much bigger role in O_3 concentrations than VOCs emitted during other times of the day. Reducing VOC emissions during morning will significantly decrease the afternoon O_3 maximum and O_3 concentrations in the late morning and early afternoon. However, the emissions of VOCs during other periods (early morning, evening, and night) have very small impacts on O_3 concentrations. Secondly, the emissions of NO_x have also important effects on afternoon O_3 maximum. The emissions of NO_x during morning tend to depress the daytime O_3 concentration, and a decrease in the emissions of NO_x during the morning lead to increase in the daytime O_3 concentration, especially in the later morning and early afternoon. The emissions of NO_x have important impacts on O_3 concentrations in the evening and the early morning. For example, decreasing the NO_x emissions during the evening greatly enhance the evening O_3 concentrations. Finally, a shift of emission pattern to 2 hours later, while keeping the total emissions unchanged (*Run4-Delay*), has important impacts on air quality. For example, the default morning emission peak is normally at 8 AM. In this alternative case, the morning emission peak is shifted to 10 AM. Between 8 and 10 AM, the PBL height is at a transition time, and grows from 100 meters at 8 AM to 500 meters at 10 AM. As a result, the NO_x and VOC concentrations are greatly diluted during the morning due to more vertical mixing with the higher PBL height, and thus produce decrease in daytime O_3 concentration and the afternoon O_3 maximum.

4.4 Sensitivity to further time shifts of emissions

To better understand the impact of shift in emission timing on the O_3 concentrations, and O_3 afternoon maximum, we performed additional simulations with all emission

patterns shifted to 2 hour earlier, 1 hour earlier, and 1 hour later. Figure 4.10 shows the response of O_3 and O_x to the 4 emission shift patterns, including emission shifted 2 hours later (*Run4-Delay*). As discussed above, the delayed emission patterns (shift of emission pattern to 1 and 2 hour later) tend to reduce the O_3 afternoon maxima and O_3 concentrations in both the late morning and early afternoon (purple dotted line and brown dot-dashed line), which results from reduced concentrations O_3 precursors in the morning. But as the emission patterns move backward (shift in emission pattern to 1 and 2 hour earlier), the higher morning emissions results in higher concentrations of NO_x and VOCs in the morning, and the daytime O_3 concentrations are increased with higher afternoon O_3 maxima (pink solid line and orange dashed line). The delayed emission patterns tend to reduce the daytime O_3 and O_x concentrations; the backward emission patterns tend to increase O_3 and O_x concentrations during the daytime.

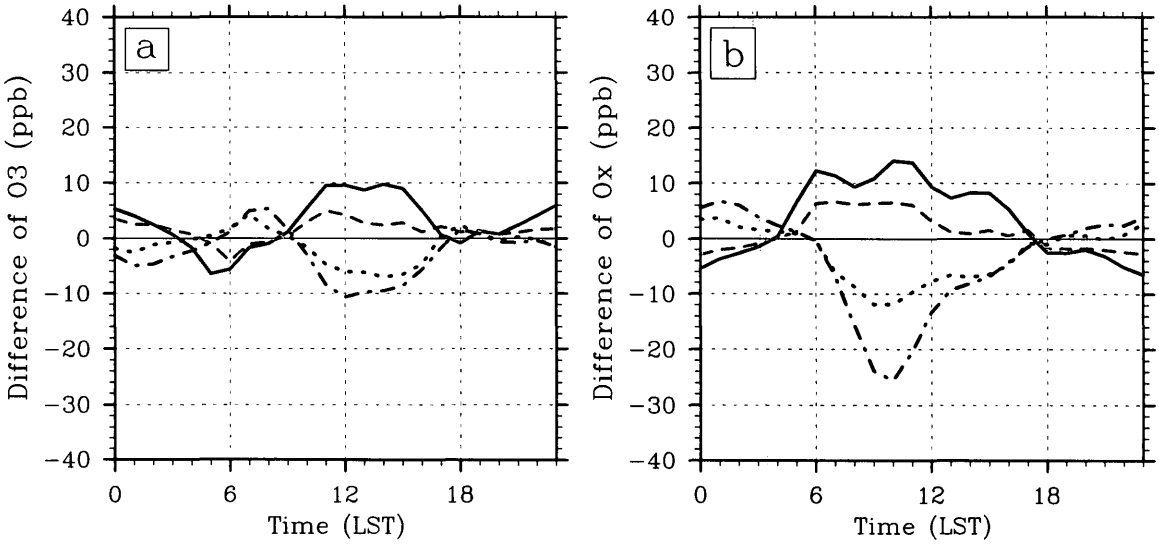

Figure 4.10: Averaged differences of O_3 and O_x concentrations (ppbv), between simulated with standard emissions and with all emission patterns shifted to: pink solid line - 2 hour earlier; orange dashed line - 1 hour earlier; purple dotted line - 1 hour later; and brown dash-dotted line - 2 hour later.

This result emphasizes that changes in diurnal variations of surface emissions have important implications for air quality: without reduction of total emission, the daytime concentrations of CO, VOCs, NO_x, and O_3 and their maxima can be significantly reduced by changing the timing of the emissions of O_3 precursors. It suggests that the air pollution could be reduced by delaying commuting time for 1 or 2 hours, while the daylight saving time could make air pollution problem even worse.

Chapter 5

Dust Aerosol and Its Effect on Photochemistry in the MC area

In this chapter, the dust particles originating from the large dry land northeast of MC are the focus of the simulations. Several model simulations were performed to highlight the effects of dust aerosols on the photolysis rates and chemical compounds in the MC area. Section 5.1 gives a brief description of the *dust module* implemented in the WRF/Chem model (version 3.0), and dust emissions in the MC area. In section 5.2, the simulated aerosol concentrations are compared with the measured values, and contributions of dust aerosols to aerosol total mass, dust effects on photolysis rates and chemical compounds are then discussed.

5.1 Dust module

Dust emission is strongly dependent on surface properties, such as soil composition, vegetation, and soil moisture content, and on surface wind velocity (e.g. Grini *et al.*, 2005). Wind erosion is the driving force of dust particle emissions, and the erosion threshold is based on the size distribution of dust emission once the surface wind

velocity reaches some threshold, which depends on soil characteristics and roughness length (Marticorena and Bergametti, 1995). In the MC region, there are no deserts and the dust erodibility is mainly due to dry lands and irrigated lands (farmlands without vegetation). The dust erodibility thus is estimated by the surface land information provided by US Geographical Service (USGS). Here a soil erosion fraction is used to represent the dust erodibility in one grid cell. The values of soil erosion fraction (grided on 6 km x 6 km model mesh size) are given in Table 5.1, and the spatial distribution is shown in Fig. 5.1. Figure 5.1 shows that the dry lakebed, dry lands and farm lands located at the northeastern of the MC region are the major dust sources. As a result, under north or northeast wind conditions, there are often dust events in the MC area that are transported from the dust source regions. When south or southeast winds prevailed, the small areas of dry lakebed and agricultural lands in vicinity of Mexico City, which is not well represented in USGS data, could play important roles for dust pollution in the MC area (Díaz-Nigenda *et al.*, 2010).

Table 5.1: The soil erosion fraction (E_r) on the 6 km x 6 km model grid cell in MC and the surrounding area

Soil type	Soil erosion fraction (E_r)
Dry cropland and pasture	0.30
Mixed dryland/irrigated cropland & pasture	0.12
Savanna	0.10
Cropland/grassland mosaic	0.05
Cropland/woodland mosaic	0.05
Irrigated cropland and pasture	0.03
Others	0.0

The major processes controlling dust distributions, including dust emission, dust transport, dry deposition (gravitational settling), are adopted from the dust

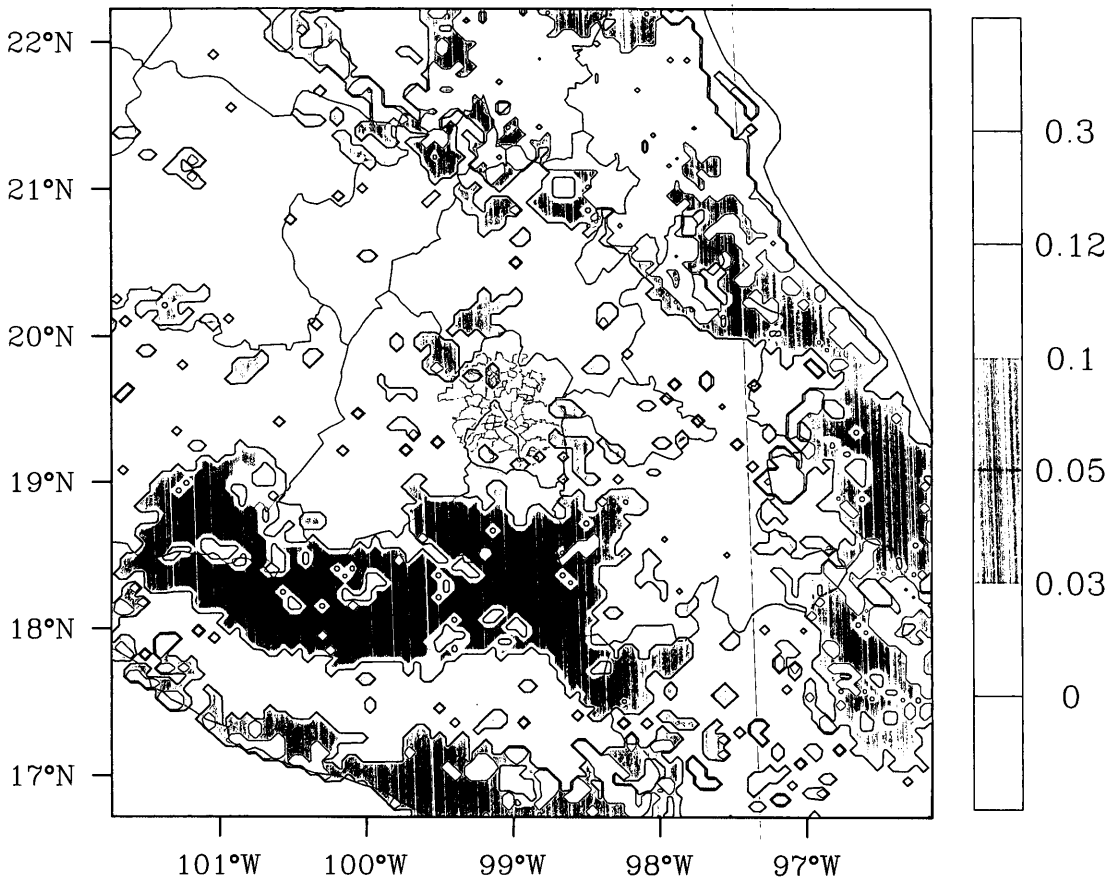

Figure 5.1: Spatial distribution of soil erosion fraction (on the 6 km x 6 km model grid cell) in Mexico City and the surrounding region. White color represents the lack of erosion.

modules developed by the GOCART model (Georgia Tech/Goddard Global Ozone Chemistry Aerosol Radiation and Transport model) (Chin *et al.*, 2000; Ginoux *et al.*, 2001). The dust erodibility is modified to be suitable for the MC region in the WRF/Chem model. The dust particle sizes include 5 size bins, with mean radius of 0.6, 1.2, 2.4, 4.5, and 8.0 μm, respectively. The dust emission of each dust particle size bin is calculated by taking into account the soil particle fraction, soil erosion fraction, surface wind velocity and the threshold velocity of wind erosion. The emission flux F_p ($\mu g m^{-2} s^{-1}$) at particle size bin p is determined by the following expression:

$$F_p = \begin{cases} C\alpha_p E_r {v_s}^2 (v_s - v_t) & v_s > v_t \\ 0 & otherwise \end{cases} \tag{5.1}$$

where C is a dimensional factor ($C = 0.8\ \mu g s^2 m^{-5}$), α_p is the soil particle fraction at particle size bin p (see Table 5.2 for details), E_r is the probability soil erosion fraction which discussed in Table 5.1 and Fig. 5.1, v_s is wind velocity at 10 m, and v_t is the threshold velocity of wind erosion. The threshold velocity is determined as a function of particle size and density, and soil moisture:

$$v_t = \begin{cases} v_{t0}(1.2 + 0.2 log_{10} w) & w < 0.5 \\ 100 & otherwise \end{cases} \tag{5.2}$$

here v_{t0} depends on the soil particle size and density:

$$v_{t0} = 0.0013 \sqrt{\frac{\rho_p g d_p}{\rho_a}} \frac{\sqrt{1 + 0.006/(\rho_p g {d_p}^{2.5})}}{\sqrt{1.928(1331.0 {d_p}^{1.56} + 0.38)^{0.092} - 1.0}} \tag{5.3}$$

where d_p is the particle diameter, g is the acceleration of gravity, ρ_p and ρ_a are the particle and air density, respectively. w is the soil wetness (0.001-1.0), $w = s_m / s_{m0}$, s_m is the soil moisture, and s_{m0} is the saturated value of soil moisture. The typical

values of w in arid surface are between 0.001 and 0.1, but higher than 0.5 after precipitation.

Table 5.2: Properties of five dust particle size bins

Type	Mean effective radius μm	Particle density (ρ_p) gcm^{-3}	Particle fraction (α_p)
Bin 1	0.6	2.50	0.10
Bin 2	1.2	2.65	0.25
Bin 3	2.4	2.65	0.25
Bin 4	4.5	2.65	0.25
Bin 5	8.0	2.65	0.25

After the dust particles are emitted under favorable meteorological conditions (dry and windy days), the particles are transported by wind and turbulent motions. The dust particles are eventually deposited (gravitational settling) on the surface. The setting velocity v_{stk} for a particle of radius r is determined using the *Stokes law*:

$$v_{stk} = \frac{2}{9}\frac{\rho_p g}{\mu} r^2 C_{cun} \tag{5.4}$$

where ρ_p is the particle density, g is the acceleration of gravity, and μ is the absolute viscosity of the air ($1.5 \times 10^{-5} kgm^{-1}s^{-1}$), and C_{cun} is the Cunningham correction which takes into account the viscosity dependency on air pressure and temperature.

Because the gravitational settling velocity is strongly dependent on the size of particles, large dust particles are deposited with relative short distance of downwind of source region, while small particles can be transported a long distance (up to several thousand kilometers) before they are deposited (mostly by rainout and washout) at the surface. The detailed descriptions of these processes are given by Ginoux *et al.*, (2001).

5.2 Simulation results

In order to investigate the dust and its impact on the photochemistry (especially the rate of photolysis) and the chemical compounds in the MC region, three sets of simulations were conducted, including (1) a control simulation with only gas-phase chemistry, excluding the effects of aerosol particles (*Gas-Run*), (2) a simulation with gas-phase chemistry and the effect of anthropogenic aerosols on photolysis, but excluding the effect of dust particles (*Aero-Run*), and (3) a simulation with gas-phase chemistry and aerosols, including dust and the effect on photolysis (*Dust-Run*). The difference between *Gas-Run* and *Aero-Run* represents the impact of anthropogenic aerosols on photochemistry, and the difference between *Aero-Run* and *Dust-Run* indicates the impact of dust aerosols on photochemistry.

5.2.1 Anthropogenic and dust aerosols

The simulations of aerosol mass concentrations and distributions (both anthropogenic and dust aerosols) are evaluated by comparing the simulation with the measured aerosol values. In the MC area, there are 8 monitoring sites for measuring $PM_{2.5}$ and 16 monitoring sites for measuring PM_{10} in the RAMA network (see Fig. 2.5 and Table 2.4 for details). Among these sites, only three (TLA, SAG and MER) measure both $PM_{2.5}$ and PM_{10} aerosol concentrations. In addition to the RAMA sites, there is also a super monitoring site T0 which located inside of Mexico City (also see Fig. 2.5) during MILAGRO experiment (http://mce2.org/fc06/fc06.html), with more detailed measurements, such as aerosol composition and photolysis rate coefficients. These comprehensive measurements enable study of the effects of aerosol particles on photochemistry.

The size of anthropogenic aerosol particles is normally less than 2.5 μm. The large particles (radius > 2.5 μm) are mainly attributed to dust and sea-salt particles.

In the MC region sea-salt particle concentrations are normally very small, and the remaining large particles are mainly attributed to dust particles (Chow *et al.*, 2002). $PM_{2.5}$ particles mainly consist of anthropogenic aerosols and smaller size of dust particles (size bins 1, 2 and 3). The difference between PM_{10} and $PM_{2.5}$ mainly consist of larger dust particles in size bin 4 and 5.

Figure 5.2 shows the simulated and measured daily-mean (averaged over 24 hours from 08:00 AM to 08:00 AM the next day) surface $PM_{2.5}$ aerosol mass concentrations, at the super site T0 (Mugica *et al.*, 2008) and averaged over all RAMA sites. if dust particles are excluded from the simulation (*Aero-Run*), the calculated $PM_{2.5}$ aerosol mass concentrations (gray bars) are significantly underestimated, about 50% lower than the measured values (black bars). At the site of T0, the simulated $PM_{2.5}$ mass concentrations range from 11 to 30 $\mu g/m^3$, while the measured values are between 33 and 70 $\mu g/m^3$. This result clearly indicates that there are significant amount of aerosol mass missed in the simulations, when dust particles are not included in the model.

As described above, anthropogenic aerosols are major contributors to $PM_{2.5}$ aerosols, especially carbonaceous aerosols in the MC area. The largest fine-particle components were carbonaceous aerosols, constituting ~50% of $PM_{2.5}$ mass (Querol *et al.*, 2008; Mugica *et al.*, 2009). Comparing calculated carbonaceous aerosols to measured values can give some insight for the missing aerosol sources. Figure 5.3 shows the simulated and measured daily-mean (06:00 AM - 06:00 AM) carbonaceous aerosol mass concentrations at the city site of T0 during MILAGRO experiment. The result shows no big over- or under-estimate by the simulations for the aerosol mass concentrations of organic and elemental carbon. The 5-day averaged aerosol mass concentrations for simulated and measured OC are 6.7 and 8.9 $\mu g/m^3$ (underestimated by 2.2 $\mu g/m^3$) and for EC are 2.3 and 2.8 $\mu g/m^3$ (underestimated by 0.5 $\mu g/m^3$), respectively. It notes that the calculation of SOA (secondary organic

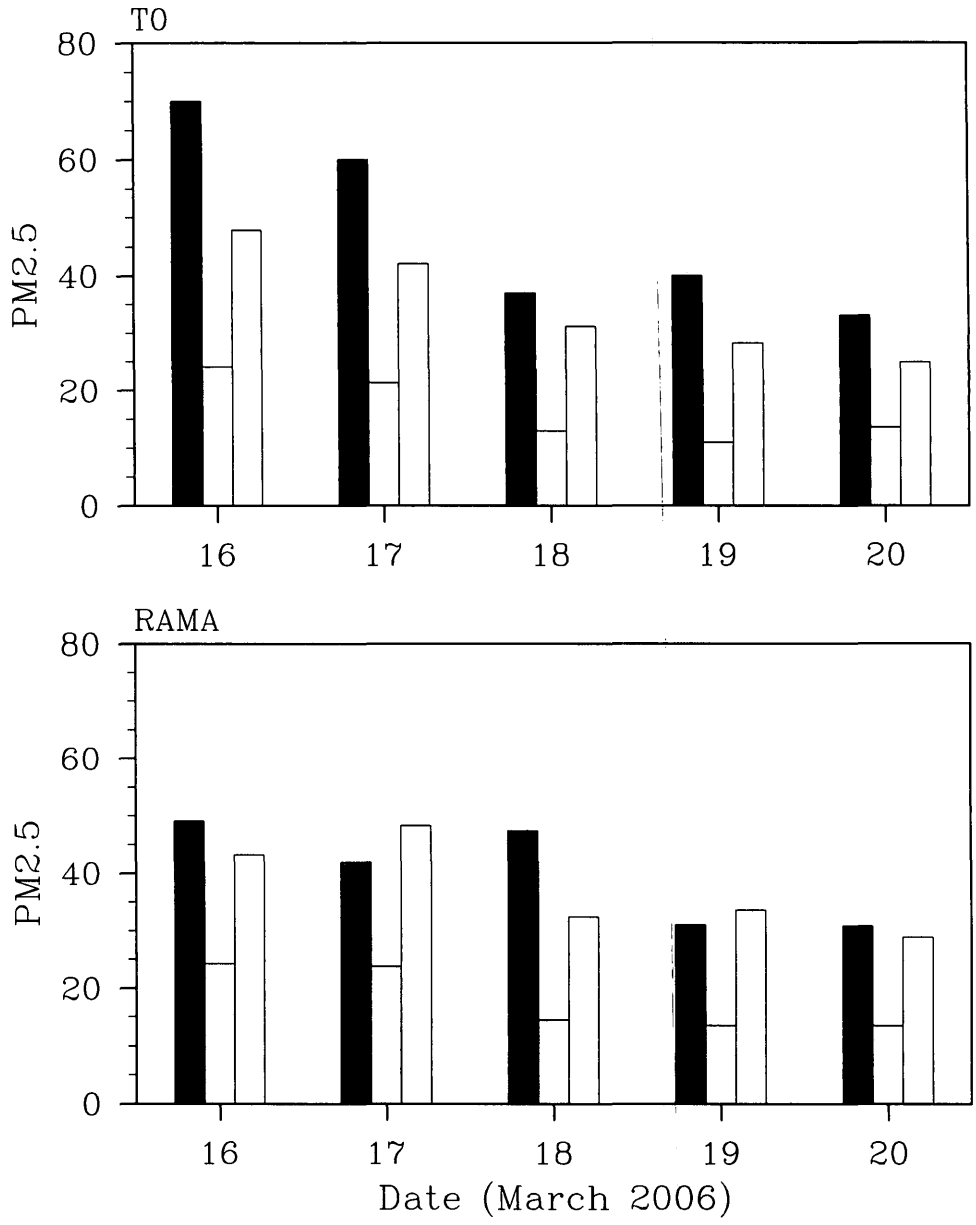

Figure 5.2: Daily-mean $PM_{2.5}$ aerosol mass concentrations ($\mu g/m^3$) at T0 site (Upper) and averaged over all RAMA sites (Bottom), from March 16 to 20, 2006. Black bars represent the measurements, gray bars represent simulations without dust, and white bars represent simulations with dust.

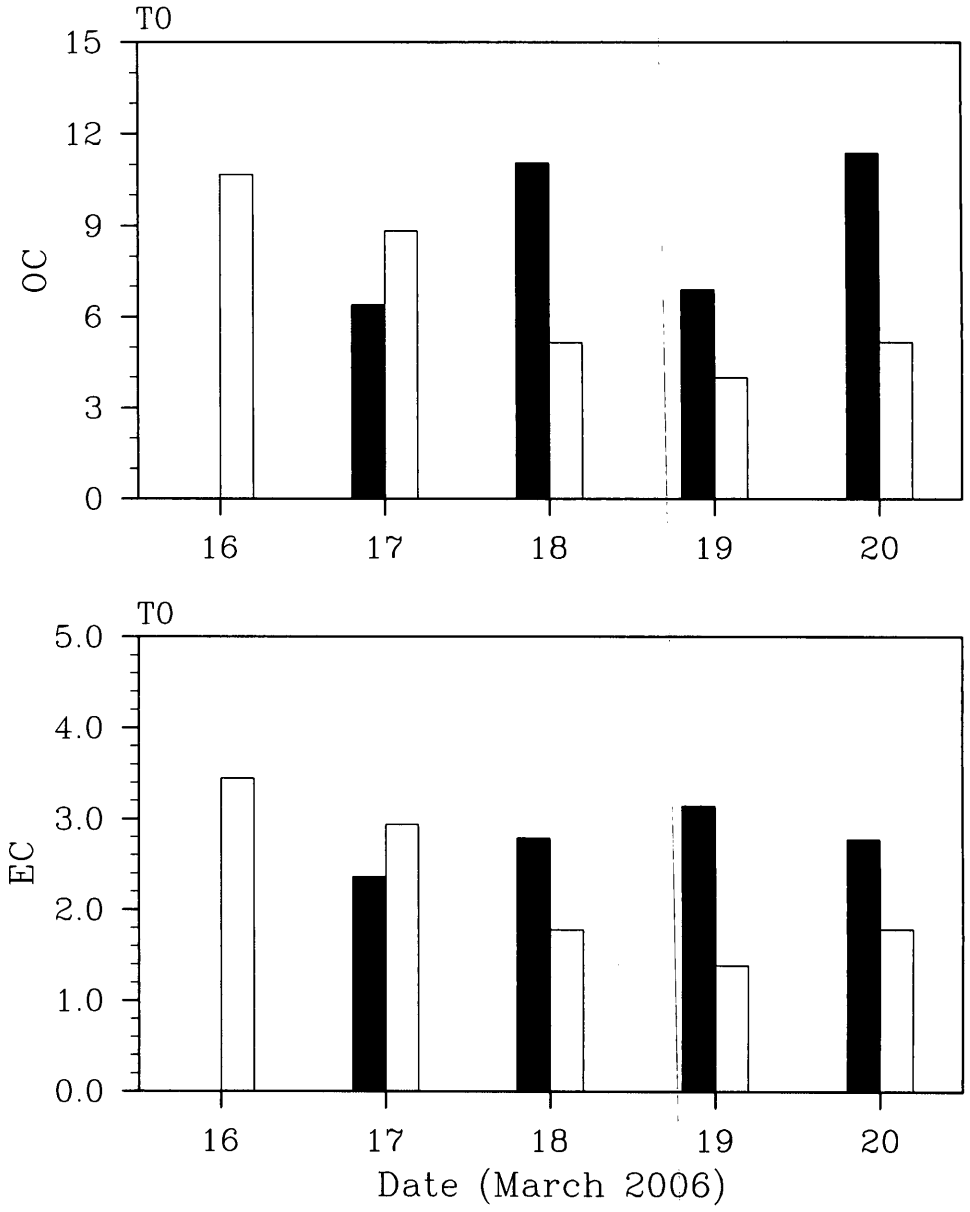

Figure 5.3: Daily-mean organic carbon (OC) and elemental carbon (EC) aerosol mass concentrations ($\mu g/m^3$) at MILAGRO monitoring site T0 from March 16 to 20, 2006. Black bars represent the measurements, red bars represent simulations.

aerosol) exhibits a large uncertainty in current models (less than 1 $\mu g/m^3$ was produced in WRF/Chem) (Fast *et al.*, 2009), and thus the concentrations of $PM_{2.5}$ are generally underestimated in the model simulations. The mean SOA mass is 7.5 $\mu g/m^3$ at the city site (T0) during MILAGRO experiments (Hodzic *et al.*, 2009). The larger underestimate of aerosol mass (22-40 $\mu g/m^3$) with the *Aero-Run* during the period of March 16–20, 2006 cannot only be explained by missing anthropogenic aerosol sources and the underestimation of SOA in the model, and is likely due to the lack of dust aerosol mass in the model.

Figure 5.4 shows the simulated and measured daily-mean (08:00 AM - 08:00 AM) surface PM_{10} aerosol mass concentrations at the site T0 and averaged over all RAMA sites. Similar to $PM_{2.5}$, the simulated PM_{10} (*Aero-Run*) aerosol mass concentrations are significantly underestimated in the MC area. The 5-day averaged aerosol mass concentrations for simulated and measured PM_{10} at the T0 site are 20 and 87 $\mu g/m^3$, respectively. Because PM_{10} contains more dust aerosol mass than $PM_{2.5}$, the larger underestimation of PM_{10} ($\sim$70%) than $PM_{2.5}$ ($\sim$50%) shows convincingly that the missing aerosols in the *Aero-Run* are attributed to the lack of dust particles.

The daily-mean $PM_{2.5}$ and PM_{10} aerosol mass concentrations with dust particles (*Dust-Run*) are also shown in Fig. 5.2 and Fig. 5.4. By including dust aerosol particles in the model, both $PM_{2.5}$ and PM_{10} simulations are significantly improved. With dust particles included in the model, at the site of T0, for example, the 5-day averaged aerosol mass concentration for simulated $PM_{2.5}$ is increased from 17 to 35 $\mu g/m^3$, slightly lower than the measured value of 48 $\mu g/m^3$. The simulated aerosol mass concentrations of PM_{10} with dust aerosol are close to their measured values on March 16 and 20, but higher than the measured values on the other days. Comparing the simulations of the *Dust-Run* (white bars) with the *Aero-Run* (gray

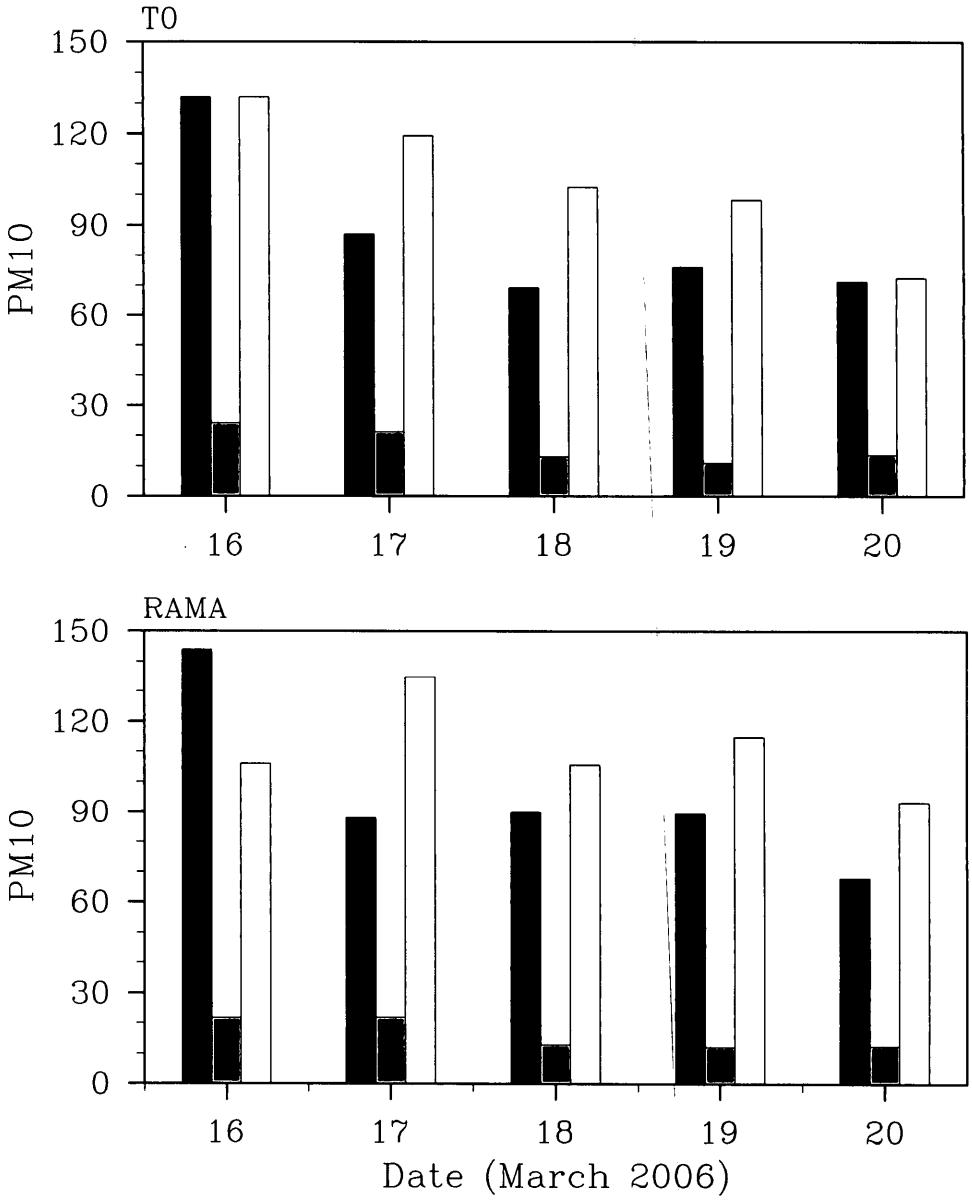

Figure 5.4: Daily-mean PM_{10} aerosol mass concentrations ($\mu g/m^3$), at site of T0 (Upper) and averaged over all RAMA sites (Bottom), from March 16 to 20, 2006. Black bars represent the measurements, gray bars represent simulations without dust, and white bars represent simulations with dust.

bars), the mass of dust particles accounts for about 50% and 70% of the total aerosol mass for $PM_{2.5}$ and PM_{10}, respectively. This simulation suggests that during 'dust days' in the MC area, dust particles contribute a large portion of aerosol mass to the total aerosol mass, and must be taken into account for aerosol simulations. Although the simulations of the *Dust-Run* overestimated the contribution of soil dust comparing with the observation results that soil dust accounted for 15% and 26% of $PM_{2.5}$ and PM_{10} (Querol *et al.*, 2008).

5.2.2 Distribution of dust

Because the highest dust emission sources are located northeast of the MC area (shown in Fig. 5.1), with strong surface wind speeds (inexcess of 5 m/s, see Fig. 5.5), large dust mass concentrations were produced in the source regions during the period of March 16-20, 2006. Figure 5.5 shows the spatial distributions of PM_{10} concentrations simulated with the dust module (*Dust-Run*) on March 16. The simulated PM_{10} has largest mass concentration in this coastal region, and the maximum concentration reaches 500 - 700 $\mu g/m^3$ (about 7 times higher than the PM_{10} mass concentration in the MC area). The winds are generally easterly in the dust source region, and turn to northeasterly near MC. As a result, high dust concentrations appear in the MC region, especially in the northeast area of the city. In the high plains north of MC, the PM_{10} concentrations range from 50 to 200 $\mu g/m^3$. As shown above, the 'dust days' in the MC area appears when the following two conditions occur: (1) higher surface winds in the coastal dust source region northeast of MC; (2) northeast winds from the source region toward to the MC area. Those conditions generally have strong variability, resulting in large daily variations of dust distributions in the MC area.

The above model results indicate that the origin of dust is mainly located about 200 km northeast of Mexico City, where a large area of barren land is an important

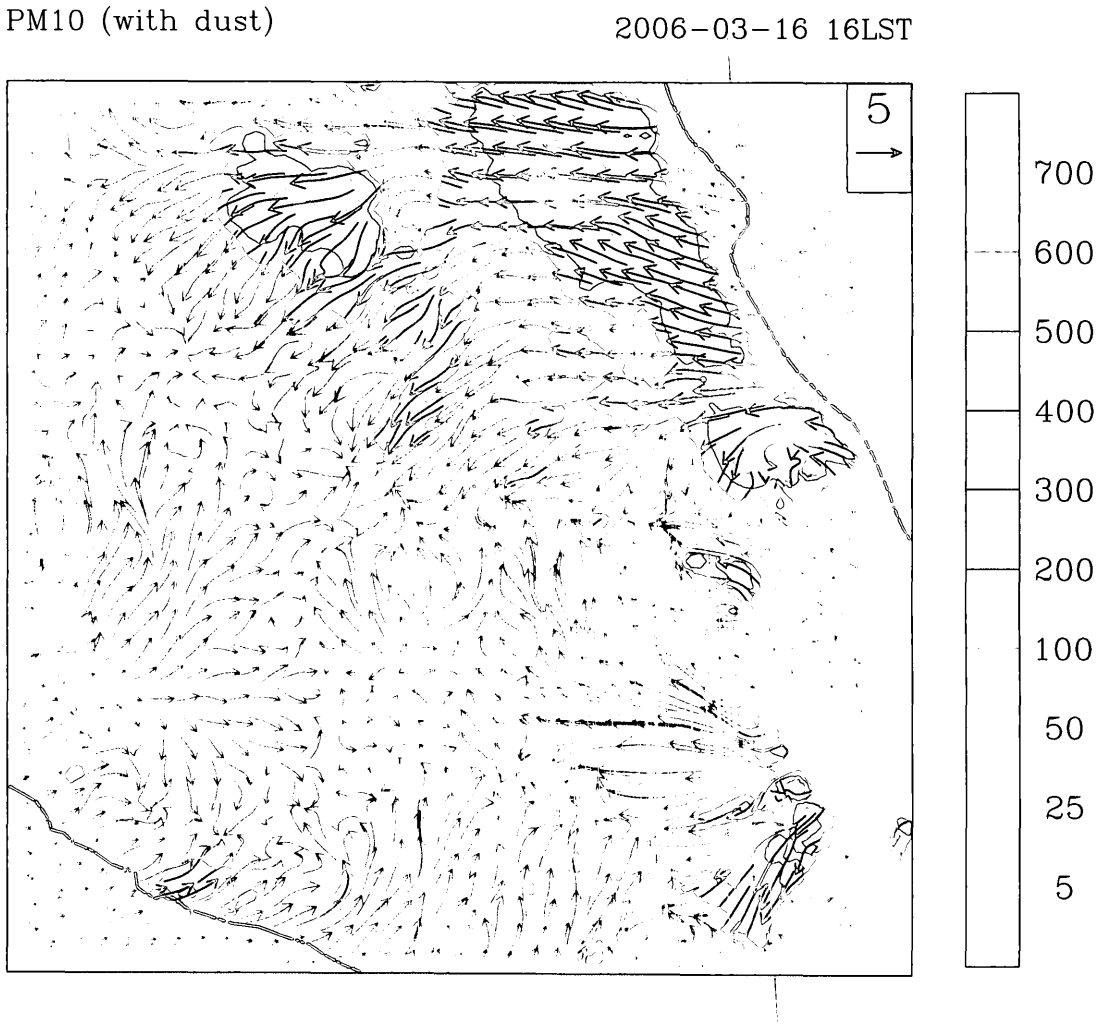

Figure 5.5: The spatial distributions of surface PM_{10} aerosol mass concentrations ($\mu g/m^3$), simulated with dust module, at 4 PM, March 16, 2006.

source of dust (see Fig. 5.1). In order to verify this result, Fig. 5.6 shows the measured absorbing Aerosol Optical Depth (AOD) in the Mexico City region during the period of March 16-20, 2006, from OMI (Ozone Monitoring Instrument) on NASA's Aura satellite. The satellite observations show that the measured absorbing AOD was highly elevated in the dust source region as indicated in the model result. The values of absorbing AOD ranged from 0.1 to 0.14 in the dust source region, but were smaller in other regions, including the Mexico City area. Two possible aerosols sources could have resulted in this high absorbing AOD in this region: (1) soil dust storm and (2) large biomass burning (producing soot aerosols), because both dust and soot particles absorb radiation. From satellite measurements of fire distributions (not shown), there is no evidence of strong fire activity in the high absorbing AOD region during this period, which suggest that the high absorbing AODs are mainly attributed to dust particles in this region.

Figure 5.7 shows wavelength dependence of scattering of aerosols observed with a nephelometer aboard the C-130 aircraft on March 18, 2006 (Shinozuka *et al.*, 2009). Wavelength dependence of scattering is calculated by Angstrom's empirical expression as $\sigma(\lambda) = c\lambda^{-\alpha}$, where σ is the aerosol light scattering coefficient, the factor c is related to the aerosol concentration, and λ is the wavelength (nm) of light; Angstrom's coefficient (α) is also called Wavelength dependence of scattering here. The aerosol light scattering coefficient $\sigma(\lambda)$ was measured at three wavelengths (λ = 450, 550 and 700 nm) in this experiment (see the website http://www-air.larc.nasa.gov/cgi-bin/arcstat-b). Here we use wavelengths of 450 and 550 nm for the calculations ($\alpha = -\frac{\ln(\sigma_{\lambda_1}/\sigma_{\lambda_2})}{\ln(\lambda_1/\lambda_2)}$). According to the studies by Kaufinan *et al.* (1994) and Shinozuka *et al.* (2009), the typical value of α for dust particle ranges from 0.0 to 1.0. In this study, a value of 0.5 is used to distinguish small urban-type particles from large soil-derived particles. The values of calculated α (see Fig. 5.7) ranged from -5 to 10, the lower values (less than 0.5) are result from dust (blue dots), and bigger values (great

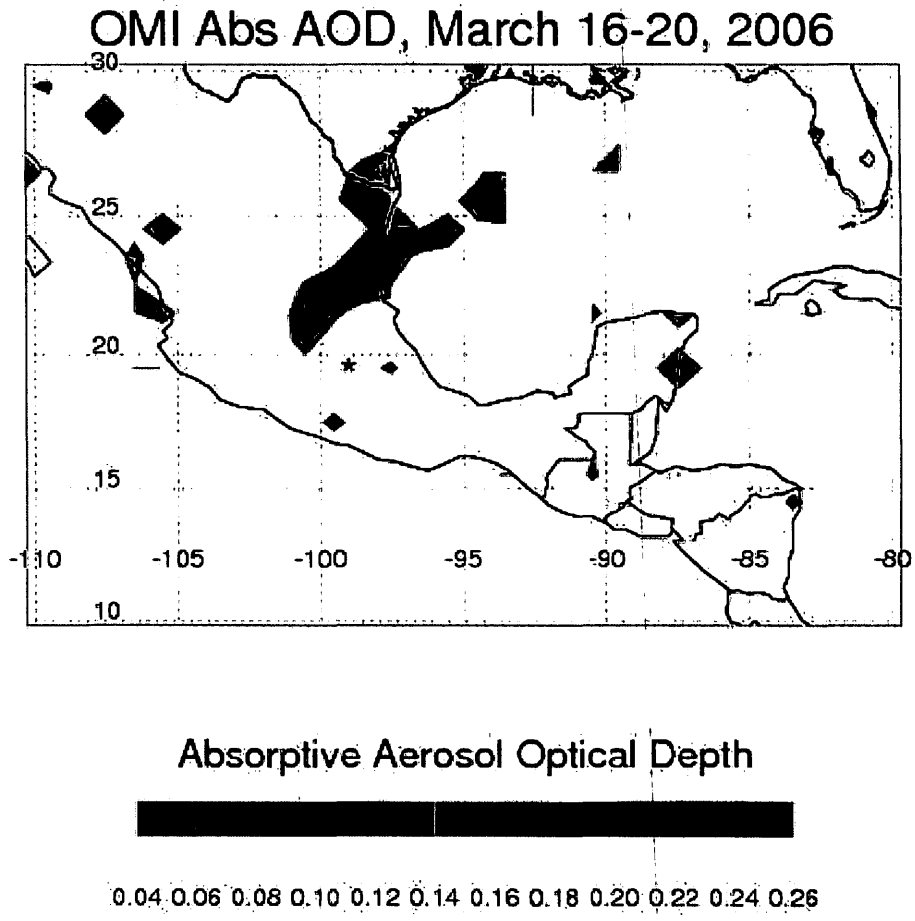

Figure 5.6: Measured absorbing Aerosol Optical Depth (AOD) by OMI satellite in the Mexico City region during the period of March 16-20, 2006. * is the location of MC (plot by S. Massie, private communication, 2009).

than 0.5) are from pollution (red dots). There are several α peaks from dust during this 8.5 hour flight. The flight route on March 18 is shown in Fig. 5.8, in which the line colors represent the values of the observed wavelength dependence of scattering: below 0.5 are shown in blue, and over 0.5 are shown in red. There are two dust areas (blue lines), one in the north (around 12 and 14 PM), the other east (about 17 PM) of MC at a flight height of 2 - 4 km from the surface. This flight observation is consistent with the model result (also shown in Fig. 5.8) that the major dust source is located north and east of the MC area.

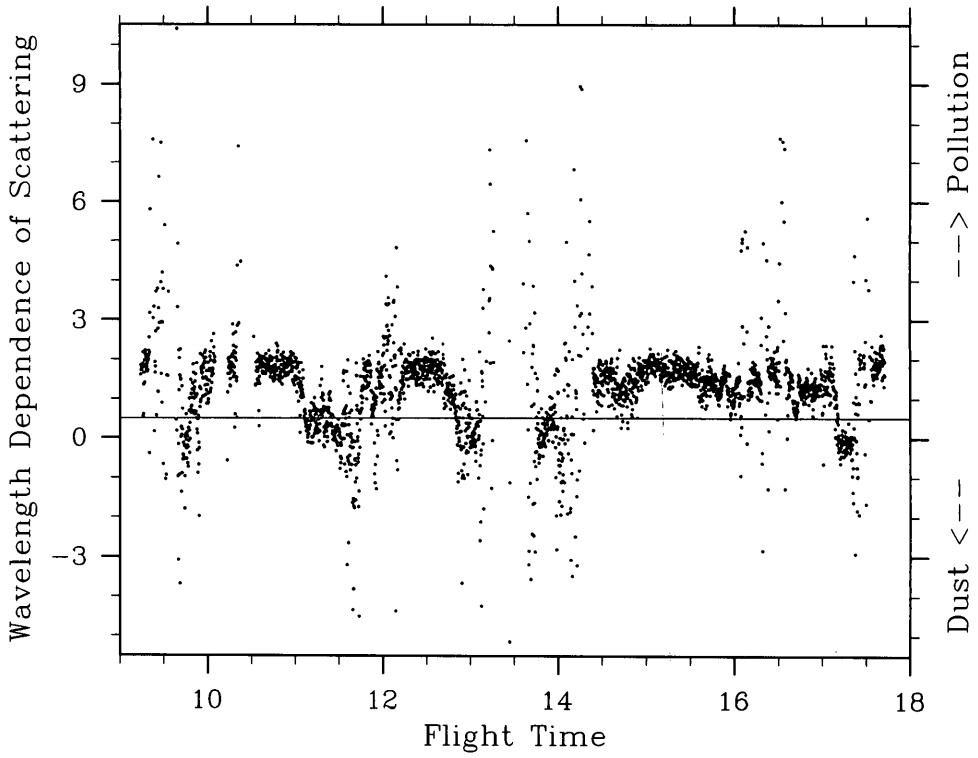

Figure 5.7: Observed wavelength dependence of scattering from C-130 aircraft flight on March 18, 2006 during the MIRAGE-Mex field experiments.

In addition to higher dust mass concentrations, a strong daily variation of aerosol mass was also observed at the surface stations in the Mexico City area during

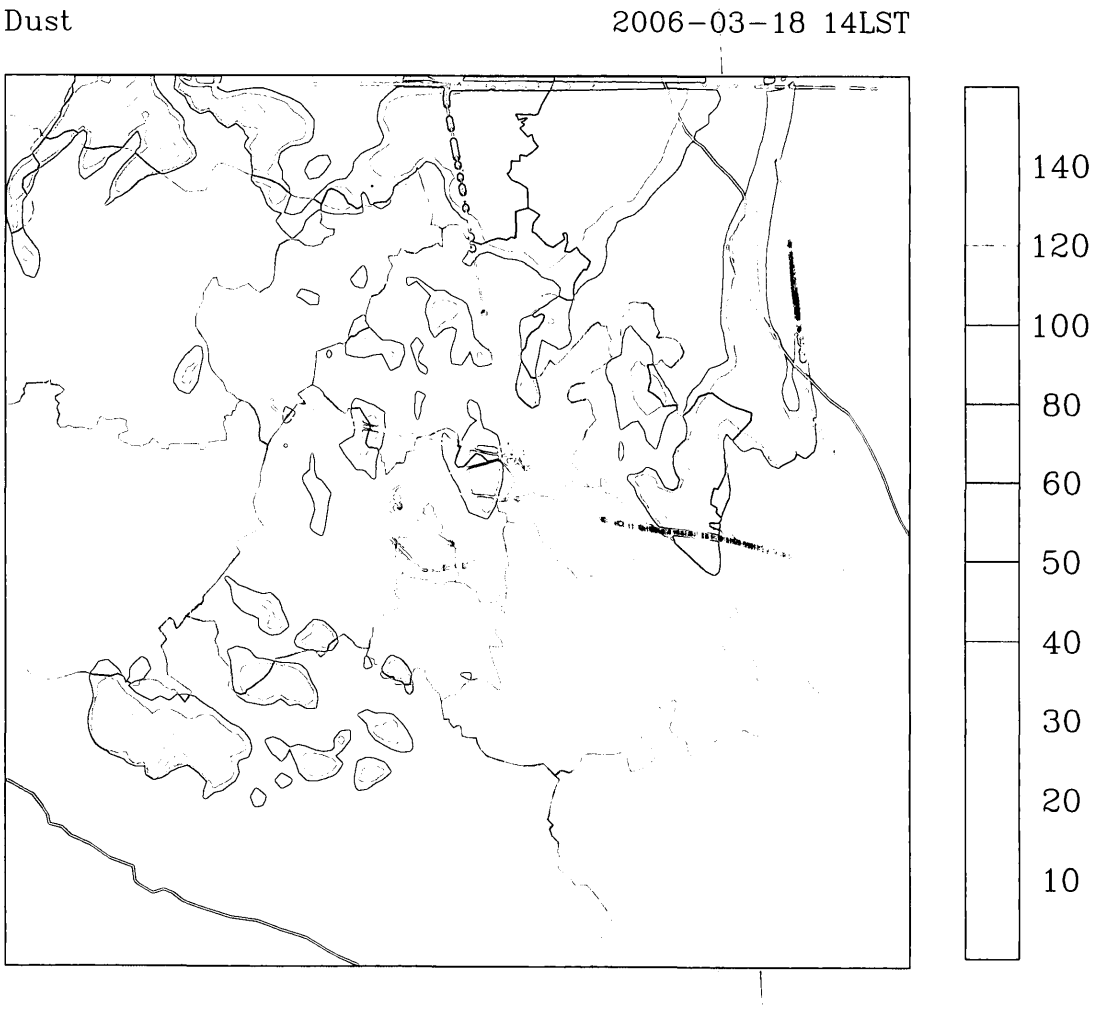

Figure 5.8: The spatial distributions of dust concentrations ($\mu g/m^3$) at an altitude of ~2.5 km, at 2 PM, March 18, 2006. The line represents aircraft flight route on March 18, line colors reflects the intensity of wavelength dependence of scattering (α) (blue: $\alpha < 0.5$, red: $\alpha > 0.5$, gray: data missing).

March 16-20, 2006 (Fig. 5.9). There are several aerosol peaks during this period. The first major peak occurs during the night of March 16-17 and the second major peak during the night of March 17-18. There is also a third peak occurring during the night of March 18-19, especially at the SAG site, which is located northeast of the city. The simulated aerosol mass concentrations without dust particles (red-dash lines) are substantially lower than the measured mass concentrations, especially during these peak times, suggesting that the dust aerosols cause these high aerosol mass peaks. There is also an indication that the diurnal variability is very different between dust and anthropogenic aerosols. For example, the simulated aerosol diurnal variation without dust (red-dash lines) is generally in a regular pattern, with maxima occurring in the morning (9-10 AM). However, the measured diurnal variation of the aerosol concentration appears a relatively random pattern, with maxima generally occurring during evenings. The simulated aerosol concentrations with dust included (green-solid lines) significantly improve the agreement with observations, in terms of both mass concentrations and diurnal variation.

As shown in Fig. 5.9, by including dust aerosols in the model, the simulated aerosol concentrations are significantly enhanced with the peak values of 300-400 $\mu g/m^3$, which are consistent with the measured peak values. The simulated diurnal variation of PM_{10} appears to be more variable than the anthropogenic aerosol and the maxima of aerosol concentrations can occur in the morning, or in the evening.

In spite of the good agreement with observations, there are discrepancies between the simulation and measurement for the aerosol concentrations. For example, the morning peak in March 17 is largely overestimated, and the very large variability of aerosols in the NE site cannot be resolved. These results suggest that although the calculated magnitude of dust aerosol mass are generally consistent with observations, the large variability of dust aerosols, cannot be well simulated in the current model; especially the timing of dust aerosol peak in afternoon, which needs to be further

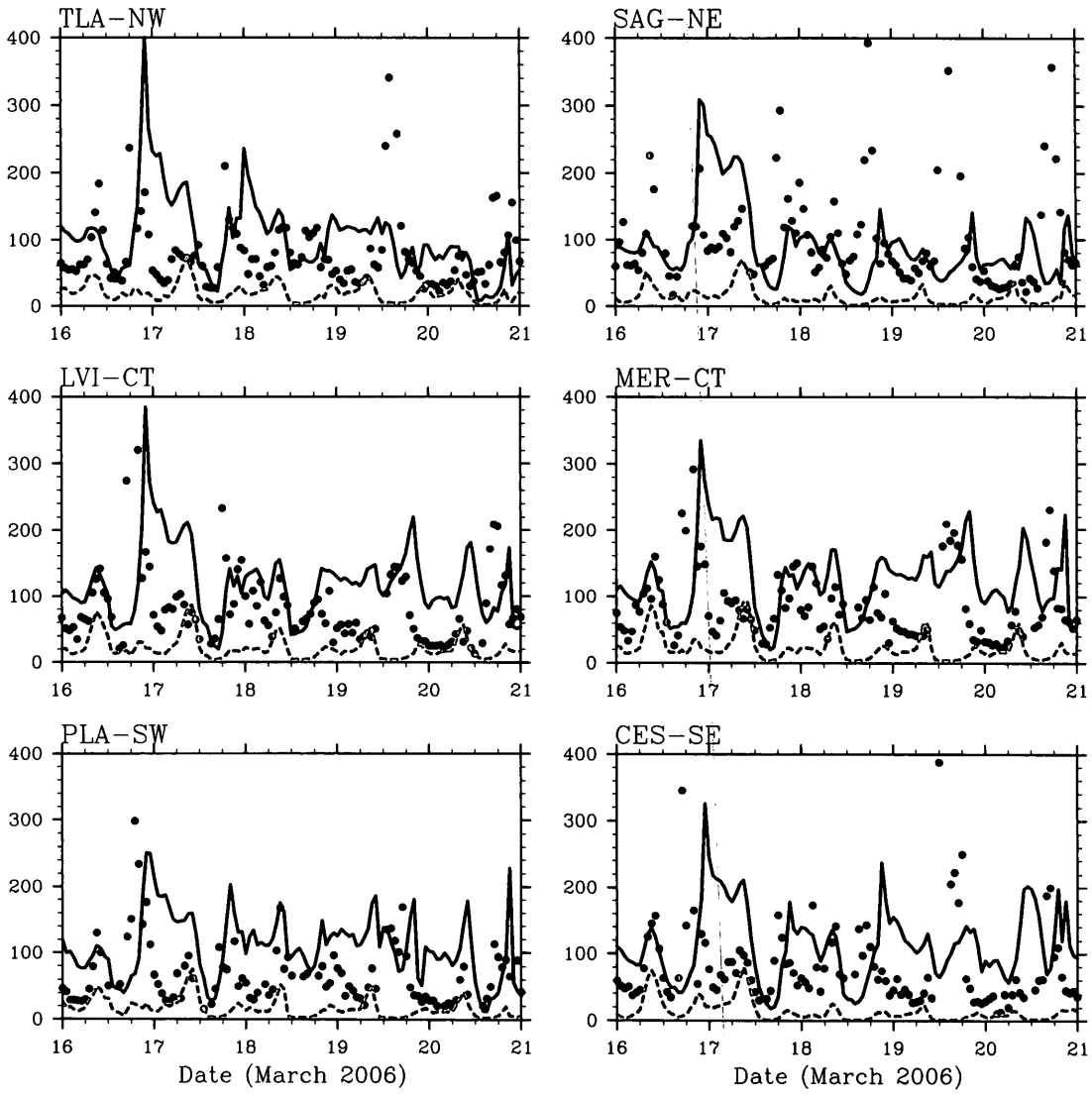

Figure 5.9: Comparison of the measured and simulated PM_{10} aerosol mass concentrations ($\mu g/m^3$) at selected sites, during the period of March 16-20, 2006. Black dots represent the measurements, red dashed lines represent simulations without dust, and green solid lines represent simulations with dust.

improved in the model. This study does not include the local dust sources from the dry lake of Texcoco and agricultural lands to east and southeast of Mexico City which are discussed in Díaz-Nigenda *et al.* (2010). As a result, when the south or south-east winds prevailed in the afternoon of March 19, the dust pollution due to these small local sources are underestimated, and this could be the reason that the model underestimated the afternoon peak in March 19 in the north and east measurement site.

5.2.3 Dust effect on photochemistry

Aerosol particles can have important effects on photochemistry through their effects on photolysis rates of chemical oxidants (e.g. Castro *et al.*, 2001; Martin *et al.*, 2002; Bian *et al.*, 2003). Figure 5.10 shows the photolysis rate coefficients (J-values) for NO_2 (R1.2) and $O(^1D)$ from O_3 (R1.4) measured and simulated at the super monitoring site of T0 (*city site*) on March 16 and 18, 2006. The model calculated photolysis rate for NO_2 (J_{NO_2}) calculation (light black lines) without the effect of aerosols largely overestimates the observed values (black dots). By including the effects of anthropogenic aerosols, the calculated J_{NO_2} (red dashed lines) is reduced by about 10%, and by further including the effects of dust aerosols, J_{NO_2} (green dotted lines) is reduced by about 20%. While the effect of dust aerosols on photolysis rate coefficient for $O(^1D)$ from O_3 ($J_{O(^1D)}$) at the *city site* (T0) is relatively smaller. In the dust source area, the dust effects on J_{NO_2} and $J_{O(^1D)}$ should be bigger than that in the city area. Unfortunately there are no observations for photolysis rate coefficients in the dust source area, Fig. 5.11 shows the model calculated photolysis rate coefficients for NO_2 and $O(^1D)$ from O_3 at one *dust site* on March 16, 2006. The calculated photolysis rate coefficients J_{NO_2} and $J_{O(^1D)}$ are greatly reduced by including the effects of dust aerosols in the model. The effects of dust aerosols on

photolysis rate coefficients J_{NO_2} and $J_{O(^1D)}$ are all large in the dust source area. The results show the importance of the dust particles on photolysis rate coefficients in the dust source and the MC area.

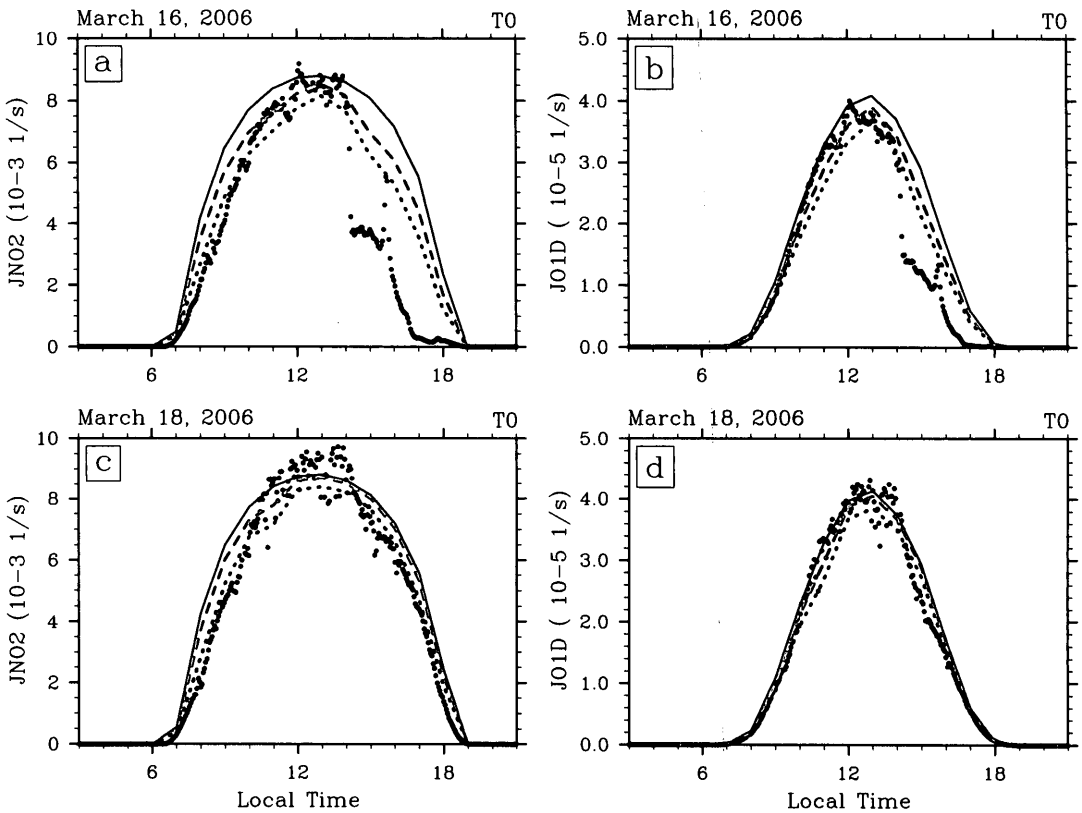

Figure 5.10: Measured and simulated J-values for NO_2 (Left) and $O(^1D)$ from O_3 (Right) at the *city site* (T0) in March 16 and 18, 2006. Black dots represent measured J-values; black solid line represents J-values simulated without aerosols; red dashed lines represent J-values simulated with aerosols, not including dust; and green dotted lines represent J-values simulated with aerosols, including dust.

Compared with the measured J_{NO_2} (Fig. 5.10), the calculated values with both anthropogenic and dust aerosols have been significantly improved, especially during the morning of March 16 and 18. However, the calculated J_{NO_2} is still significantly too large during the afternoon on March 16. The large difference is mainly caused by

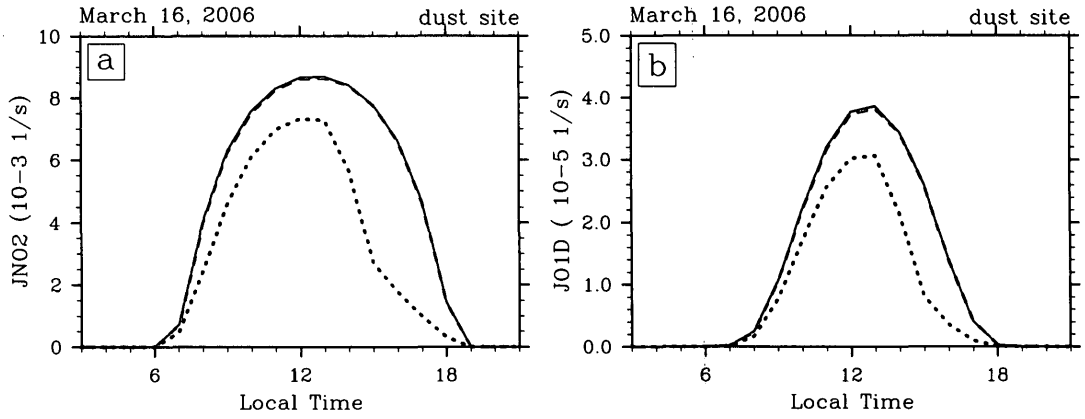

Figure 5.11: Simulated J-values for NO_2 (Left) and $O(^1D)$ from O_3 (Right) at the *dust site* in March 16, 2006. Black solid line represents J-values simulated without aerosols; red dashed lines represent J-values simulated with aerosols, not including dust; and green dotted lines represent J-values simulated with aerosols, including dust.

afternoon clouds, as mostly cloudy conditions were observed at T0 area during the afternoon of March 16, but there were clear skies on March 18 (Fast *et al.* 2007). Another reason could be that the impact of dust aerosols on photolysis rates are underestimated, as the measured aerosol peak occurred around 18 PM as shown in Fig. 5.9 , while the calculated peak occurred around 21 PM, which is about 3 hours later than the measured peak. Because of the strong diurnal variation of sunlight, both the magnitude and diurnal variability of aerosols need to be accurately represented in the model to accurately address the effect of aerosols on photochemistry.

The perturbation of photolysis rates has important impacts on production of hydroxyl radical (OH) and O_3, by reaction of water vapor with $O(^1D)$ (R1.4 - 1.6) and photolysis of NO_2 (R1.11), respectively. The effects of dust aerosols on OH and O_3 concentrations are analyzed by comparing the differences between the two model runs, i.e., Aero-Run and Dust-Run. The result shown in Fig. 5.12 shows that the surface concentration of OH is significantly reduced due to the high concentrations

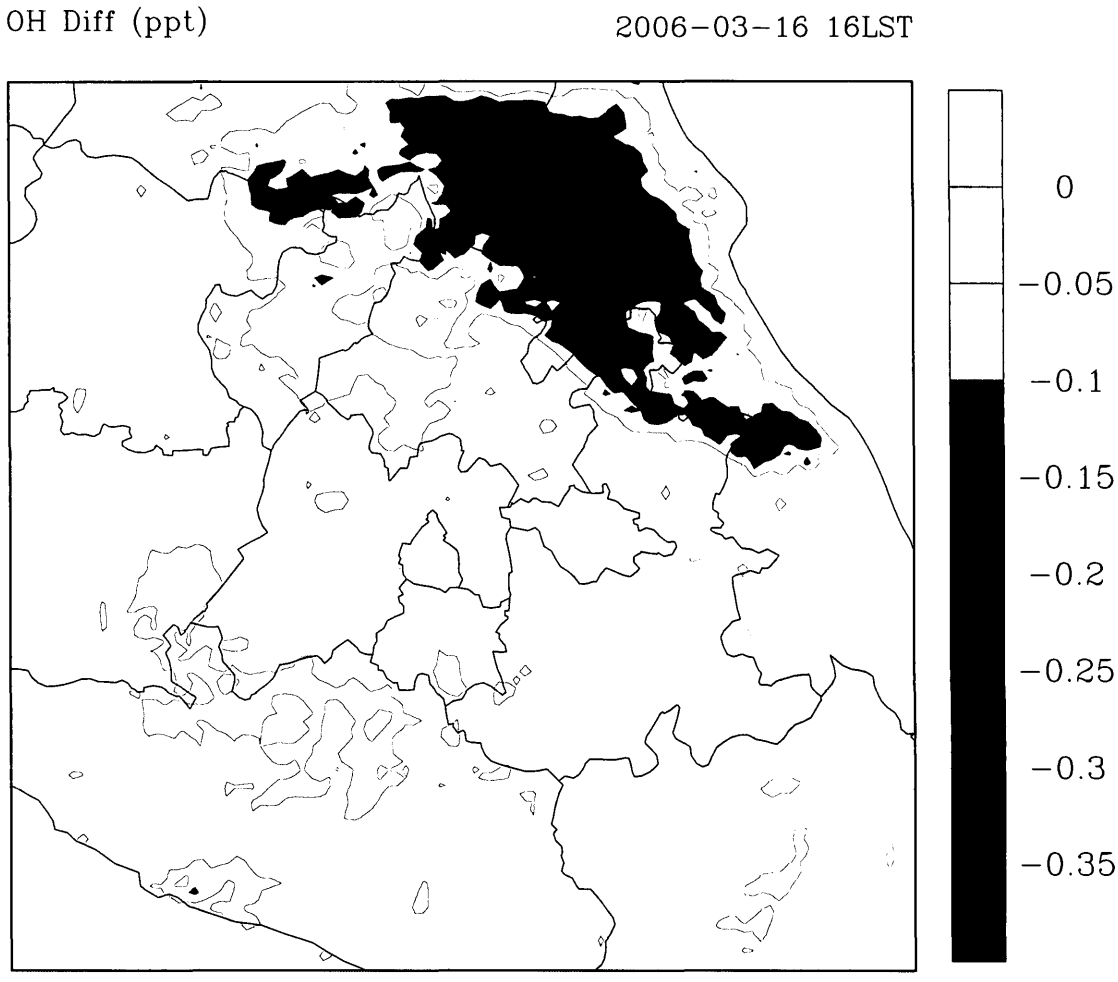

Figure 5.12: calculated perturbation to OH (pptv) at the surface, due to scattering and absorbing by dust at 4 PM, March 16, 2006.

of dust aerosols in the afternoon of March 16, 2006. Because of the short chemical lifetime of OH, the reduction of OH concentrations by dust aerosols is generally correlated with the spatial distribution of dust aerosols, and the maximum reduction of about 0.3 pptv (50%) occurs in the dust source region (northeast of MC). But this large reduction decreases quickly with increasing height, and is close to zero at a height of 5 km (see Fig. 5.13) with little concentration of OH and dust. Near the city area, the reduction of OH concentrations (5 to 20 %) is smaller than the dust source region, due to smaller amount of dust aerosols in this area.

The model simulation also suggests that dust aerosols continued to affect O_3 concentrations in the MC area (see Fig. 5.14), especially in Mexico City, where the O_3 reduction reaches a maximum of about 10 ppbv at the surface. However, as height increases, this reduction decreases, and reaches zero around 15 km (see Fig. 5.13). In the dust source region, O_3 concentrations are reduced by about 3 to 5 ppbv. Contrary to the reduction of OH concentrations, the maximum O_3 reduction is higher in Mexico City than in the dust source region. The strong reduction near the city is because the chemical production of O_3 is not only proportional to the photolysis rate, but also to the concentrations of ozone precursors (such as NO_x and VOCs). The concentrations of VOCs and NO_x are considerably higher in Mexico City than that in the dust source region, producing higher ozone perturbations in the city area.

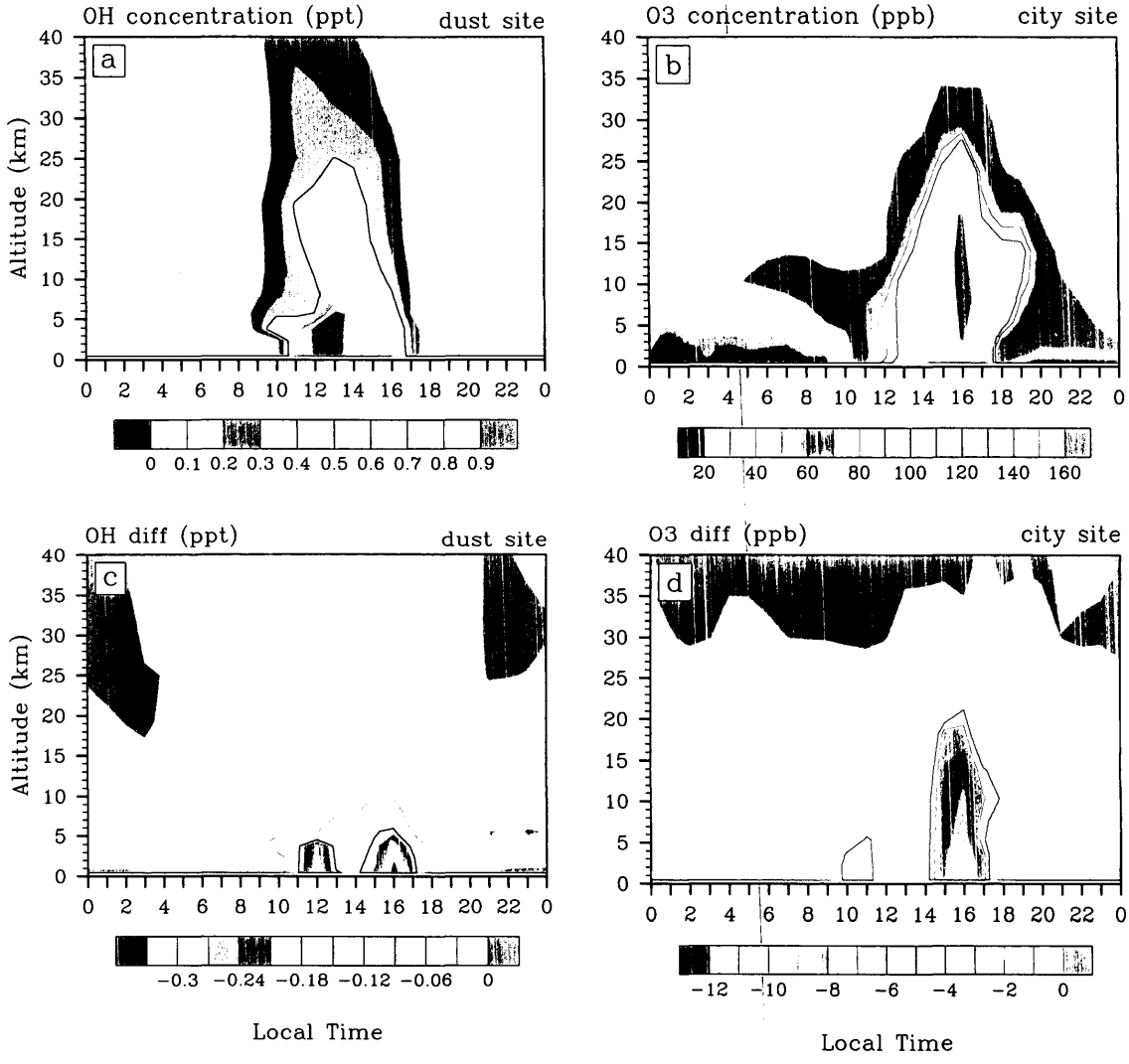

Figure 5.13: The height-time cross-section of OH and O_3 concentrations, and their perturbations caused by dust in the dust site (Left) and city site (right) in March 16, 2006. (a) OH concentration in the dust site; (b) O_3 concentration in the city site; (c) perturbation to OH in the dust site; and (d) perturbation to O_3 in the dust site.

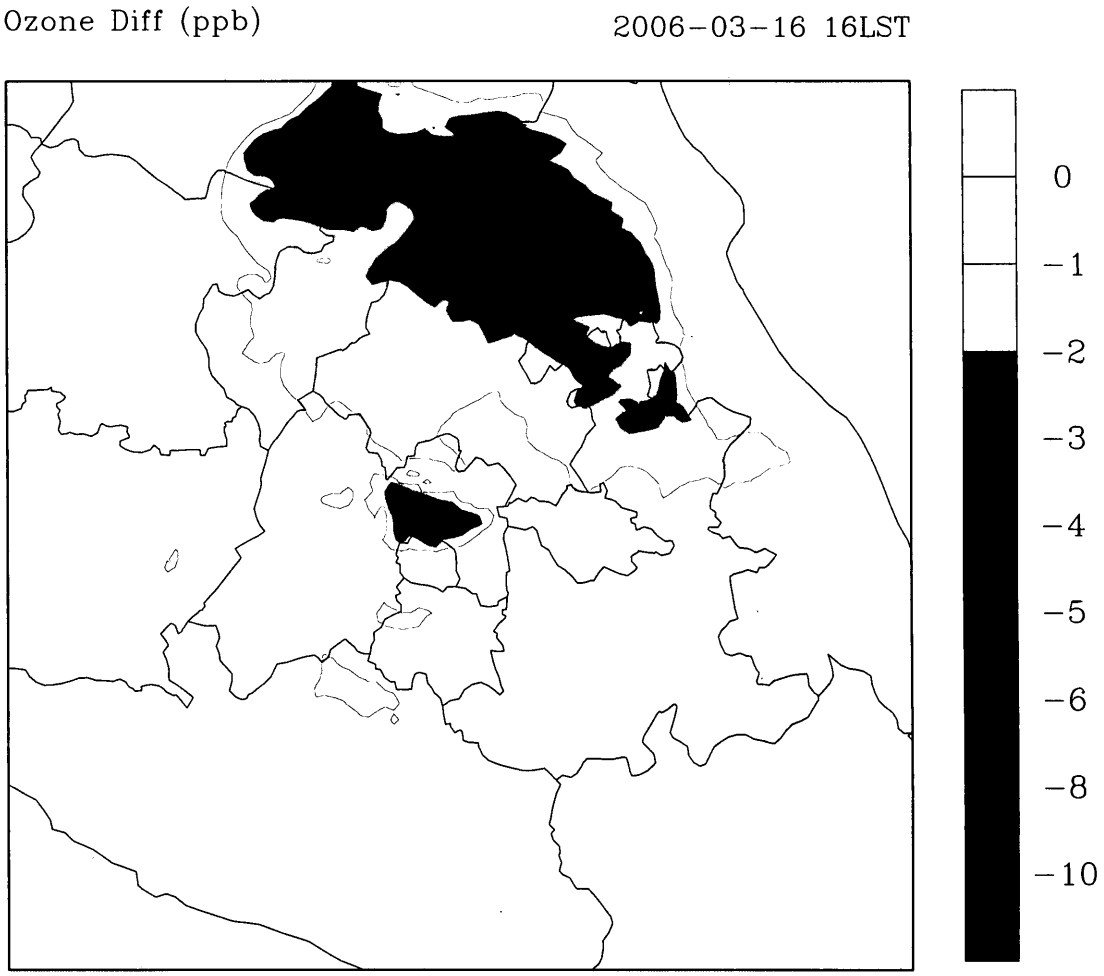

Figure 5.14: calculated perturbation to O_3 (ppbv) at the surface, due to scattering and absorbing by dust at 4 PM, March 16, 2006.

Chapter 6

Summary and Conclusions

The chemical oxidants and dust aerosols in the Mexico city area are studied using the WRF/Chem model. Several simulations are conducted to examine (a) characterization of chemical oxidants and O_3 formation regime; (b) the sensitivity of O_3 to the diurnal variations of the surface emissions; and (c) the effects of dust aerosols on the total aerosol mass and on photochemical production of OH and O_3.

The sensitivity experiments of O_3 to surface NO_x and VOC emissions and chemical indicator analysis using simulated NO_y, O_3/NO_y, $O_3/(NO_y - NO_x)$, and $HCHO/NO_y$ suggest that the chemical O_3 formation is possibly under the VOC-limited regime in the Mexico City area and changes to NO_x-limited in the rural area. According to the calculated OH reactivity from model results, alkenes make the largest contribution to OH reactivity in the emission source area. At the rural area, the OH reactivity and O_3 production are dominated by oxygenated VOCs and CO. The most important VOC in terms of OH reactivity is acetaldehyde at all sites.

The impact of diurnal variations of surface emissions on O_3 concentrations are examined by changing the timing of surface emissions and the following results are obtained from the model simulations: (1) the diurnal variations of air pollutants are strongly influenced by the PBL height evolution; (2) the morning (6 - 11 AM)

emissions determine the afternoon hour O_3 concentrations. The increase in daytime O_3 concentrations and the O_3 maximum is mainly attributable to VOC emissions increase and NO_x emissions decrease in the morning; (3) the emissions of VOCs during other periods (early morning, evening, and night) have little impact on the O_3 concentrations. However, the emissions of NO_x have strong impacts on O_3 concentrations in the evening and the early morning; and (4) shift in timings of emissions can affect air quality. The model simulations suggest that air pollution could be reduced by delaying commuting time for 1 or 2 hours.

During periods when strong winds blow from the northeast, dust contributes substantially to the total aerosol mass and has important effects on concentrations of OH and O_3 in the Mexico City area. The modeling results and observations show that the source of dust is located mainly about 200 km northeast of Mexico City, where a large area of dry barren land plays an important role for the dust events. The simulations of $PM_{2.5}$ and PM_{10} mass concentrations are improved *with a dust module* included in the model. Dust accounted for about 50% of total $PM_{2.5}$ mass, and 70% of total PM_{10} mass during the period of March 16-20, 2006. Dust probably also affects the concentrations of OH and O_3 through its impact on atmospheric photolysis rates. Dust particles reduce the photochemical production of OH, with a maximum reduction of 50% at surface in the dust source area to the northeast of Mexico City. Near the city area, the reduction of surface OH concentrations is about 5 to 20%. The strongest dust effects on O_3 concentrations are near MC, where the maximum reduction of surface O_3 is about 10 ppbv. In the dust source area, simulated surface O_3 concentrations are reduced by about 3 to 5 ppbv.

Giving that the model underestimated the contribution of $HCHO$ to OH reactivity, the emissions of $HCHO$ and ethene may be underestimated and would need to be adjusted in the inventories. Since the dust source of the dry lakebed and agricultural lands in vicinity of Mexico City is not well represented in USGS data,

this small area of dry lands, which can play important roles for dust pollution in the MC area when southeasterly winds prevailed, should be included in future work. Considering the simulation overestimated the contribution of soil dust (compared with the observations obtained during the MILAGRO experiment), the threshold of wind erosion and constraints of causing dust emission may need to be modified, and probably will improve the simulation.

Appendix A

Description of the WRF/Chem Model

The WRF model is a fully compressible and nonhydrostatic model. The model uses terrain-following, hydrostatic-pressure vertical coordinate with top of the model being a constant pressure surface. The horizontal grid is the Arakawa-C grid, and the time-integration scheme in the model uses the third-order Runge-Kutta scheme, and the spatial discretization makes use of 2^{nd} to 6^{th} order scheme. The model supports both idealized and real-data applications with various lateral and top boundary condition options. The model supports one-way, two-way and moving nest options. More information about WRF model can be found on the website *http://www.wrf-model.org.*

The WRF/Chem model is the WRF model coupled with online chemistry. The WRF/Chem model is fully consistent with the WRF model. The model simulates the emission, transport, mixing, and chemical transformation of trace gases and aerosols simultaneously with the meteorology. It uses the same transport schemes for all chemical species, including grid-scale advection and subgrid-scale transport by turbulence and convection. The same vertical and horizontal coordinates are used

(no horizontal or vertical interpolation), the same physics parameterization utilized for subgrid scale transport, and no interpolation in time is performed.

A.1 The WRF model

A.1.1 The model equations

The WRF model equations are written in the flux-form.The equations are formulated using a terrain-following hydrostatic-pressure vertical coordinate denoted by η and defined as

$$\eta = (p_{dh} - p_{dht})/\mu_d \tag{A.1}$$

where $\mu_d = p_{dhs} - p_{dht}$ represents the mass of the dry air in the column, p_{dhs} and p_{dht} refer to the hydrostatic pressure of the dry atmosphere at the surface and at the top boundary, respectively. The coordinate definition (A.1), proposed by Laprise (1992), is the traditional σ coordinate used in many hydrostatic atmospheric models. η varies monotonically from a value of 1 at the surface to 0 at the upper boundary of the model. The equations are written as

$$\partial_t U + (\nabla \cdot \mathbf{V}u) + \mu\alpha\,\partial_x p + (\alpha/\alpha_d)\,\partial_\eta p\,\partial_x \phi = F_U \tag{A.2}$$

$$\partial_t V + (\nabla \cdot \mathbf{V}v) + \mu\alpha\,\partial_y p + (\alpha/\alpha_d)\,\partial_\eta p\,\partial_y \phi = F_V \tag{A.3}$$

$$\partial_t W + (\nabla \cdot \mathbf{V}w) - g\left[(\alpha/\alpha_d)\,\partial_\eta p - \mu\right] = F_W \tag{A.4}$$

$$\partial_t \Theta + (\nabla \cdot \mathbf{V}\theta) = F_\Theta \tag{A.5}$$

$$\partial_t \mu + (\nabla \cdot \mathbf{V}) = 0 \tag{A.6}$$

$$\partial_t \phi + \mu^{-1}\left[(\mathbf{V} \cdot \nabla\phi) - gW\right] = 0 \tag{A.7}$$

$$\partial_t Q_m + (\nabla \cdot \mathbf{V}q_m) = F_{Q_m} \tag{A.8}$$

where α_d is the inverse density for the dry air (ρ_d), α is the inverse density for the full parcel $\alpha = \alpha_d\,(1 + q_v + q_c + q_r + q_i + ...)^{-1}$, and $q_m = q_v, q_c, q_r, q_i, ...$ are the mixing ratios for water vapor, cloud, rain, ice, etc.. Here $\mathbf{V} = \mu_d\,\mathbf{v}$, $\Omega = \mu_d\,\dot{\eta}$, $\Theta = \mu_d\,\theta$, and $Q_m = \mu_d\,q_m$. The right-hand-side terms F_U, F_V, F_W, F_Θ and F_{Q_m} are the forcing terms arising from model physics, turbulent mixing, spherical projections, and the earth's rotation. The diagnostic equation for dry inverse density is

$$\partial_\eta \phi = -\alpha_d\,\mu \tag{A.9}$$

and the diagnostic equation for full pressure (vapor + dry air) is

$$p = p_0\,(R_d\,\theta_m / p_0\,\alpha_d)^\gamma \tag{A.10}$$

where $\gamma = c_p/c_v = 1.4$ is the ratio of the heat capacities for dry air, and p_0 is a reference pressure (typically 10^5 Pascals). $\theta_m = \theta\,(1 + (R_v/R_d)\,q_v) \approx \theta\,(1 + 1.61\,q_v)$.

A.1.2 Discretizations

Spatial discretization

The horizonal and vertical representation of the discrete fields is done on a C-grid staggered for the variables as shown in Fig. A.1 and Fig. A.2, which the locations where u, v, w and m are defined as u points (i+1/2, j, k), v points (i, j+1/2, k), w points (i, j, k+1/2) and mass points (i, j, k), respectively. m represents θ, the column mass μ and q_m, the diagnostic variables, the pressure p and inverse density α are computed at mass points. The geopotential ϕ is defined at the w points. The grid lengths Δx and Δy are constants in the model formulation, The vertical grid length $\Delta\eta$ is not fixed constant, $\Delta\eta_k = \eta_{k+1/2} - \eta_{k-1/2}$ and $\Delta\eta_{k+1/2} = \eta_{k+1} - \eta_k$.

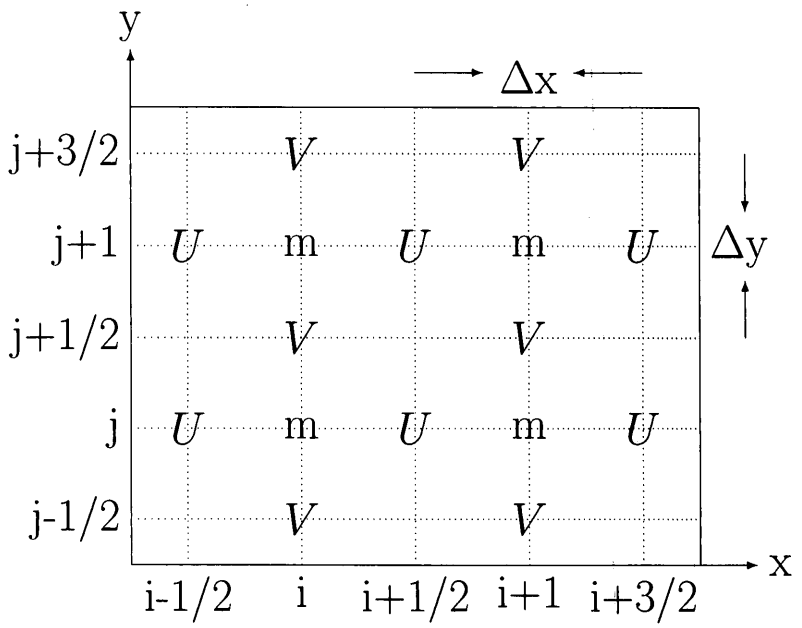

Figure A.1: Staggered horizonal grid and placement of dependent variables.

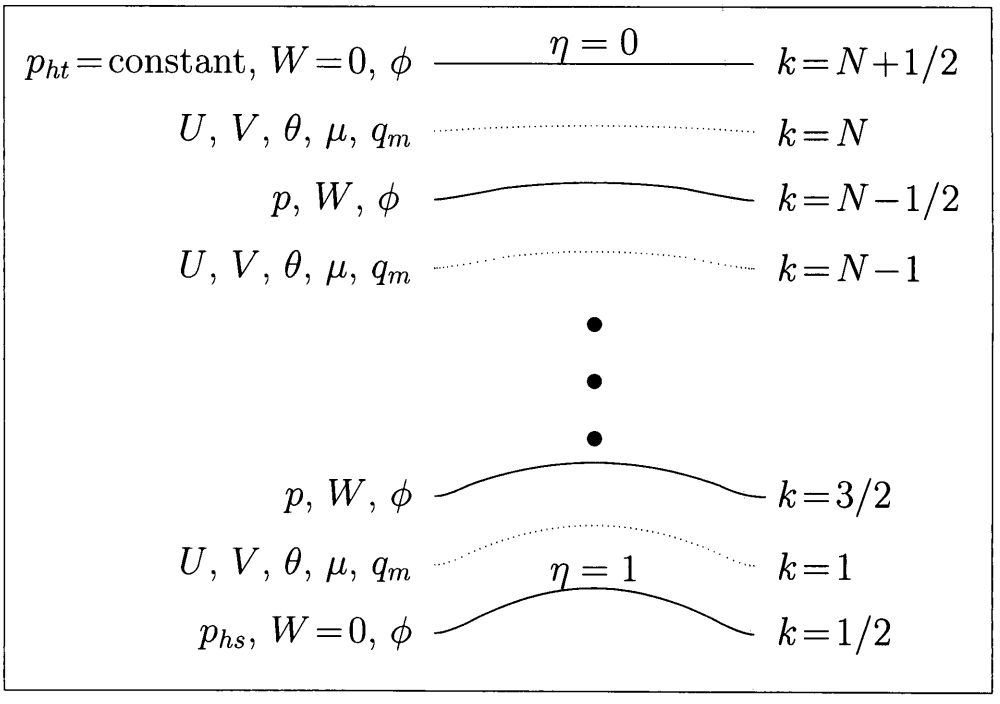

Figure A.2: Staggered vertical grid and placement of dependent variables. N is the number of total vertical levels.

Discretization of advection terms

The advection (flux divergence) terms are discretized using selectable 2^{nd} through 6^{th} order operators. The discrete flux divergence operators can be illustrated by considering the flux divergence operator for a scalar a in its discrete form:

$$\nabla \cdot \mathbf{V}_a = \delta_x \left(U\bar{a}^{x_{adv}}\right) + \delta_y \left(V\bar{a}^{y_{adv}}\right) + \delta_\eta \left(\Omega\bar{a}^{\eta_{adv}}\right)$$

the discrete operator δ_x is defined as

$$\delta_x \left(U\bar{a}^{x_{adv}}\right) = \Delta x^{-1} \left[\left(U\bar{a}^{x_{adv}}\right)_{i+1/2} - \left(U\bar{a}^{x_{adv}}\right)_{i-1/2}\right]$$

The different order advection schemes correspond to different definitions for the operator $\bar{a}^{x_{adv}}$, and the 6^{th} and 5^{th} order operators are

$$\begin{aligned} 6^{th}\text{order:} \quad \left(\bar{a}^{x_{adv}}\right)_{i-1/2} &= \frac{37}{60}(a_i + a_{i-1}) - \frac{2}{15}(a_{i+1} + a_{i-2}) + \frac{1}{60}(a_{i+2} + a_{i-3}) \\ 5^{th}\text{order:} \quad \left(\bar{a}^{x_{adv}}\right)_{i-1/2} &= \left(\bar{a}^{x_{adv}}\right)^{6^{th}}_{i-1/2} \\ &\quad -sign(U)\frac{1}{60}[(a_{i+2} - a_{i-3}) - 5(a_{i+1} - a_{i-2}) + 10(a_i - a_{i-1})] \end{aligned}$$

Temporal discretization: Rung-Kutta time integration scheme

The WRF uses a time-spliting integration scheme, of which the slow or low-frequency modes are integrated using a third-order Runge-Kutta (RK3) time integration scheme, while the high-frequency acoustic modes are integrated over smaller time steps to maintain numerical stability (Wicker and Skamarock *et al.*, 2002). Defining the prognostic variables as $\Phi = (U, V, W, \Theta, \phi', \mu', Q_m)$ and the model equations as $\Phi_t = R(\Phi)$, the RK3 integration takes the form of 3 steps to advance a solution $\Phi(t)$ to $\Phi(t+\Delta t)$:

$$\Phi^* = \Phi^t + \frac{\Delta t}{3} R(\Phi^t) \tag{A.11}$$

$$\Phi^{**} = \Phi^t + \frac{\Delta t}{2} R(\Phi^*) \tag{A.12}$$

$$\Phi^{t+\Delta t} = \Phi^t + \Delta t R(\Phi^{**}) \tag{A.13}$$

where Δt is the time step for the low-frequency modes (the model time step), and the superscripts denote time levels.

Stability Constraints

The Courant-Friedrichs-Lewy condition (CFL condition) is a necessary condition for convergence while solving certain partial differential equations numerically by the method of finite differences. It arises when explicit time-marching schemes are used for the numerical solution. As a consequence, the time step must be less than a certain time in many explicit time-marching computer simulations, otherwise the simulation will produce wildly incorrect results. The condition is named after Richard Courant, Kurt Friedrichs, and Hans Lewy who described it in their papers.

For one-dimensional case, the CFL has the following form:

$$\frac{u \cdot \Delta t}{\Delta x} \leq C \tag{A.14}$$

where u is the velocity (whose dimension, according to dimensional analysis, is L/T), Δt is the time step (whose dimension is T), Δx is the length interval (whose dimension is L), and C is a dimensionless constant which depends only on the particular equation to be solved. The dimensionless number $u \cdot \Delta t / \Delta x$ is called the Courant number.

The RK3 time step is limited by the Courant number and the user's choice of advection schemes - users can choose 2^{nd} through 6^{th} order discretizations for the advection terms. The time-step limitations for 1D advection in the RK3 scheme using these advection schemes is given in Table A.1.

Table A.1: Maximum stable Courant numbers for one-dimensional linear advection (Wicker and Skamarock, 2002)

Time Scheme	Spatial order			
	3^{rd}	4^{th}	5^{th}	6^{th}
Leapfrog	Unstable	0.72	Unstable	0.62
RK2	0.88	Unstable	0.30	Unstable
RK3	1.61	1.26	1.42	1.08

For advection in three spatial dimensions, the maximum stable Courant number is $1/\sqrt{3}$ times the Courant numbers given in Table A.1. For stability, the time step used in the ARW should produce a maximum Courant number less than that given by theory. Thus, for 3D applications, the time step should satisfy the following equation:

$$\Delta t_{max} < \frac{Cr_{theory}}{\sqrt{3}} \cdot \frac{\Delta x}{u_{max}} \tag{A.15}$$

where Cr_{theory} is the Courant number taken from the RK3 entry in Table A.1 and u_{max} is the maximum velocity expected in the simulation. Given additional constraint from the time splitting, and to provide a safety buffer, the time step is usually chosen approximately 25% less than that given by equation A.15. For the ARW, the time step (in seconds) should be approximately 6 times the grid distance (in kilometers).

A.1.3 Transport

All transport of chemical species is done online and consistent with the WRF model, which uses a spatially 5^{th}-order evaluation of the horizontal flux divergence (advection) in the scalar conservation equation and a 3^{rd}-order evaluation of the vertical flux divergence coupled with the 3^{rd}-order Runge-kutta time integration scheme.

A.1.4 Planetary boundary layer physics

The planetary boundary layer (PBL) is responsible for vertical sub-grid-scale fluxes due to eddy transports in the whole atmospheric column, not just the boundary layer. The surface fluxes are provided by the surface layer and land-surface schemes. The PBL schemes determine the flux profiles within the well-mixed boundary layer and the stable layer, and thus provide atmospheric tendencies of temperature, moisture (including clouds), and horizontal momentum in the entire atmospheric column.

Yonsei University (YSU) PBL scheme uses the countergradient terms to represent fluxes due to non-local gradients and inclues an explicit treatment of the entrainment layer at the PBL top (Hong *et al.*, 2006). The boundary layer height is given by

$$h = Rib_{cr}\frac{\theta_{va}|U(h)|^2}{g[\theta_v(h) - \theta_s]} \tag{A.16}$$

where Rib_{cr} is the critical bulk Richardson number, $U(h)$ is the horizontal wind speed at h, θ_{va} is the virtual potential temperature at the lowest model level, $\theta_v(h)$ is the virtual potential temperature at h, and θ_s is the appropriate temperature near the surface. The temperature near the surface is defined as

$$\theta_s = \theta_{va} + \theta_T \left[= b\frac{\overline{(w'\theta_v')_0}}{w_s}\right] \tag{A.17}$$

where θ_T is the virtual temperature excess near the surface (the maximum of θ_T is 3 K in case θ_T becomes too large). Here $w_s = u_*\phi_m^{-1}$ is the mixed-layer velocity scale, where u_* is the surface frictional velocity scale, and ϕ_m is the wind profile function evaluated at the top of the surface layer. The virtual heat flux from the surface is $\overline{(w'\theta_v')_0}$ and the proportionality factor b is set as 7.8.

For the mixed layer ($z \leq h$), the turbulence diffusion equations for prognostic variables (C, u, v, θ, q, q_c, and q_i) can be expressed by

$$\frac{\partial C}{\partial t} = \frac{\partial}{\partial z}\left[K_c\left(\frac{\partial C}{\partial z} - \gamma_c\right) - \overline{(w'c')_h}\left(\frac{z}{h}\right)^3\right] \tag{A.18}$$

where K_c is the eddy diffusivity coefficient and γ_c is a correction to the local gradient, which incorporates the contribution of the large-scale eddies to the total flux. Here $\overline{(w'c')_h}$ is the flux at the inversion layer. The formula includes an asymptotic entrainment flux term $-\overline{(w'c')_h}(z/h)^3$ at the inversion layer. The PBL height h is defined as the level in which minimum flux exists at the inversion level. Above the mixed layer ($z \leq h$), a local diffusion approach is applied to account for free atmospheric diffusion. The penetration of entrainment flux above h is also considered.

A.2 The chemistry model

The chemistry model solves a set of chemical species conservation equations:

$$\frac{\partial C}{\partial t} = \nabla \cdot \mathbf{V}C + \nabla \cdot (K_e \nabla C) + P_{chem} - L_{chem} + E + (\frac{\partial C}{\partial t})_{clouds} + (\frac{\partial C}{\partial t})_{dry} \tag{A.19}$$

where C is the species volume mixing ratio, $\mathbf{V}$ is the three-dimensional velocity vector at each grid point in the model domain, K_e is the eddy diffusity used to parameterize the subgrid scale fluxes of trace species due to noncloudy turbulent motions, P_{chem} and L_{chem} are the production and loss rates due to chemical interactions, E is the emission rate, $(\partial C/\partial t)_{clouds}$ is the change of concentration due to cloud effects (including subgrid scale vertical redistribution, aqueous chemical interactions, and scavenging), and $(\partial C/\partial t)_{dry}$ represents the change in concentration due to dry deposition. A detailed description of WRF/Chem can be found in Grell *et al.* (2005) and more information

about WRF/Chem can be found on the website *http://ruc.noaa.gov/wrf/WG11.* The WRF/Chem model has multiple choice of gas-phase chemistry, photolysis schemes, aerosol modules, and biogenic emission calculations. The chemistry package consists of the following components:

- **Dry deposition**, coupled with the soil/vegetation scheme.
- **Aqueous phase chemistry**, coupled to some of the microphysics and aerosol schemes.
- **Transport**, including advection, convection and diffusion.
- **Photolysis**

  TUV (Tropospheric Ultraviolet and Visible) radiation scheme coupled with hydrometeors, aerosols and convective parameterizations.

  Fast TUV radiation scheme coupled with hydrometeors, aerosols and convective parameterizations.

  Fast-J photolysis scheme coupled with hydrometeors, aerosols and convective parameterizations.
- **Gas-phase chemical reaction** calculations

  RADM2 chemical mechanism, including the gas-phase chemical reaction calculations through the use of **KPP** (Kinetic Pre-Processor).

  CBM-Z mechanism.
- **Anthropogenic emissions**, user specified anthropogenic emission data computed from the emission inventory.
- **Biogenic emissions**

  Online calculation of biogenic emissions (Guenther *at al.*, 1994, and Simpson *et al.*, 1995) including emissions of isoprene, monoterpenes, and nitrogen emissions

by soil.

Online calculation of biogenic emissions using the **MEGAN** (Model of Emissions of Gases and Aerosols from Nature) biogenic emission routine.

Online modification of user specified biogenic emissions.

- **Aerosols**

  The Model Aerosol Dynamics model for Europe - **MADE/SORGAM** aerosol.

  The Model for Simulating Aerosol Interactions and Chemistry (**MOSAIC** - 4 or 8 bins) sectional model aerosol parameterization.

A.2.1 Dry deposition

The flux of trace gases and particles from the atmosphere to the surface is calculated by multiplying concentrations in the lowest model layer by the spatially and temporally varying deposition velocity v_d, which is proportional to the sum of three characteristic resistances (aerodynamic resistance, sublayer resistance, surface resistance). The surface resistance parameterizations developed by Wesely (1989) is used. In this parameterizations, the surface resistance is derived from the resistances of the surfaces of the soil and the plants. The properties of the plants are determined using land use data and the season. The surface resistance also depends on the diffusion coefficient, the reactivity, and water solubility of the reactive trace gas.

The dry deposition of sulfate is described differently. In case of simulations without calculating aerosols explicitly, sulfate is assumed to be present in the form of aerosol particles and its deposition is described according to Erisman *et al.* (1994). Otherwise sulfate deposition is calculated as outlined in the MADE/SORGAM aerosol parameterizations section.

When employing the aerosol parameterizations, the deposition velocity $\widehat{v}_{dk}$, for the kth moment of a polydisperse aerosol is given by

$$\widehat{v}_{dk} = (r_a + \widehat{r}_{dk} + r_a \widehat{r}_{dk} \widehat{v}_{Gk})^{-1} + \widehat{v}_{Gk}$$

where r_a is the surface resistance, $\widehat{v}_{Gk}$ is the polydisperse setting velocity, and $\widehat{r}_{dk}$ is the Brownian diffusivity (Slinn and Slinn, 1980; Grell *et al.*, 2005).

A.2.2 Photolysis - TUV and FTUV

Tropospheric Ultraviolet-Visible (TUV) model is a radiation transfer model developed by Madronich and Weller (1990). The code and the description of the model are available from http://www.acd.ucar.edu/TUV. The model calculates spectral irradiance, spectral actinic flux, and photodissociation rates (J-values) for the wavelength range between 121 and 750 nm.

Photolysis frequencies for the 21 photochemical reactions of the gas phase chemistry model are calculated at each grid point according to Madronich (1987). The photolysis rate for the gas (i), J_i is given by the integral of the product of the actinic flux $I_A(\lambda)$, the absorption cross sections $\sigma(\lambda)$, and the quantum yields $\Phi(\lambda)$ over the wavelength λ:

$$J_i = \int^{\lambda} I_A(\tau, \lambda) \sigma_i(\lambda) \Phi_i(\lambda) d\lambda$$

For the calculation of the actinic flux, a radiative transfer model which is based on the delta-Eddington technique (Joseph *et al.*, 1976) is used. This radiative transfer model accounts for absorption by O_2 and O_3, rayleigh scattering, and scattering and absorption by aerosol particles and clouds as described by Chang *et al.* (1987). The

absorption cross sections and the quantum yields for the calculation of J_i are given by Stockwell *et al.* (1990).

The profiles of the actinic flux are computed at each grid point of the model domain. For the determination of the absorption- and scattering cross sections needed by the radiative transfer model, predicted values of temperature, ozone, and cloud liquid water content are used below the upper boundary. Above the upper boundary, fixed typical temperature and ozone profiles are used to determine the absorption and scattering cross sections. These ozone profiles are scaled with total ozone mapping spectrometer (TOMS) satellite observational data for the area and date under consideration.

The TUV model permits the proper treatment of several cloud layers with height dependent liquid water contents. The extinction coefficient of cloud water β_c is parameterized as a function of the cloud water computed by the 3-dimensional model based on a parameterization given by Slingo (1989). For simplicity the wavelength dependent coefficients of the original were replaced by the fixed average values of 0.0275 and 1.3, which makes practically no effect on the computed actinic fluxes. For the present study, the effective radius of the cloud droplets simply follows Jones *at al.* (1994). For aerosol particles a constant extinction profile with an optical depth of 0.2 is applied.

The wavelength resolution used by TUV is sufficiently expensive, a simple version of TUV - Fast TUV (FTUV) is developed, which is about 8 times faster than TUV. The FTUV model (Tie *et al.*, 2003) has the same physical processes as the TUV model, except that the number of wavelength bins between 121-750 nm is reduced from 140 bins to 17 bins, and the actinic solar flux and effective cross section are averaged in the each bins. The differences in the calculated photolysis rates between TUV and FTUV are generally less than 5% in the troposphere.

A.2.3 The RADM2 chemical mechanism

The ozone formation chemistry is represented in the model by the RADM2 (Regional Acid Deposition Model, version 2) gas phase chemical mechanism (Chang *et al.*, 1987, Stockwell *et al.*, 1990), which includes 57 mechanism species and 158 reactions, of which 21 are photolytic. The 158 chemical reactions and the rate constant expressions can be found in Stockwell *et al.*, 1990) and *www.epa.gov/asmdnerl/CMAQ/ch08.pdf.* The 57 mechanism species are listed in Table A.2, of which the inorganic species include 12 stable species and 4 reactive intermediates, and the organic chemistry is represented by 25 stable species and 16 peroxy radicals.

The inorganic species are all represented explicitly in chemical mechanisms, and the important species included are O_3, NO, NO_2, HNO_3, $HONO$, H_2O_2, SO_2, CO and several radicals formed through their interactions with other species.

The organic mechanism is a lumped species type that uses a reactivity based weighting scheme to adjust for lumping, which most organic compounds are grouped together into surrogate mechanism species of similar reactivity and molecular weight (Stockwell *et al.*, 1990). Hundreds of volatile organic compounds (VOCs) are emitted into the atmosphere, and the primary non-methane VOCs (NMVOCs) are represented by 14 classes of mechanism species in RADM2, four of which are explicit because of their high emission rates or because of special reactivity considerations (ethane, ethene, isoprene and formaldehyde). The others represent groups of organic compounds aggregated on the basis of their reactivity with the hydroxyl radical (OH) and/or their molecular weights. The aggregation factor is the ratio of the fraction of the emitted compound which reacts to the fraction of the mechanism species which reacts:

$$F = \frac{1 - exp\{-k_{HO}(\mathrm{E}) \times \int [OH]\, dt\}}{1 - exp\{-k_{HO}(\mathrm{M}) \times \int [OH]\, dt\}}$$

Species	Name	Species	Name
Nitrogen		Organic nitrogen	
NO	Nitric oxide	PAN	Peroxyacetyl nitrate and higher PANs
NO2	Nitrogen dioxide	TPAN	$H(CO)CH = CHCO_3NO_2$
HONO	Nitrous acid	ONIT	Organic nitrate
NO3	Nitrogen trioxide		
N2O5	Nitrogen pentoxide	Organic peroxides	
HNO3	Nitric acid	OP1	Methyl hydrogen peroxide
HNO4	Pernitric acid	OP2	Higher organic peroxides
		PAA	Peroxyacetic acid
Oxidants			
O3	Ozone	Organic acids	
H2O2	Hydrogen peroxide	ORA1	Formic acid
		ORA2	Acetic and higher acids
Sulfur			
SO2	Sulfur dioxide	Peroxy radicals from alkanes	
SULF	Sulfuric acid	MO2	Methyl peroxy radical
		ETHP	Peroxy radical formed from ETH
Carbon oxides		HC3P	Peroxy radical formed from HC3
CO	Carbon monoxide	HC5P	Peroxy radical formed from HC5
		HC8P	Peroxy radical formed from HC8
Atomic species			
O3P	Oxygen atom (triplet)	Peroxy radicals from alkenes	
O1D	Oxygen atom (singlet)	OL2P	Peroxy radical formed from OL2
		OLTP	Peroxy radical formed from OLT
Odd hydrogen		OLIP	Peroxy radical formed from OLI
OH	Hydroxy radical		
HO2	Hydroperoxy radical	Peroxy radicals from aromatics	
		TOLP	Peroxy radical formed from TOL
Alkanes		XYLP	Peroxy radical formed from XYL
ETH	Ethane		
HC3	Alkanes w/$2.7 \times 10^{-13} < k_{OH} < 3.4 \times 10^{-12}$		
HC5	Alkanes w/$3.4 \times 10^{-12} < k_{OH} < 6.8 \times 10^{-12}$		
HC8	Alkanes w/$k_{OH} > 6.8 \times 10^{-12}$		
		Peroxy radicals with carbonyl groups	
Alkenes		ACO3	Acetylperoxy radical
OL2	Ethene	KETP	Peroxy radical formed from KET
OLT	Terminal olefins	TCO3	$H(CO)CH = CHCO_3$
OLI	Internal olefins		
ISO	Isoprene	Peroxy radicals involving nitrogen	
		XO2	NO to NO_2 operator
Aromatics		OLN	NO_3-alken adduct
TOL	Toluene and less reactive aromatics		
XYL	Xylene and more reactive aromatics		
CSL	Cresol and other hydroxy substituted aromatics		
Carbonyls			
HCHO	Formaldehyde		
ALD	Acetaldehyde and higher aldehydes		
KET	Ketones		
GLY	Glyoxal		
MGLY	Methyl glyoxal		
DCB	Unsaturated dicarbonyl		

Table A.2: List of RADM2 chemical species for gas-phase, k_{OH} ($cm^3\,molecule^{-1}s^{-1}$) is the reaction rate coefficient with OH.

where k_{OH}(E) is the rate constant for reaction of OH with the individual emitted compound, k_{OH}(M) is the rate constant for reaction of OH with the RADM2 mechanism species, and the term $\int[OH]\,dt$ is the daily average integrated OH radical concentration, which with an estimated value of 110 $ppt\,min.$

Alkanes are very important chemical species, they maybe transported over long distances as they react relatively slowly with OH radicals and have low deposition rates. Alkanes react with OH radicales to produce organic peroxy radicals (RO_2), which react with NO, HO_2 or other organic peroxy radicals. There are 4 species used in RADM2 to represent the nonmethane alkanes, they are: ETH (ethane); HC3 (propane, n-butane, isobutane and acetylene included); HC5 (Pentanes and hexanes included) and HC8 (most n-heptane, other C_7isomers and some C_{10} and higher isomers included).

Alkenes are more important constituents of the polluted and rural troposphere, as they have relatively high rate constants for reaction with OH radical. Alkenes can react with O_3 to produce aldehydes and highly reactive Criegee intermediates (such as CH_2O_2). The organic acids can be generated from alkenes through the reactions of Criegee intermediates. The highly reactive Alkenes are presented by 4 lumped species: OL2 (ethene); OLT (propene and other terminal olefins); OLI (trans-2-butene, cycloalkenes and other internal olefins) and ISO (isoprene).

Aromatics are very important under the polluted urban conditions, Glyoxal, methylglyoxal and unsaturated dicarbonyls are known products of aromatic decomposition. The RADM2 mechanism includes 3 primary aromatic groups: TOL (benzene, toluene and other less reactive aromatics); XYL (xylenes, other di- and polyalkylbenzenes, and other more reactive aromatics); CSL (cresols and other hydroxy substituted aromatics);

Aldehydes and ketones are mostly produced when organic peroxy radicals (RO_2) react with NO, they are presented in RADM2 by HCHO (formaldehyde);

ALD (acetaldehyde and higher aldehydes) and KET (acetone, methyl ethyl ketone and higher ketones).

A.2.4 Anthropogenic emissions

VOCs (volatile organic compounds) are known often hydrocarbons (HCs), but with smaller quantities of partially oxidized *VOCs*, such as alcohols, aldehydes, ketones and acids, with large natural and anthropogenic sources. The major urban anthropogenic sources are motor vehicle emissions and other sources of transportation, fuel consumption, gasoline evaporation and spillage, leaks of commercial natural gas, industrial processes, waste disposal, and chemical solvent emissions. The natural gas leaking are the major sources of ethane, and the rest contributions from car exhaust. The principal sources of propane are natural gas as well as chemical industrial process; and butane and pentane are primarily emitted from vehicle exhaust and gasoline, The higher alkanes arise mostly from solvent emissions. The alkenes, especially ethene, are primarily released from automobile exhaust, and partly from gasoline evaporation and spillage, in which half propene is estimated from industrial processes. Aromatic compounds are released mainly form incomplete combustion of fuel, three-quarters of benzene are arisen from vehicle exhaust and the rest from fuel spillage; toluene and ethylbenzene are in part from vehicle exhaust and gasoline, and in part from solvent emissions (Warneck, 2000). Carbonyls (formaldehyde, acetaldehydes, acetone, ketones etc.) are byproducts of hydrocarnon oxidation and also are emitted from natural and anthropogenic sources, such as the buring of wood, fuels or household waste (Brasseur *et al.*,1999, Warneck, 2000).

In order to construct an anthropogenic inventory used in WRF/Chem model, the emitted chemical species are translated into a limit number of model groups though the use of reactivity weighting, which lump several similar chemical species

into one simulated species, or one emitted species being partitioned into fractions of several simulated species. The anthropogenic emission data for gas-phase species including 14 surrogate nonmethane VOCs which described in section A.2.3 along with the 6 primary species (SO_2, CO, NO_x, NH_3, $PM_{2.5}$ and PM_{10}) are divided into 24 average hourly emissions. The conversion table, which converts primary chemical emitted species (41 speciated VOC compounds and the aggregation factors) to RADM2 emissions input, can be found on *http://ruc.noaa.gov/wrf/WG11/speciation.htm.*

Anthropogenic emissions can be computed from the USA EPA (Environmental Protection Agency)'s 1999 National Emissions Inventory (NEI99-version 3), released in November 2003 and updated in March 5, 2004. Canadian area and mobile source emissions are also included south of 52°N latitude. However, in this inventory Canadian point sources are not included. Emissions estimates for Mexico (north of 29°N latitude) are also included. All biogenic sources of VOC and NOx, and all fire-related emissions have been removed from the U.S., Canadian and Mexican source files in this inventory. The emissions are representative of a typical summer day (average of weekday and weekend days), with 4 km horizontal data spacing of the area emissions. Gridded area emissions are based on EPA's spatial surrogate file designed for the NEI-99 inventory. Point emissions are given in terms of latitude and longitude location, with stack parameter information included to allow for plume-rise calculations. More information of the anthropogenic inventory can be found on *http://ruc.noaa.gov/wrf/WG11/anthropogenic.htm.*

A.2.5 Biogenic emissions

The biogenic emission module treats the emissions of isoprene, monoterpenes, other biogenic VOC (OVOC), and nitrogen emission by the soil. Biogenic emission is based on the description of Guenther *et al.* (1994), Simpson *et al.* (1995) and Schoenemeyer

et al. (1997). In RADM2 photochemistry modules, the emissions of monoterpenes and OVOC are disaggregated into the appropriate species classes.

The emission of isoprene by forests depends on both temperature and photosynthetic active radiation. Guenther *et al.* (1994) have developed a parameterization formula for the isoprene emission, where the isoprene emission rate is proportional to the isoprene emission rate at a standard temperature and a standard flux of photosynthetic active radiation (PAR). A radiation flux correction term and a temperature correction term for forest isoprene emissions is applied. The isoprene emissions of agricultural and grassland areas are considered to be functions of the temperature only (Hahn *et al.* 1994).

The emissions of monoterpenes, OVOC, and nitrogen are also treated as functions of the temperature only. Little is known about the emission of OVOC, therefore the same temperature correction is applied for OVOC as for monoterpenes according to Simpson *et al.* (1995).

The emissions at the standard temperature and the standard PAR flux are given in Table A.3. They are taken from Guenther *et al.* (1994) for deciduous, coniferous and mixed forest and from Schoenemeyer *et al.* (1997) for agricultural and grassland. For the use with RADM2, all nitrogen emissions are treated as NO. This is a maximum estimate, because the emission of N_2O is neglected.

It should be noted that from the landuse categories used in WRF, the nature of biogenic emissions can only be roughly estimated. These categories are based on the USGS (US Geological Survey) 24-class land use or land cover system classification, which in its original WRF implementation does not include any tree species information of fractional coverage.

Landuse categories	Isoprene $ugC/(m^2h)$	Monoterpenes $ugC/(m^2h)$	OVOC $ugC/(m^2h)$	Nitrogen $ngN/(m^2s)$
1 Urban & built-up land	0	0	0	0
2 Dryland cropland & pasture	8	20	12	9
3 Irrigated cropland & pasture	8	20	12	9
4 Mix. dry/irrg. cropland & pasture	8	20	12	9
5 Cropland/grassland mosaic	4	20	46	4.95
6 Cropland/woodland mosaic	2204	202.5	363.5	4.535
7 Grassland	0	20	80	0.9
8 Shrubland	0	20	80	0.07
9 Mixed shrubland/grassland	0	20	80	0.07
10 Savanna	0	0	0	0
11 Deciduous broadleaf forest	4400	385	715	0.07
12 Deciduous needleleaf forest	780	1380	840	0.07
13 Evergreen broadleaf forest	4400	385	715	0.07
14 Evergreen needleleaf forest	780	1380	840	0.07
15 Mixed Forest	5775	1001	924	0.07
16 Water Bodies	0	0	0	0
17 Herbaceous wetland	0	0	0	0
18 Wooded wetland	5775	1001	924	0.07
19 Barren or sparsely vegetated	0	0	0	0
20 Herbaceous Tundra	70	0	0	0
21 Wooded Tundra	70	0	0	0
22 Mixed Tundra	70	0	0	0
23 Bare Ground Tundra	0	0	0	0
24 Snow or Ice	0	0	0	0

Table A.3: Emission rates at standard temperature (303.15 K for isoprene, monoterpenes and OVOC, 273.15 K for nitrogen) and standard flux ($1000\mu molm^{-2}s^{-1}$) of photosynthetic active radiation.

A.2.6 Aerosol radiative module

The aerosol is represented by a three-moment approach with a log-normal size distribution:

$$n(\ln D) = \frac{N}{\sqrt{2\pi}\ln\sigma_g} exp\left[-\frac{1}{2}\left(\frac{\ln D - \ln D_g}{\ln\sigma_g}\right)^2\right] \tag{A.20}$$

where D is the particle diameter, N is the number concentrations, D_g is the geometric mean diameter, and σ_g is the geometric standard deviation.

To calculate the aerosol optical properties, the spectrum of fine aerosol is divided into 48 bins from 0.002 μm to 2.5 μm. When the radius (r_i) is less than 0.1 μm, the interval of bins ranges from 0.001 to 0.005 μm; and when the radius is greater than 0.1 μm, the interval is increased to 0.025 to 0.25 μm. The aerosols are classified into four types: (1) internally mixed sulfate, nitrate, ammonium, hydrophilic organic, hydrophilic black carbon, and water; (2) hydrophobic organic; (3) hydrophobic black carbon; and (4) other unidentified aerosols (such as dust and sea salt). These four kinds of aerosols are assumed to be mixed externally. For the internally mixed aerosols, the complex refractive index at a given wavelength (λ) is calculated based on the volume-weighted average of the individual refractive index. Given the particle size and complex refractive index, the extinction efficiency (Q_e), the single scattering albedo (SSA, ω_a), and the asymmetry factor (g_a) are calculated using the Mie theory at a given wavelength.

The aerosol optical thickness (AOT, τ_a) at a given wavelength λ in a given atmospheric layer k is determined by the summation over all types of aerosols and all bins:

$$\tau_a(\lambda, k) = \sum_{i=1}^{48}\sum_{j=1}^{4} Q_e(\lambda, r_i, j, k)\pi {r_i}^2 n(r_i, j, k)\Delta z_k \tag{A.21}$$

where $n(r_i, j, k)$ is the number concentration of j^{th} kind of aerosols in i^{th} bin. Δz_k is the depth of an atmospheric layer. The weighted-mean values of ω_a and g_a are

calculated by

$$\omega_a(\lambda,k) = \sum_{i=1}^{48}\sum_{j=1}^{4} Q_e(\lambda,r_i,j,k)\pi {r_i}^2 n(r_i,j,k)\omega_a(\lambda,r_i,j,k)\Delta z_k/\tau_a(\lambda,k) \quad \text{(A.22)}$$

$$g_a(\lambda,k) = \frac{\sum_{i=1}^{48}\sum_{j=1}^{4} Q_e(\lambda,r_i,j,k)\pi {r_i}^2 n(r_i,j,k)\omega_a(\lambda,r_i,j,k)g_a(\lambda,r_i,j,k)\Delta z_k}{\sum_{i=1}^{48}\sum_{j=1}^{4} Q_e(\lambda,r_i,j,k)\pi {r_i}^2 n(r_i,j,k)\omega_a(\lambda,r_i,j,k)\Delta z_k} \quad \text{(A.23)}$$

When the wavelength-dependent aerosol radiative properties τ_a, ω_a, and g_a are obtained, they can be used in the short wave radiative transfer modules in the WRF/CHEM model.

References

[1] Ansmann, A., I. Mattis, D. Müller, U. Wandinger, M. Radlach, D. Althausen, and R. Damoah, 2005: Ice formation in Saharan dust over central Europe observed with temperature/humidity/aerosol Raman lidar. *J. Geophys. Res.*, **110**, D18, doi:10.1029/2004JD005000.

[2] Barnard, J. C., J. D. Fast, G. Paredes-Miranda, W. P. Arnott, and A. Laskin, 2010: Technical Note: Evaluation of the WRF-Chem "Aerosol Chemical to Aerosol Optical Properties" Module using data from the MILAGRO campaign, *Atmos. Chem. Phys.*, **10**, 7325-7340.

[3] Barker, D.M., W. Huang, Y. R. Guo, and Q. N. Xiao, 2001: A Three-Dimensional (3DVAR) Data Assimilation System For Use With MM5: Implementation and Initial Results. *Mon. Wea. Rev.*, **132**, 897-914.

[4] Baumgardner D., G. Raga, G. Kok, J. Ogren, I. Rosas, A. Báez, and T. Novakov, 2000: On the evolution of aerosol properties at a mountain site above Mexico City, *J. Geophys. Res.*, **105**, D17, doi:10.1029/2000JD900299.

[5] Bian H., C. S. Zender, 2003: Mineral dust and global tropospheric chemistry: Relative roles of photolysis and heterogeneous uptake, *J. Geophys. Res.*, **108**(D21), 4672, doi:10.1029/2002JD003143, 2003.

[6] Bian H., S.Q. Han, X. Tie, M.L. Shun, and A.X. Liu, 2007: Evidence of impact of aerosols on surface ozone concentration: A case study in Tianjin, China. *Atmos. Environ.*, **41**, 4672-4681.

[7] Bossert, J. E., 1997: An investigation of flow regimes affecting the Mexici City region, *J. Applied Met.*, **36**, 119–140.

[8] Brasseur, G. P., J. J. Orlando, G. S. Tyndall, 1999: Atmospheric chemistry and global change. Oxford University Press, New York.

[9] Brasseur, G. P., R. G. Prinn and A. Pszenny, 2003: Atmospheric chemistry in a changing world : an integration and synthesis of a decade of tropospheric chemistry research. Springer-Verlag Berlin Heidelberg New York.

[10] Castro, T., S. Madronich, S. Rivale, A. Muhlia, and B. Mar, 2001: The influence of aerosols on photochemical smog in Mexico City, *Atmos. Environ.*, **35**, 1765-1772.

[11] Chang J. S., R.A. Brost, I. S. A. Isaksen, S. Madronich, P. Middleton, W.R. Stockwell and C.J. Waleck, 1987: A three-dimensional Eulerian acid deposition model: physical concepts and formulation. *J. Geophys. Res.*, **92**, 14,681 - 14,700.

[12] Chapman, E. G., W. I. Gustafson Jr., R. C. Easter, J. C. Barnard, S. J. Ghan, M. S. Pekour, and J. D. Fast, 2009: Coupling aerosol-cloud-radiative processes in the WRF-Chem model: Investigating the radiative impact of elevated point sources *Atmos. Chem. Phys.*, **9**, 945-964, doi:10.5194/acp-9-945-2009.

[13] Chen, F., and J. Dudhia, 2001: Coupling an advanced land-surface/ hydrology model with the Penn State/ NCAR MM5 modeling system. Part I: Model description and implementation. *Mon. Wea. Rev.*, **129**, 569-585.

[14] Chiapello, I., G. Bergametti, B. Chatenet, F. Dulac, I. Jankowiak, C. Liousse, and E. S. Soares, 1999: Contribution of the different aerosol species to the aerosol mass load and optical depth over the northeastern tropical Atlantic. *J. Geophys. Res.*, **104**(D4), 4025-4035.

[15] Chin, M., R. Rood, S.J. Lin, J.F. Müller, and A. Thompson, 2000: Atmospheric sulfur cycle simulated in the global model GOCART: Model description and global properties. *J. Geophys. Res.*, **105**, D20, doi:10.1029/2000JD900384.

[16] Chow, J. C., J. G. Watson, S. A. Edgerton, and E. Vega, 2002: Chemical composition of PM2.5 and PM10 in Mexico City during winter 1997, *Science of The Total Environment*, **287**, 177-201.

[17] Daum, P., *et al.*, 2004: Origin and properties of plumes of high ozone observed during the Texas 2000 Air Quality Study (TexAQS 2000), *J. Geophys. Res.*, **109**, D17306, doi:10.1029/2003JD004311.

[18] de Foy, B., E. Caetano, V. Magana, A. Zitacuaro, B. Cardenas, A. Retama, R. Ramos, L.T. Molina, and M. J. Molina, 2005: Mexico City basin wind circulation during the MCMA-2003 field campaign. *Atmos. Chem. Phys.*, **5**, 2267-2288.

[19] de Foy, B., A. Clappier, L. T. Molina, and M. J. Molina, 2006: Distinct wind convergence patterns in the Mexico City basin due to the interaction of the gap winds with the synoptic flow, *Atmos. Chem. Phys.*, **6**, 1249-1265.

[20] de Foy, B., J.R. Varela, L.T. Molina, and M.J. Molina, 2006a: Rapid ventilation of the Mexico City basin and regional fate of the urban plume. *Atmos. Chem. Phys.*, **6**, 2321-2335.

[21] de Foy, B., Fast, J. D., Paech, S. J., Phillips, D., Walters, J. T., Coulter, R. L., Martin, T. J., Pekour, M. S., Shaw, W. J., Kasten- deuch, P. P., Marley, N.

A., Retama, A., and Molina, L. T., 2008: Basin-scale wind transport during the MILAGRO field campaign and comparison to climatology using cluster analysis, *Atmos. Chem. Phys.*, **8**, 1209-1224, doi:10.5194/acp-8-1209-2008.

[22] Díaz-Nigenda, E., J. Tatarko, A. D. Jazcilevich, A. R. García, E. Caetano, L. G. Ruíz-Suárez, 2010: A modeling study of Aeolian erosion enhanced by surface wind confluences over Mexico City. *Aeolian Research*, doi:10.1016/j.aeolia.2010.04.004.

[23] Doran, J. C. *et al.*, 1998: The IMADA-AVER boundary layer experiment in the Mexico City area, *Bull. Am. Met. Soc.*, **79**, 2497-2508.

[24] Doran, J. C., J.C. Barnard, W.P. Arnott, R. Cary, R. Coulter, J. D. Fast, E.I. Kassianov, L. Kleinman, N.S. Laulainen, T. Martin, G. Paredes-Miranda, M.S. Pekour, W.J. Shaw, D.F. Smith, S.R. Springston, and X.-Y. Yu, 2007: The T1-T2 study: evolution of aerosol properties downwind of Mexico City, *Atmos. Chem. Phys.*,**7**, 1585-1598.

[25] Dudhia, J., 1989: Numerical study of convection observed during the winter monsoon experiment using a mesoscale two-dimensional model, *J. Atmos. Sci.*, **46**, 3077-3107.

[26] Edgerton, S. *et al.*, 1999: Particulate air pollution in Mexico City. A collaborative research project, *J. Air Waste Manag. Assoc.*, **49**, 1221-1229.

[27] Emmons, L. K., Apel, E. C., Lamarque, J.-F., Hess, P. G., Avery, M., Blake, D., Brune, W., Campos, T., Crawford, J., DeCarlo, P. F., Hall, S., Heikes, B., Holloway, J., Jimenez, J. L., Knapp, D. J., Kok, G., Mena-Carrasco, M., Olson, J., O'ullivan, D., Sachse, G., Walega, J., Weibring, P., Weinheimer, A., and Wiedinmyer, C., 2010: Impact of Mexico City emissions on regional air quality from MOZART-4 simulations, *Atmos. Chem. Phys.*, **10**, 6195-6212, doi:10.5194/acp-10-6195-2010.

[28] Erisman, J. W., A. van Pul, and P. Wyers, 1994: Parameterization of surface resistance for the quantification of atmospheric deposition of acidifying pollutants and ozone. *Atmos. Environ.*, **28**, 2595-2607.

[29] Fast, J. D. and S. Zhong, 1998: Meteorological factors associated with inhomogeneous ozone concentrations within the Mexico City basin. *J. of Geophys. Res.*, **103**, 18927–18946.

[30] Fast, J. D., W. I. Gustafson Jr., R. C. Easter, R. A. Zaveri, J. C. Barnard, E. G. Chapman, G. A. Grell, and S. E. Peckham, 2006: Evolution of ozone, particulates, and aerosol direct radiative forcing in the vicinity of Houston using a fully coupled meteorology-chemistry-aerosol model, *J. Geophys. Res.*, **111**, D21305, doi:10.1029/2005JD006721.

[31] Fast, J. D., B. de Foy, F. Acevedo Rosas, E. Caetano, G. Carmichael, L. Emmons, D. McKenna, M. Mena, W. Skamarock, X. Tie, R. L. Coulter, J. C. Barnard, C. Wiedinmyer, and S. Madronich, 2007: A meteorological overview of the MILAGRO field campaigns, *Atmos. Chem. Phys.*, **7**, 2233–2257.

[32] Fast, J., A. C. Aiken, J. Allan, L. Alexander, T. Campos, M. R. Canagaratna, E. Chapman, P. F. DeCarlo, B. de Foy, J. Gaffney, J. de Gouw, J. C. Doran, L. Emmons, A. Hodzic, S. C. Herndon, G. Huey, J. T. Jayne, J. L. Jimenez, L. Kleinman,W. Kuster, N. Marley, L. Russel, C. Ochoa, T. B. Onasch, M. Pekour, C. Song, I. M. Ulbrich, C. Warneke, D. Welsh-Bon, C. Wiedinmyer, D. R. Worsnop, X.-Y. Yu, and R. Zaveri, 2009: Evaluating simulated primary anthropogenic and biomass burning organic aerosols during MILAGRO: implications for assessing treatments of secondary organic aerosols, *Atmos. Chem. Phys.*, **9**, 6191-6215.

[33] Finlayson-pitts, B. J., and J. N. Pitts, Jr., 2000: Chemistry of the upper and lower atmosphere: theory, experments and applications. Academic Press, A Harcourt Science and Technology Company.

[34] Garcia, A., 2004: Mexico Evaluacion de Escenarios Utilizando el Modelo Regional de Calidad del Aire Multiscale Climate Chemistry Model. CCA- Universidad Nacional Autonoma de Mexico. Ph.D. Thesis, Universidad Nacional Autonoma de Mexico.

[35] Ginoux, P., M. Chin, I. Tegen, J. Prospero, B. Holben, O. Dubovik, and S.-J. Lin, 2001: Sources and distributions of dust aerosols simulated with the GOCART model. *J. Geophys. Res.*, **106**(D17), 20255-20273.

[36] Ginoux, P., I. Geogdzhayev, B. Holben, G. Stenchikov, and X. Tie, 2006: Evaluation of aerosol distribution and optical depth in GFDL couple model. *J. Geophys. Res.*, **111**, D22210, doi:10.1029/2005JD006707.

[37] Grell, Georg A., Steven E. Peckham, Rainer Schmitz, Stuart A. McKeen, Gregory Frost, William C. Skamarock and Brian Eder, 2005: Fully coupled "online" chemistry within the WRF model, *Atmos. Environ.*, **39**, 6957-6975.

[38] Grini A., G. Myhre, C. S. Zender, I. S. A. Isaksen, 2005: Model simulations of dust sources and transport in the global atmosphere: Effects of soil erodibility and wind speed variability, *J. Geophys. Res.*, **110**, D02205, doi:10.1029/2004JD005037.

[39] Guenther, A., P. Zimmerman, and M. Wildermuth, 1994: Natural volatile organic compound emission rate estimates for U.S. woodland landscapes. *Atmos. Environ.*, **28**, 1197-1210.

[40] Guenther, A., T. Karl, P. Harley, C. Wiedinmyer, P. I. Palmer, and C. Geron, 2006: Estimates of global terrestrial isoprene emissions using MEGAN (Model of Emissions of Gases and Aerosols from Nature) *Atmos. Chem. Phys.*, **6**, 3181-3210.

[41] Hahn, J., J. Steinbrecher, and R. Steinbrecher, 1994: Studie F: Emission von Nicht-Methan-Kohlenwasserstoffen aus der Landwirtschaft. In: Enquete-Kommission 'Schutz der Erdatmosphaere' des Deutschen Bundestages (Hrsg.), Studienprogramm Band 1 'Landwirtschaft', Teilband 1 , Economica Verlag, Bonn.

[42] Harley, R., et al., 1993: Photochemical modeling of the Southern California Air Quality Study, *Environ. Sci. Tech.*, **27**, 378-388.

[43] He, S., and G. R. Carmichael, 1999: Sensitivity of photolysis rates and ozone production in the troposphere to aerosol properties, *J. Geophys. Res.*, **104**(D21), 26,307-26,324.

[44] Herwehe, J. A., T. L. Otte, R. Mathur, S. Trivikrama Rao, 2001: Diagnostic analysis of ozone concentrations simulated by two regional-scale air quality models, *Atmos. Environ.*, **45**, 5957-5969.

[45] Hodzic, A., J. L. Jimenez, S. Madronich, A. C. Aiken, B. Bessagnet, G. Curci, J. Fast, J.-F. Lamarque, T. B. Onasch, G. Roux, J. J. Schauer, E. A. Stone, and I. M. Ulbrich, 2009: Modeling organic aerosols during MILAGRO: importance of biogenic secondary organic aerosols *Atmos. Chem. Phys.*, **9**, 6949-6981.

[46] Hong, S., Y. Noh and J. Dudhia, 2006: A New Vertical Diffusion Package with an Explicit Treatment of Entrainment Processes. *Mon. Wea. Rev.*, **134**, 2318-2341.

[47] Horowitz, L.W., S. Walters, D. Mauzerall, L. Emmons, P. Rasch, C. Granier, X. Tie, J.F. Lamarqu, M. Schultz, G. Tyndall, J. Orlando, G. Brasseur, 2003: A global simulation of tropospheric ozone and related tracers: Description

and evaluation of MOZART, version 2. *J. Geophys. Res.*, **108**(D24), 4784, doi:10.1029/2002JD002853.

[48] IMP (Instituto Mexicano el Petróleo, 1998: Investigación sobre materia particulada y deterioro atmosférico, Subdirección de Protección Ambiental, 1994-1998.

[49] Jacob, Daniel J., 1999: Introduction to Atmospheric Chemistry. Princeton University Press.

[50] Jiang, F., T. Wang, T. Wang, M. Xie and H. Zhao, 2008: Numerical modeling of a continuous photochemical pollution episode in Hong Kong using WRF-Chem, *Atmos. Environ.*, **42**, 8717-8727.

[51] Jiang, M., L.C. Marr, E.J. Dunlea, S.C. Herndon, J.T. Jayne, C.E. Kolb, W.B. Knighton, T.M. Rogers, M. Zavala, L.T. Molina, and M.J. Molina, 2005: Vehicle fleet emissions of black carbon, polycyclic aromatic hydrocarbons, and other pollutants measured by a mobile laboratory in Mexico City. *Atmos. Chem. Phys.*, **5**, 3377-3387.

[52] Jones, A., D. Roberts, A. Slingo, 1994: A climate model study of indirect radiative forcing by anthropogenic sulphate aerosols. *Nature*, **370**, 450-453.

[53] Joseph, J. H., W. J. Wiscombe, J. A. Weinmann, 1976: The delta-Eddington approximation for radiative flux transfer. *J. Atmos. Sci.*, **33**, 2452-2458.

[54] Kaufman, Y.J., A. Gitelson, A. Karnieli, E. Ganor, R.S. Fraser, T. Nakajima, S. Mattoo, and B.N. Holben, 1994: Size distribution and scattering phase function of aerosol particles retrieved from sky brightness measurementsr. *J. Geophys. Res.*, **99**, 10341-10356.

[55] Kleinman, L., *et al.*, 2000, Ozone production in the New York City urban plume, *J.Geophys. Res.*, **105**, 14495-14511.

[56] Kleinman, L., *et al.*, 2005: A comparative study of ozone production in five U.S. metropolitan areas, *J. Geophys. Res.*, **110**, D02301, doi:10.1029/2004JD005096.

[57] Kleinman, L. I., S.R. Springston, P.H. Daum, Y.-N. Lee, L.J. Nunnermacker, G.I. Senum, J. Wang, J. Weinstein-Lloyd, M.L. Alexander, J. Hubbe, J. Ortega, 2008: M.R. Canagaratna, and J. Jayne: The time evolution of aerosol composition over the Mexico City plateau. *Atmos. Chem. Phys.*,**8**, 1559-1575.

[58] Kleinman, L. I., S.R. Springston, J. Wang, P.H. Daum, Y.-N. Lee, L.J. Nunnermacker, G.I. Senum, J. Weinstein-Lloyd, M.L. Alexander, J. Hubbe, J. Ortega, R.A. Zaveri, M.R. Canagaratna, and J. Jayne, 2009: The time evolution of aerosol size distribution over the Mexico City plateau. *Atmos. Chem. Phys.*, **9**, 4261-4278.

[59] Kley, D., H. Geiss and V. A. Mohnen, 1994: Tropospheric ozone at elevated sites and precursor emissions in the United States and Europe, *Atmos. Environ.*, **28**, 149-158.

[60] LANL/IMP (Los Alamos National Laboratory and Instituto Mexicano del Petroleo), Mexico City Air Quality Research Initiative, Los Alamos, NM, 1994.

[61] Laprise R., 1992: The Euler Equations of motion with hydrostatic pressure as as independent variable, *Mon. Wea. Rev.*, **120**, 197-207.

[62] Lei, W., B. de Foy, M. Zavala, R. Volkamer, and L. T. Molina, 2007: Characterizing ozone production in the Mexico City Metropolitan Area: a case study using a chemical transport model, *Atmos. Chem. Phys.*, **7**, 1347-1366.

[63] Lei, W., M. Zavala, B. de Foy, R. Volkamer, and L. T. Molina, 2008: Characterizing ozone production and response under different meteorological conditions in Mexico City, *Atmos. Chem. Phys. Discuss.*, **8**, 12053-12079.

[64] Lin, Y.-L., R. D. Farley, and H. D. Orville, 1983: Bulk parameterization of the snow field in a cloud model. *J. Climate Appl. Meteor.*, **22**, 1065-1092.

[65] Madronich, S., 1987: Photodissociation in the Atmosphere 1. Actinic Flux and the Effects of Ground Reflections and Clouds, *J. Geophys. Res.*, **92**(D8), 9740-9752.

[66] Madronich, S., and G. Weller, 1990: Numerical integration errors in calculated tropospheric photodissociation rate coefficients, *J. Atmos. Chem.*, **10**, 289-300.

[67] Madronich, S. and S. Flocke, 1999: The role of solar radiation in atmospheric chemistry, in Handbook of Environmental Chemistry (P. Boule, ed.), Springer-Verlag, Heidelberg, pp. 1-26.

[68] Madronich, S., 2006: Chemical evolution of gaseous air pollutants down-wind of tropical megacities: Mexico City case study, *Atmos. Environ.*, **40**, 6012-6018.

[69] Marticorena, B., and G. Bergametti, 1995: Modeling the atmospheric dust cycle: 1. Design of a soil-derived dust emission scheme, *J. Geophys. Res.*, **100**(D8), 16415-16430.

[70] Martin, R., D. J. Jacob, J. A. Logan, I. Bey, R. M. Yantosca, A. C. Staudt, Q. Li, A. M. Fiore, B. N. Duncan, H. Liu, P. Ginoux and V. Thouret, 2002: Interpretation of TOMS observations of tropical tropospheric ozone with a global model and in situ observations, *J. Geophys. Res.*, **107**(D18), 4351, doi:10.1029/2001JD001480.

[71] Martin, R., A. Fiore, and A. Van Donkelaar, 2004: Space-based diagnosis of surface ozone sensitivity to anthropogenic emissions, *Geophys. Res. Lett.*, **31**, doi:10.1029/2004GL019416.

[72] Milford, J., A. Russell, and G. McRae, 1989: A new approach to photochemical pollution control: implications of spatial patterns in pollutant responses to reductions in nitrogen oxides and reactive organic gas emissions, *Environ. Sci. Tech.*, **23**, 1290-1301.

[73] Milford, J., D. Gao, S. Sillman, P. Blossey, and A. Russell, 1994: Total reactive nitrogen (NOy) as an indicator of the sensitivity of ozone to reductions in hydrocarbon and NOx emissions, *J. Geophys. Res.*, **99**, D2, doi:10.1029/93JD03224.

[74] Miller R. L., I. Tegen, J. Perlwitz, 2004: Surface radiative forcing by soil dust aerosols and the hydrologic cycle, *J. Geophys. Res.*, **109**, D04203, doi:10.1029/2003JD004085.

[75] Mlawer, E. J., S. J. Taubman, P. D. Brown, M. J. Iacono, and S. A. Clough, 1997: Radiative transfer for inhomogeneous atmosphere: RRTM, a validated correlated-k model for the longwave. *J. Geophys. Res.*, **102** (D14), 16663-16682.

[76] Molina, L. and M. Molina, 2002: Air quality in the Mexico Megacity: an integrated assessment, Kluwer Academic Publisher.

[77] Molina, L.T., C.E. Kolb, B. de Foy, B.K. Lamb, W.H. Brune, J.L. Jimenez, R. Ramos-Villegas, J. Sarmiento, V.H. Paramo-Figueroa, B. Cardenas, V. Gutierrez-Avedoy, and M.J. Molina, 2007: Air quality in North America's most populous city - overview of the MCMA-2003 campaign. *Atmos. Chem. Phys.*, **7**, 2447-2473.

[78] Molina, L. T., S. Madronich, J. S. Gaffney, E. Apel, B. de Foy, J. Fast, R. Ferrare, S. Herndon, J. L. Jimenez, B. Lamb, A. R. Osornio-Vargas, P. Russell, J. J. Schauer, P. S. Stevens, R. Volkamer, and M. Zavala, 2010: An overview of the MILAGRO 2006 Campaign: Mexico City emissions and their transport and transformation, *Atmos. Chem. Phys.*, **10**, 8697-8760, doi:10.5194/acp-10-8697-2010.

[79] Mugica, V., E. Ortiz, L. Molina, A. De Vizcaya-Ruiz, A. Nebot, R. Quintana, J. Aguilar, E. Alcátara, 2009: PM composition and source reconciliation in Mexico City, *Atmos. Environ.*, **43**, 5068-5074.

[80] Nunnermacker, L., J. Weinstein-Lloyd, B. Hillery, B. Giebel, L. Kleinman, S. Springston, P. Daum, J. Gaffney, N. Marley, and G. Huey, 2008: Aircraft and ground-based measurements of hydroperoxides during the 2006 MILAGRO field campaign, *Atmos. Chem. Phys. Discuss.*, **8**, 7619-7636, doi:10.5194/acp-8-7619-2008.

[81] Penner, J. E., et al., 2001: Aerosols, their direct and indirect effects, in Climate Change 2001: The Scientific Basis. Contribution of Working Group I to the Third Assessment Report of the Intergovernmental Panel on Climate Change, edited by J. T. Houghton *et al.*, chap. 5, pp. 291-336, Cambridge Univ. Press, New York.

[82] Perlwitz, J., I. Tegen, and R. Miller, 2001: Interactive soil dust aerosol model in the GISS GCM 1. Sensitivity of the soil dust cycle to radiative properties of soil dust aerosols, *J. Geophys. Res.*, **106**(D16), 18167-18192.

[83] Plummer, D. A., 1999: On-line Chemistry in a Mesoscale Model: Assessment of the Toronto Emission Inventory and Lake-Breeze Effects on Air Quality. Ph.D. Thesis, York University.

[84] Plummer D., J. McConnell, L. Neary, J. Kominski, R. Benoit, J. Drummond, J. Narayan, V. Young, D. Hastie, 2001: Assessment of emissions data for the Toronto region using aircraft-based measurements and an air quality model *Atmos. Environ.*, **35**, 6453-6463.

[85] Querol, X., J. Pey, M. C. Minguillón, N. Pérez, A. Alastuey, M. Viana, T. Moreno, R. M. Bernabé, S. Blanco, B. Cárdenas, E. Vega, G. Sosa, S. Escalona,

H. Ruiz, and B. Artíñano, 2008: PM speciation and sources in Mexico during the MILAGRO-2006 Campaign, *Atmos. Chem. Phys.*, **8**, 111-128, doi:10.5194/acp-8-111-2008.

[86] Raga, G. B., D. Baumgardner, T. Castro, A. Martínez-Arroyo, R. Navarro-González, 2001: Mexico City air quality: a qualitative review of gas and aerosol measurments (1960-2000). *Atmos. Environ.*, **35**, 4041–4058.

[87] Salcedo, D., T.B. Onasch, K. Dzepina, M.R. Canagaratna, Q. Zhang, J.A. Huffman, P.F. DeCarlo, J.T. Jayne, P. Mortimer, D.R. Worsnop, C.E. Kolb, K.S. Johnson, B. Zuberi, L.C. Marr, R. Volkamer, L.T. Molina, M.J. Molina, B. Cardenas, R.M. Bernab, C. Mrquez, J.S. Gaffney, N.A. Marley, A. Laskin, V. Shutthanandan, Y. Xie, W. Brune, R. Lesher, T. Shirley, and J.L. Jimenez, 2006: Characterization of ambient aerosols in Mexico City during the MCMA-2003 campaign with Aerosol Mass Spectrometry: results from the CENICA Supersite. *Atmos. Chem. Phys.*, **6**, 925-946.

[88] Schoenemeyer, T., K. Richter, and G. Smiatek, 1997: Vorstudie uber ein raumlich und zeitlich aufgelostes Kataster anthropogener und biogener Emissionen fuer Bayern mit Entwicklung eines Prototyps und Anwendung fur Immissionsprognosen. Abschluss bericht an das Bayerische Landesamt fur Umweltschutz. Fraunhofer-Institut fuer Atmosphaerische Umweltforschung, Garmisch-Partenkirchen.

[89] Seinfeld, John H. and Spyros N. Pandis, 2006: Atmospheric Chemistry and Physics, From air pollution to climate change, John Wiley & Sons.

[90] Shinozuka, Y., A. D. Clarke, P. F. DeCarlo, J. L. Jimenez, E. J. Dunlea, G. C. Roberts, J. M. Tomlinson, D. R. Collins, S. G. Howell, V. N. Kapustin, C. S. McNaughton, and J. Zhou, 2009: Aerosol optical properties relevant to

regional remote sensing of CCN activity and links to their organic mass fraction: airborne observations over Central Mexico and the US West Coast during MILAGRO/INTEX-B, *Atmos. Chem. Phys.*, **9**, 6727-6742.

[91] Sillman, S., J. A. Logan, and S. C. Wofsy, 1990: The Sensitivity of Ozone to Nitrogen Oxides and Hydrocarbons in Regional Ozone Episodes. *J. Geophys. Res.*, **95**(D2), 18371851, doi:10.1029/JD095iD02p01837.

[92] Sillman, S., 1995: The use of NOy, H2O2, and HNO3 as indicators for ozone-NOx-hydrocarbon sensitivity in urban locations. *J. Geophys. Res.*, **100**(D7), 14,175-14,188.

[93] Simpson, D., A. Guenther, C. N. Hewitt, R. Steinbrecher, 1995: Biogenic emissions in Europe. 1. Estimates and uncertainties. *J. Geophys. Res.*, **100**D, 22875-22890.

[94] Slingo, A., 1989: A GCM parameterization for the shortwave radiative properties of water clouds. *J. Atmos. Sci.*, **46**, 1419-1427.

[95] Slinn, S.A. and W.G.N. Slinn, 1980, Prediction for particle deposition on natural waters, *Atmos. Environ.*, **14**, 1013-1016.

[96] Song, J., Lei, W., Bei, N., Zavala, M., de Foy, B., Volkamer, R., Cardenas, B., Zheng, J., Zhang, R., and Molina, L. T., 2010: Ozone response to emission changes: a modeling study during the MCMA-2006/MILAGRO Campaign, *Atmos. Chem. Phys.*, **10**, 3827-3846, doi:10.5194/acp-10-3827-2010.

[97] Steiner, A., *et al.*, 2006, Influence of future climate and emissions on regional air quality in California, *J. Geophys. Res.*, **111**, D18303, doi:10.1029/2005JD006935.

[98] Stephens, S., S. Madronich, F. Wu, J. Olson, R. Ramos, A. Retama, and R. Muñoz, 2008: Weekly patterns of Mexico City's surface concentrations of CO,

NOx, PM10 and O3 during 1986-2007, *Atmos. Chem. Phys.*, Discuss., 8, 8357-8384.

[99] Stockwell, W. R., P. Middleton, J. S. Chang and X. Tang, 1990: The second generation regional acid deposition model chemical mechanism for regional air quality modeling. *J. Geophys. Res.*, **95**, 16343–16367.

[100] Tegen, I., and I. Fung, 1994: Modeling of mineral dust in the atmosphere: Sources, transport, and optical thickness, *J. Geophys. Res.*, **99**(D11), 22897-22914.

[101] Tegen, I., and A. A. Lacis, 1996: Modeling of particle influence on the radiative properties of mineral dust aerosol. *J. Geophys. Res.*, **101**, 19237-19244.

[102] Tegen I., S. P. Harrison, K. Kohfeld, I. C. Prentice, M. Coe, and M. Heimann, 2002: Impact of vegetation and preferential source areas on global dust aerosol: Results from a model study. *J. Geophys. Res.*, **107** (D21), 4576, doi:10.1029/2001JD000963.

[103] Tegen, I., S. P. Harrison, K. E. Kohfeld, 2002: Modeling the role of mineral aerosols in global climate cycles, Eos Trans. AGU, 83(36), 395, 10.1029/2002EO000292.

[104] Tie, X., S. Madronich, S. Walters, R. Zhang, P. Rasch, and W. Collins, 2003: Effect of Clouds on photolysis and oxidants in the troposphere, *J. Geophys. Res.*, **108**(D20), 4642, doi:10.1029/2003JD003659.

[105] Tie, X., S. Madronich, S. Walters, D.P. Edwards, P. Ginoux, N. Mahowald, R.Y. Zhang, C. Lou, and G. Brasseur, 2005: Assessment of the global impact of aerosols on tropospheric oxidants, *J. Geophys. Res.*, **110** (D03204), doi:10.1029/2004JD005359.

[106] Tie, X, S. Madronich, G. Li, Z. Ying, R. Zhang, A. Garcia, J. Lee-Taylor, and Y Liu, 2007: Characterizations of Chemical Oxidants in Mexico City: A Regional chemical/dynamical Model (WRF-Chem) Study, *Atmos. Environ.*, **41**, 1989-2008.

[107] Tie, X., S. Madronich, G. Li, Z. Ying, A. Weinheimer, E. Apel, and T. Campos, 2009: Simulation of Mexico City Plumes during the MIRAGE-Mex Field Campaign Using the WRF-Chem Model. *Atmos. Chem. Phys.*, **9**, 4621-4638.

[108] Tie, X., F. Geng, L. Peng, W. Gao, and C. Zhao, 2009a: Measurement and modeling of O_3 variability in Shanghai, China: Application of the WRF-Chem model, *Atmos. Environ.*, **43**, 4289-4302.

[109] Tie, X., G. Brasseur, and Z. Ying, 2010: Impact of model resolution on chemical ozone formation in Mexico City: application of the WRF-Chem model *Atmos. Chem. Phys.*, **10**, 8983-8995.

[110] Uno I., Z. Wang, M. Chiba, Y. S. Chun, S. L. Gong, Y. Hara, E. Jung, S. S. Lee, M. Liu, M. Mikami, S. Music, S. Nickovic, S. Satake, Y. Shao, Z. Song, N. Sugimoto, T. Tanaka, and D. L. Westphal, 2006: Dust model intercomparison (DMIP) study over Asia: Overview. *J. Geophys. Res.*, **111**, D12213, doi:10.1029/2005JD006575.

[111] Velasco, E., B. Lamb, H. Westberg, E. Allwine, G. Sosa, J.L. Arriaga-Colina, B.T. Jobson, M.L. Alexander, P. Prazeller, W.B. Knighton, T.M. Rogers, M. Grutter, S.C. Herndon, C.E. Kolb, M. Zavala, B. de Foy, R. Volkamer, L.T. Molina, and M. J. Molina 2007: Distribution, magnitudes, reactivities, ratios and diurnal patterns of volatile organic compounds in the Valley of Mexico during the MCMA 2002 & 2003 field campaigns. *Atmos. Chem. Phys.*, **7**, 329-353.

[112] Velasco, E., Pressley, S., Grivicke, R., Allwine, E., Coons, T., Foster, W., Jobson, B. T., Westberg, H., Ramos, R., Hernández, F., Molina, L. T., and

Lamb, B., 2009: Eddy covariance flux measurements of pollutant gases in urban Mexico City, *Atmos. Chem. Phys.*, **9**, 7325-7342, doi:10.5194/acp-9-7325-2009.

[113] Wang, Y., J.A. Logan, D.J. Jacob, 1998: Global simulation of tropospheric O_3-NO_x-hydrocarbon chemistry. 2. Model evaluation and global ozone budget. *J. Geophys. Res.*, **103**(D9), 10727-10755.

[114] Warneck, P., 2000: Chemistry of the Natural Atmosphere. Academic Press, A Harcourt Science and Technology Company.

[115] Wayne, R. P., 2000: Chemistry of atmospheres: an introduction to the chemistry of the atmospheres of Earth, the planets, and their satellites. Oxford University Press, Oxford.

[116] Wesely, M.L., 1989: Parameterization of surface resistance to gaseous dry deposition in regional-scale numerical models, *Atmos. Environ.*, **23**, 1293-1304.

[117] Wicker, L. J. and W. C. Skamarock, 2002: Time splitting methods for elastic models using forward time schemes, *Mon. Wea. Rev.*, **130**, 2088-2097.

[118] Wood, E., S. Herndon, T. Onasch, J. Kroll, M. Canagaratna, C. Kolb, D. Worsnop, J. Neuman, R. Seila, M. Zavala, and W. Knighton, 2009: A case study of ozone production, nitrogen oxides, and the radical budget in Mexico City, *Atmos. Chem. Phys.*, **9**, 24992516, doi:10.5194/acp-9-2499-2009.

[119] Wurzler, S., T. G. Reisin, and Z. Levin, 2000: Modification of mineral dust particles by cloud processing and subsequent effects on drop size distributions. *J. Geophys. Res.*, **105**, 4501-4512.

[120] Yang, R., A. Xia, D. Michelangeli, D. Plummer, L. Neary, J. Kaminski, J. McConnell, 2003: Evaluating a Canadian regional air quality model using

ground-based observations in north-eastern Canada and United States, *J. Environ. Monit.*, **5**, 40-46.

[121] Ying, Z., X. Tie, G. Li, 2009: Sensitivity of ozone concentrations to diurnal variations of surface emissions in Mexico City: A WRF/Chem modeling study. *Atmos. Environ.*, **43**, 851-859.

[122] Ying Z., X. Tie, S. Madronich, G. Li, S. Massie, 2011: Simulation of regional dust and its effect on photochemistry in the Mexico City area during MILAGRO experiment, *Atmos. Environ.*, **45**, 2549-2558.

[123] Zhang, Y., M. K. Dubey, and S. C. Olsen, 2009: Comparisons of WRF/Chem simulations in Mexico City with ground-based RAMA measurements during the MILAGRO-2006 period. *Atmos. Chem. Phys. Discuss.*, **9**, 1329-1376.